EXPLORATION FOR UNCONFORMITY TYPE URANIUM DEPOSITS WITH AUDIO-MAGNETOTELLURIC DATA: A CASE STUDY FROM THE MCARTHUR RIVER MINE, SASKATCHEWAN, CANADA

by

Volkan TUNCER

A thesis submitted to the Faculty of Graduate Studies and Research in partial fulfillment of the requirements for the degree of Master of Science in Geophysics

Department of Physics

UNIVERSITY OF ALBERTA

Edmonton, Alberta
Fall 2007

Library and Archives Canada

Published Heritage Branch

395 Wellington Street
Ottawa ON K1A 0N4
Canada

Bibliothèque et Archives Canada

Direction du Patrimoine de l'édition

395, rue Wellington
Ottawa ON K1A 0N4
Canada

Your file Votre référence
ISBN: 978-0-494-33362-4
Our file Notre référence
ISBN: 978-0-494-33362-4

NOTICE:
The author has granted a non-exclusive license allowing Library and Archives Canada to reproduce, publish, archive, preserve, conserve, communicate to the public by telecommunication or on the Internet, loan, distribute and sell theses worldwide, for commercial or non-commercial purposes, in microform, paper, electronic and/or any other formats.

The author retains copyright ownership and moral rights in this thesis. Neither the thesis nor substantial extracts from it may be printed or otherwise reproduced without the author's permission.

AVIS:
L'auteur a accordé une licence non exclusive permettant à la Bibliothèque et Archives Canada de reproduire, publier, archiver, sauvegarder, conserver, transmettre au public par télécommunication ou par l'Internet, prêter, distribuer et vendre des thèses partout dans le monde, à des fins commerciales ou autres, sur support microforme, papier, électronique et/ou autres formats.

L'auteur conserve la propriété du droit d'auteur et des droits moraux qui protège cette thèse. Ni la thèse ni des extraits substantiels de celle-ci ne doivent être imprimés ou autrement reproduits sans son autorisation.

In compliance with the Canadian Privacy Act some supporting forms may have been removed from this thesis.

While these forms may be included in the document page count, their removal does not represent any loss of content from the thesis.

Conformément à la loi canadienne sur la protection de la vie privée, quelques formulaires secondaires ont été enlevés de cette thèse.

Bien que ces formulaires aient inclus dans la pagination, il n'y aura aucun contenu manquant.

Canada

ABSTRACT

Unconformity-type deposits supply a significant amount of the world's uranium and consist of uranium that is often deposited in fault zones that contained graphite. The low resistivity of the graphite produces a significant contrast in electrical resistivity, which can be located with electromagnetic (EM) methods. The Athabasca Basin in Western Canada hosts significant uranium deposits, and exploration in deeper parts of the basin has required the application of new EM methods. This thesis presents an evaluation of the audiomagnetotelluric (AMT) exploration method at the McArthur River mine in the Athabasca Basin. AMT data were collected at 132 stations on a grid, and two-dimensional (2D) and three-dimensional (3D) inversions were used to generate resistivity models. These models showed two major results: (1) a significant conductor coincident with a major basement fault (P2) and the uranium deposits (this conductor begins at the unconformity at a depth of 550 m and extends to a depth of at least three km); and (2) a resistive halo which might be caused by silicification associated with mineralization. However, synthetic inversions showed that this halo could be an artefact of smoothing function in the inversion scheme. The 2D inversions were validated by synthetic inversions, comparison with the 3D inversion models, and correlation with drill-hole information. 3D AMT forward modelling showed that strong 3D effects are not present in the AMT impedance data. Induction vectors showed more evidence of complexity, but the inclusion of these data in the inversion improved subsurface resolution.

ACKNOWLEDGEMENTS

I would like to thank my supervisor Dr. Martyn J. Unsworth for his support and advices during this research. Support and comments from Dr. Vadim Kravchinsky is gratefully appreciated. Dr. Weerachai Siripunvaraporn and Dr. Randall Mackie are also appreciated for running 3D inversions. James A. Craven is thanked for doing time series analysis of the AMT data.

I am grateful to Serhan Tuncer, Wen Xiao, Erşan Türkoğlu, Ted Bertrand, Dr. Wolfgang Soyer, Ahmet Ökeler, Dr. Mat Mengong, Özlem Süleyman, Dr. Jeremy Richards, Dr. Doug Schmitt and Dr. İlyas Çağlar for their contributions and helpful discussions. This study benefited from comments by Dan Brisbin, Charlie Jefferson, Brian Powell, Dr. George Jiracek and Dr. Randall Mackie.

Gary McNeice and Dr. Alan G. Jones are thanked for allowing me to use their tensor decomposition software for the regional strike analysis of AMT data.

AMT data were funded by Cameco Corporation, AREVA subsidiary COGEMA Resources Inc, the Geological Survey of Canada and Geosystem. Aeromagnetic, airborne gravity and airborne radiometry data were provided through the Geoscience Data Repository of Geoloical Survey of Canada.

Research at University of Alberta was supported by NSERC and the Alberta Ingenuity Fund. 3D inversion at Mahidol University was supported by Thailand Research Fund.

Institute for Geophysical Research and BP Energy Ltd are thanked for supporting me with a travel award for a presentation of this study at the 76th Annual Meeting of the Society of Exploration Geophysicists in New Orleans.

TABLE OF CONTENTS

1. INTRODUCTION 1

1.1. Uranium and Its Importance..... 1

1.2. Uranium Deposits 1

2. THE GEOLOGY OF THE ATHABASCA BASIN AND THE MCARTHUR RIVER MINE..... 7

2.1. Introduction..... 7

2.2. Tectonic History of the Athabasca Basin..... 9

2.3. General Characteristics of Uranium Deposition..... 11

2.4. Ore Types and Geological Attributes..... 12

2.4.1. Fracture controlled and clay bounded type ore deposits 12

2.4.2. Monometallic and polymetallic type uranium deposits.. 13

2.4.3. Ingress and egress type uranium deposits..... 14

2.5. Geology of the McArthur River Deposit..... 16

2.5.1. Regional settings of the Mc Arthur River deposit..... 16

2.5.1.1. Athabasca group stratigraphy..... 16

2.5.1.2. Wollaston group stratigraphy..... 17

2.5.2. Alteration at the Mc Arthur River mine..... 17

2.5.3. Mineralization..... 18

2.6. Geological Exploration Criteria..... 18

2.7. Summary..... 20

3. PREVIOUS GEOPHYSICAL STUDIES FOR URANIUM EXPLORATION IN THE ATHABASCA BASIN..... 21

3.1. Introduction..... 21

3.2. Regional Airborne Geophysics..... 22

3.2.1. Airborne radiometry..... 22

3.2.2. Aeromagnetic data..... 24

3.2.3. Regional gravity data..... 26
3.2.4. Airborne electromagnetic data..... 28
3.3. Previous Geophysical Studies at the McArthur River Mine..... 31
3.3.1. Seismic imaging at the McArthur River deposit..... 32
3.3.2. Gravity exploration at the McArthur River deposit..... 37
3.3.3. Magnetic studies at the McArthur River deposit..... 40
3.3.4. Borehole data from the McArthur River deposit..... 42
3.3.5. Electrical and electromagnetic studies at the McArthur River deposit..... 44
3.4. Summary..... 47

4. MAGNETOTELLURIC METHOD..... 49
4.1. The Source of Magnetotelluric Signals..... 49
4.2. Electromagnetic Wave Propagation in a Conductor..... 50
4.3. Interaction of EM Signals with a Uniform Earth..... 53
4.4. MT Impedance over a Two Dimensional Earth..... 56
4.5. Time Series Analysis in MT..... 59
4.6. Applications of AMT Method..... 60

5. EXTECH IV AUDIO-MAGNETOTELLURIC DATA COLLECTION AT THE McARTHUR RIVER MINE..... 63
5.1. EXTECH-IV AMT Data Acquisition..... 64
5.2. Dimensionality and Strike Analysis..... 65
5.3. Vertical Magnetic Field and Induction Vectors..... 68
5.4. Apparent Resistivity and Phase Curves..... 70
5.5. Pseudosections..... 70
5.6. Conclusions..... 72

6. INVERSION OF THE McARTHUR RIVER AMT DATASET..... 73
6.1. Two Dimensional Magnetotelluric Inversion..... 73
6.1.1. Two-dimensional inversion of the audio magnetotelluric data from the McArthur River..... 74
6.2. Three Dimensional Magnetotelluric Inversion..... 82
6.3. Comparison of the 2D and 3D Inversions with well log data..... 87
6.4. Conclusions..... 90

7. RESOLUTION AND SENSITIVITY STUDIES.....93
7.1. Two Dimensional Synthetic Inversions..... **93**
7.2. Three Dimensional Forward Modelling..... **99**
7.2.1. End effect of basement conductors..... **100**
7.2.2. 2D and 3D resistivity models and induction vectors..... **102**
7.2.3. Tensor decomposition of the 3D models and r.m.s. maps..... **106**
7.3. Discussion..... **108**

8. CONCLUSIONS..... 111

REFERENCES..... 115

APPENDIX A. Pseudosections.....127

APPENDIX B. Inversions.....139

ABBREVIATIONS

A	Allan Fault
ABIC	Akaike's Bayesian Information Criterion
AEM	Airborne Electromagnetic
AMT	Audio-magnetotellurics
BB	Black Bay Fault
BL	Black Lake Shear Zone
BR	Beatty River Fault
C	Carswell Impact Structure
CB	Cable Bay Shear Zone
Cap	Black-red hematite cap
CSAMT	Control Source Audio Magnetotellurics
CSEM	Controlled Source Electromagnetic
D	Douglas Formation
dBZdt	Time derivative of the z component of the magnetic field
DC	Direct Current
DEEPEM	Deep Pulse Electromagnetic method
EM	Electromagnetic
eU	Equivalent Uranium
eTh	Equivalent Thorium
EXTECH	Exploration Science and Technology
FanCGl	Fan Conglomerate

FP	Fair Point Formation
FW	Footwall
Ga	Billions years ago
GR	Grease River Shear Zone
H	Harrison Fault
LL	Locker Lake Formation
LZ	Lazenby Lake Formation
Ma	Million years ago
MEGATEM	Fixed-wing Airborne Electromagnetic System
MF	Manitou Falls Formation
MFa	Renamed as Read Formation
MFb	Manitou Falls Formation – Bird member
MFc	Manitou Falls Formation – Collins member
MFd	Manitou Falls Formation – Dunlop member
MFr	Manitou Falls Formation – Raibl member
MFw	Manitou Falls Formation – Warnes member
MT	Magnetotellurics
Myr	Million years
NF	Needle Falls Shear Zone
NLCG	Nonlinear Conjugate Gradients
O	Otherside Formation
PL	Parker Lake Shear Zone
R	Robillard Fault
RD	Read Formation
REBOCC	Reduced Basis Occam's inversion
Reg	Regolith
r.m.s.	Root mean square misfit

RRI	Rapid Relaxation Inversion
RY	Reilly Formation
S	Smart Formation
STZ	Snowbird Tectonic Zone
T	Tabbernore Fault Zone
TDEM	Time Domain Electromagnetic method
TE	Transverse Electric
TM	Transverse Magnetic
U	Uranium
UC	Unconformity
UTEM	University of Toronto Electromagnetic method
VLF	Very Low Frequency
Vp	Primary wave velocity
VR	Virgin River Shear Zone
VTEM	Versatile Time-Domain Electromagnetic method
W	Wolverine Point Formation
Y	Yaworski Fault
Z	Acoustic or Electrical Impedance

TABLE CAPTIONS

Table 1-1. Amount of uranium resources and average grades (Table taken from Jefferson et al., 2007).....**3**

Table 2-1. Uranium related geological events and their ages (after Jefferson et al., 2007 and Rainbird et al., 2007).....**10**

Table 3-1. Comparison of the VTEM and the MEGATEM system configurations (http://www.geotechairborne.com/FILES/CaseStudies/VTEM_MEGATEM_2006.pdf)..... .....**29**

Table 3-2. Ranges of magnetic susceptibilities in the Wollaston domain (after, Annesley and Madore, 1993; Thomas and McHardy, 2005).....**40**

FIGURE CAPTIONS

Figure 1-1. Athabasca and Thelon basins of Canada (Figure taken from Jefferson et al., 2007). VR: Virgin River Shear Zone, BL: Black Lake Shear Zone and STZ: Snowbird Tectonic Zone..... **2**

Figure 1-2. Average grades and tonnages of unconformity type uranium deposits in Canada with comparison to Australia (Figure taken from Jefferson et al., 2007). Numbers are associated to the uranium deposits, see Table 1 of Jefferson et al. (2007) for details..... **3**

Figure 1-3. Generic model of a unconformity type uranium deposit (after McMullan et al., 1987; Mwenifumbo et al., 2004). The Athabasca Group consist of four major sandstone units from bottom to top: The Read Formation (RD, formerly MFa), Manitou Falls Formation (MFb, MFc and MFd). Metamorphic basement Wollaston Group underlies the Athabasca group (Figure is taken from Tuncer et all., 2006a)..... **5**

Figure 2-1. Geology of the Athabasca Basin and uranium deposits. Squares show the current uranium mines, stars show proposed mines and crosses show uranium occurrences (A: Allan Fault, BB: Black Bay Fault, BL: Black Lake Shear Zone, BR: Beatty River fault, C: Carswell Impact Structure, CB: Cable Bay Shear Zone, D: Douglas formation, FP: Fair point formation, GR: Grease River Shear Zone, H: Harrison Fault, LL: Locker Lake formation, LZ: Lazenby Lake formation, MF: Manitou Falls formation (MFd-Dunlop, MFc-Collins, MFb-Bird (u: upper, l: lower), MFr-Raibl members, MFw-Warnes), NF: Needle Falls Shear Zone, O: Otherside formation, PL: Parker Lake Shear Zone, R: Robillard Fault, RD: Read formation, RY: Reilly formation, S: Smart formation, SZT: Snowbird Tectonic Zone, T: Tabbernore Fault Zone, VR: Virgin River Shear Zone, W: Wolverine Point formation, Y: Yaworski). (Figure is taken from Tuncer et al., 2006a)...**8**

Figure 2-2. A) Lithostatigraphic cross section of the Athabasca basin. B) Structural cross section of the Athabasca basin that illustrates structural geometry of the Wollaston – Mudjatik transition zone (Figure taken from Jefferson et al., 2007)..... **9**

Figure 2-3. Illite anomaly with the dravite and chlorite corridors at the eastern part of Athabasca Basin (Figure taken from Jefferson et al., 2007)..... **12**

Figure 2-4. Examples of uranium deposits in the Athabasca Basin. a) Eagle Point: Basement hosted uranium deposit, b) Cigar Lake: Typical unconformity ore and c) Dielmann: Both basement hosted and unconformity type deposit (modified from Jefferson et al., 2007).....13

Figure 2-5. Monometallic and polymetallic type unconformity related uranium deposits in the Athabasca Basin (Figure taken from Jefferson et al., 2007).14

Figure 2-6. Ingress and egress type uranium deposits (Figure taken from Jefferson et al., 2007).....14

Figure 2-7. Alteration models for egress type deposits in the eastern Athabasca Basin (Figure taken from Jefferson et al., 2007). UC: unconformity, Reg: regolith, Up-G: upper limit of graphite, Cap: black-red hematite cap, Fresh: fresh basement which is Fe-Mg chlorite biotite paragneiss.....15

Figure 2-8. Typical geological cross section of the McArthur River P2 North deposit and the P2 fault (Figure taken from Györfi et al., 2004). Pink rectangles show the mineralization corresponds to the first three categories listed below.....18

Figure 3-1. Regional radiometry data from the Athabasca Basin. The panel at the top shows the rate of a natural air absorbed dose (also called Total Count). The-mid panels shows the K, eU and eTh and the bottom panels shows the ratios of eU/eTh, eTh/K and eU/K from left to right. The redrawn from data from Geological Survey of Canada. Black line shows the limit of Athabasca Basin.....23

Figure 3-2. Total residual magnetic field in the Athabasca Basin and the surrounding area. The Geological Survey of Canada collected the magnetic data at elevation of 305 m with line spacing of 800 m. Dashed line showed one of the low magnetic trends interpreted as the Wollaston Domain – Mudjatik Domain transition zone. Black line shows the limit of Athabasca Basin. Taken from Matthews et al., (1997).....24

Figure 3-3. The agreement between the magnetic anomaly and basement geology (Figure is taken from Matthews et al., 1997). White dots shows the known uranium deposits, and white lines shows the graphitic conductors mapped by EM studies, the white dashed lines show the shear zones interpreted by EM and the linear trends of low magnetic intensity. Black line shows the border of the Athabasca Basin.....25

Figure 3-4. Shaded relief map of the vertical derivative of the residual magnetic field of the Athabasca Basin and the surrounding area. + sign shows some of the main uranium deposits of the Athabasca Basin.....**26**

Figure 3-5. Corrected Bouguer gravity anomaly map for the Athabasca Basin (Figure is taken from Matthews et al., 1997).....**27**

Figure 3-6. Two dimensional gravity model of line A-A' in Figure 3-4. Green circles show the observed gravity data where solid black line shows the fit of the model which was given in the bottom panel. The thickness of the Athabasca sediments is inferred from drill hole and seismic data (Figure is taken from Matthews et al., 1997).....**28**

Figure 3-7. Electrical resistivity properties of rocks found in the Athabasca Basin (after Cristall and Brisbin, 2006; Irvine and Witherly, 2006).....**29**

Figure 3-8. MEGATEM, VTEM and ground resistivity data and conductivity depth sections of the line in the Athabasca Basin (Figure is taken from Irvine and Witherly, 2006). (LEI: Layered Earth Inversion, dBZdt: time derivative of the z component of the B field).....**30**

Figure 3-9. Location of the seismic lines (blue) at the McArthur River property with the AMT stations (red circles) and borehole locations (black stars). Black diamond signs show the uranium pods. Coordinates of the seismic lines were taken from White et al. (2007). Dashed blue line shows the location of the cross-line 50.....**33**

Figure 3-10. Possible seismic reflection response of the uranium deposit itself around the P2 ore body (modified from White et al., 2002).....**34**

Figure 3-11. Top panel shows the final migrated data and the bottom panel shows the interpretation of the 2D high resolution seismic Line 12 (Figure is taken from Györfi et al., 2007). Note that the line is perpendicular to the P2 fault trend (see Figure 3-9).....**35**

Figure 3-12. Top panel shows the migrated seismic section for Line 14, the bottom panel shows the interpretation (Figure is taken from Györfi et al., 2007). The unconformity at the sandstone / basement interface was well imaged. Intersecting faults and fault offsets were also identified in the seismic section.....**36**

Figure 3-13. Interpretation of the cross-line 50 (Figure is taken from Györfi et al., 2004). Note that this line is parallel to the P2 fault trend.....**37**

Figure 3-14. Bouguer gravity anomaly map of the McArthur River Mine area. (Figure is taken from Wood and Thomas, 2002). The thick black line shows the high resolution gravity profile and the blue dot shows the McArthur River deposit. Black dots shows the gravity stations. Contour interval is 0.5 mGals..... **38**

Figure 3-15. Gravity modelling of the intermediate wavelength anomalies (Figure taken from Wood and Thomas, 2002)..... **39**

Figure 3-16. Residual magnetic field and its vertical derivative at the McArthur River mine. Black symbols indicate the uranium deposits. Aeromagnetic data was provided by Geological Survey of Canada..... **41**

Figure 3-17. Borehole MAC218. OB: Overburden, MFa,b,c,d: Manitou Falls a, b, c, d members, FanCGl: Fan Conglomerate and Bsmt: Basement (Figure is taken from Mwenifumbo et al., 2004). MFa is also known as the Read Formation. **43**

Figure 3-18. Borehole RL088 (Figure is taken from Mwenifumbo et al., 2004)..... **44**

Figure 3-19. Conductor axis as located by time domain EM surveys in the McArthur River area (Figure is taken from Thomas and Wood, 2007)..... **45**

Figure 3-20. Upper panel = VLF data. Lower panel = pseudosection of CSAMT data (Figure is taken from McGill et al., 1993)..... **46**

Figure 4-1. Illustration of the skin depth (depth of penetration), which shows the relationship between the AMT frequencies and the resistivity of the medium of the survey area..... **52**

Figure 4-2. Physics of electromagnetic waves in a halfspace (Figure is modified from http://www-geo.phys.ualberta.ca/~unsworth/MT/MT.html). High frequencies penetrate to the shallow depths where low frequencies penetrate to the deeper parts of the earth..... **53**

Figure 4-3. The definition of phase in an Argand diagram..... **54**

Figure 4-4. The subsurface electrical model (left panel) and associated resistivity (middle panel) and phase (right panel) curves. The solid line represents the homogeneous half-space model. The dashed curve represents a model in which the second layer is more resistive. The dotted curve represents a model in which the second layer is less resistive..... **55**

Figure 4-5. Propagation of EM signals with Snell's Law (Unsworth, 2003 Geoph424 lecture notes)..... **55**

Figure 4-6. Configuration of MT in the field above the prism model ($\rho_2<\rho_1$).**56**

Figure 4-7. TE and TM modes in magnetotellurics..... **57**

Figure 4.8. Behaviour of the vertical magnetic field over a 2D earth. Induction vectors point towards a conductor as in the convention of Parkinson (1962)..... **58**

Figure 4-9. A sample time series at the AMT frequencies due to a distant lightning strike recorded in Central California (modified from http://www-geo.phys.ualberta.ca/~unsworth/MT/time_series_lightning.gif)..... **60**

Figure 5-1. Station locations of the EXTECH-IV AMT data set at the McArthur River mine. Blue diamond signs indicate the uranium pod locations. The black lines show strike directions derived by tensor decomposition for real data over a frequency range 1000 – 1 Hz. Northeast - southwest striking topography features are due to the glacial flow. Dashed red line shows the direction of the P2 Fault..... **64**

Figure 5-2. Rose diagrams of geoelectric strike and channelling angle computed with the algorithm of McNeice and Jones, (2001)..... **66**

Figure 5-3. The contour map of the r.m.s. misfit values obtained from the tensor decomposition code mostly shows values below the acceptable value of 1.5.**67**

Figure 5-4. Contour map of the shear and twist angles at the McArthur River area derived from tensor decomposition with the McNeice and Jones (2001) algorithm. These values are not close to the maximum possible values, which suggest that the distortion is not strong in this area..... **68**

Figure 5-5. Real induction vectors at 100 Hz frequency in the Parkinson (1959) convention. Note that the induction vectors point at a conductor in this convention. Solid red line shows the conductor, dashed red line shows the possible extension of the conductor..... **69**

Figure 5-6. Sample data curves of TE and TM mode AMT data for stations on lines 224, 248 and 304. Note that there are no data near 2 KHz in the AMT dead band..... **70**

Figure 5-7. Pseudosections of the AMT data of line 224 with the defined strike direction of N45°E. White areas show deleted data (i.e. AMT dead band)...**71**

Figure 6-1. Resistivity models derived for profile 224 with 2D AMT inversions. Black triangles show the station locations and there is no vertical exaggeration..... **75**

Figure 6-2. Sample data curves of TE and TM mode data for stations on profiles 224, 248 and 304. Continuous lines show the fit of the response of the inversion models for the TE mode and TM mode data. These data are shown in Figure 5-7 (Figure is taken from Tuncer et al., 2006a).....**76**

Figure 6-3. The r.m.s. misfit values for TE-TM (dashed) and TE-TM-T_{zy} (solid) inversions for each profile (Figure is taken from Tuncer et al., 2006a).....**77**

Figure 6-4. Resistivity models for all profiles derived with 2D inversions. Left column shows the TE-TM-T_{zy} inversions and the right column shows the TE-TM inversions (Figure is taken from Tuncer et al, 2006a).....**78**

Figure 6-5. Inversion results for profile 224 with different τ values (3, 10 and 30) and α=1 (left panel), and α values (1, 0.3 and 0.1), and τ=10 (right panel). r.m.s. misfit values and iteration numbers are also given in the figure for comparison.....**79**

Figure 6-6. Models obtained by TE-TM-T_{zy} and TM-T_{zy} inversions of the AMT data on profile 224. These inversions illustrate the presence of a second conductor to the northwest of the survey area.....**80**

Figure 6-7. Plot of well log resistivity and 1-D AMT inversion at borehole MAC265 (Craven et al., 2002; 2007). The resistive zone in the depth range 140-240 metres were interpreted as silicified alteration zone. This image suggests that 1D AMT modelling can be used to locate silicified zones..... **82**

Figure 6-8. Vertical slices of the 3D TE-TM inversion using the REBOCC algorithm. The starting model was a 1000 Ω.m halfspace and the horizontal to vertical smoothing was set to unity. The error floor of the impedance was taken as 5 %. The initial and the final r.m.s. misfit values were 5.56 and 1.38 respectively..... **84**

Figure 6-9. Comparison of the REBOCC and NLCG6 inversions for profiles 224, 254, 276 and 304. Note that NLCG algorithms included the vertical magnetic field data into the 2D and 3D inversions as well as the TE and TM mode data. REBOCC algorithm just used the TE mode and TM mode data for the

3D joint inversion. White squares on profile 276 show locations of the uranium pods of the McArthur River P2 North deposit.....**85**

Figure 6-10. Horizontal slices of resistivity contour maps from different depths obtained from 3D inversion results of REBOCC algorithm. White squares show locations of the uranium pods. Cross signs (x) show the locations of the AMT stations of McArthur River.....**86**

Figure 6-11. Comparison of two dimensional and three dimensional horizontal depth slices at different depths showing the similarities in the McArthur River area (Figure is taken from Tuncer et al., 2006a). White diamonds indicate locations of the uranium pods. Two dimensional inversions used the NLCG algorithm whereas three dimensional inversion used REBOCC algorithm...**87**

Figure 6-12. Comparison of the horizontal slices of the inversion models derived with NLCG and REBOCC algorithms. Models are shown at depths of 300, 500, 500 and 1000 m. White diamonds show locations of the uranium pods.....**88**

Figure 6-13. Comparison of borehole-log resistivity data (from Mwenifumbo et al., 2004) and the of 2D and 3D joint inversion models (Figure is modified from Tuncer et al., 2006a). A 7-point moving average filter was applied to the resistivity log data to allow a more objective comparison of the two measures of subsurface resistivity.....**89**

Figure 6-14. Comparison of 2D and 3D inversion results for lines 248 and 304. Comparison with resistivity in adjacent borehole logs is also shown (Figure is modified from Tuncer et al., 2006b).....**90**

Figure 7-1. Synthetic inversion study showing the effect of different smoothing parameters. (a) This model represents the alteration chimney (500 Ω.m) beneath a 25 m thick, 2000 Ω.m resistive overburden and shows a resistivity contrast across the fault with different smoothing parameters. (b) This model shows a basic two-layer model with a graphitic conductor that has an artificial resistive halo around the conductor.....**94**

Figure 7-2. Synthetic model of dipping basement conductor. The left panel shows the results of an inversion using α=0.3 and a range of τ parameters (3, 10 and 30). The right panel shows the results of synthetic inversions using α=1 and the same τ parameters.....**96**

Figure 7-3. Synthetic model of two parallel dipping basement conductors. The choice of α and τ, the smoothing parameters, of this synthetic model is same as in Figure 7-2.....**97**

Figure 7-4. Synthetic model of two crossing basement conductors. Note that the choice of α and τ parameters in this figure is same as in Figure 7-2..... **98**

Figure 7-5. Synthetic model of stair-like fault geometry. Note that the choice of α and τ parameters in this figure is same as in Figure 7-2..... **99**

Figure 7-6. Comparison of resistivity and phase curves obtained from the 2D and 3D forward modelling algorithms. Note that both modelling programs used NLCG algorithm. Red circles show TE mode curves, blue squares show TM mode curves..... **100**

Figure 7-7. End effect in AMT data. Site A shows how the end of the conductor influences the TE mode response. The response at Site B shows that the end effect gets weaker as distance from the end of the conductor increases.....**101**

Figure 7-8. 2D models computed by 3D forward algorithm to test the 2D behaviours of the induction vectors..... **103**

Figure 7-9. 3D models used to model the measured induction vectors.... **104**

Figure 7-10. 3D models that includes crossing conductors to model the measured induction vectors.....**106**

Figure 7-11. Results of tensor decomposition for measured data and synthetic 3D model over a frequency range 1 – 1000 Hz. (a) Shows best fitting strike direction in map format and the misfit obtained by the tensor decomposition. Low misfit values indicate the 2D assumption is well satisfied. (b) Same quantities for synthetic data generated for a 2D resistivity model. (c) Same quantities for synthetic data generated for a 3D resistivity model. Red rectangular bars shows the locations of conductors in the synthetic models.....**107**

Figure 8-1. Resistivity model derived from the 2D inversion of the TE-TM-T_{zy} data on profile 224 (Figure is modified from Tuncer et al., 2006a).....**111**

Figure A-1. Pseudosections of the measured data and fits of the 2D inversions for profile 224. Note that $\alpha = 1$ and $\tau = 10$ in the inversion.....**128**

Figure A-2. Pseudosections of the measured data and fits of the 2D inversions for profile 234. Note that $\alpha = 1$ and $\tau = 10$ in the inversion.....**129**

Figure A-3. Pseudosections of the measured data and fits of the 2D inversions for profile 240. Note that $\alpha = 1$ and $\tau = 10$ in the inversion.....**130**

Figure A-4. Pseudosections of the real data and the fits of the 2D inversion for profile 248. Note that $\alpha = 1$ and $\tau = 10$ in the inversion.....**131**

Figure A-5. Pseudosections of the real data and the fits of the 2D inversion for profile 254. Note that $\alpha = 1$ and $\tau = 10$ in the inversion.....**132**

Figure A-6. Pseudosections of the real data and the fits of the 2D inversion for profile 266. Note that $\alpha = 1$ and $\tau = 10$ in the inversion..... **133**

Figure A-7. Pseudosections of the real data and the fits of the 2D inversion for profile 271. Note that $\alpha = 1$ and $\tau = 10$ in the inversion..... **134**

Figure A-8. Pseudosections of the real data and the fits of the 2D inversion for profile 276. Note that $\alpha = 1$ and $\tau = 10$ in the inversion..... **135**

Figure A-9. Pseudosections of the real data and the fits of the 2D inversion for profile 288. Note that $\alpha = 1$ and $\tau = 10$ in the inversion..... **136**

Figure A-10. Pseudosections of the real data and the fits of the 2D inversion for profile 296. Note that $\alpha = 1$ and $\tau = 10$ in the inversion..... **137**

Figure A-11. Pseudosections of the real data and the fits of the 2D inversion for profile 304. Note that $\alpha = 1$ and $\tau = 10$ in the inversion..... **138**

Figure B-1. Resistivity models of TE mode and TE-T_{zy} for all profiles..... **140**

Figure B-2. Resistivity models of TM mode and TM-T_{zy} for all profiles.....**141**

Figure B-3. Resistivity models of vertical magnetic field for all profiles..... **142**

1. INTRODUCTION

1.1. Uranium and Its Importance

Uranium is a radioactive element with an atomic number of 92. It was discovered in 1789 by Martin Heinrich Klaproth and named after planet Uranus. It is a silvery-white metal whose radioactive properties were first discovered by Beqerel in 1896. The abundance of uranium in the Earth's crust is 0.91 ppm (parts per million) and 0.003 ppm in the ocean. Uranium occurs in significant quantities in the minerals pitchblende and carnotite. For many centuries, uranium was used as a orange or yellow pigment for colouring glass. Today it is primarily used as a fuel in nuclear reactors and in military applications. In recent years a number of new nuclear plants have been planned and there has been a sharp increase in the uranium prices. Prices were around US$10 per pound in the 1990's and have increased more than ten fold reaching a maximum price in June 2007 of US$135 per pound. This increase in price has resulted in an increase in uranium exploration necessitating new exploration methods. This thesis describes the evaluation of a new uranium exploration method with application to one of the largest known deposits in the world.

1.2. Uranium Deposits

Uranium is found in a number of types of deposits. These include:

1) Meso-proterozoic unconformity deposits,

2) Meso-proterozoic breccia complex deposits,

3) sandstone hosted deposits,

4) surficial deposits,

5) large tonnage but low grade resources in early Paleo-proterozoic conglomeratic deposits,

6) small percentages in volcanic, metasomatic, metamorphic, granite-hosted and vein-type deposits (World Uranium Mining, 2004).

More than one third of the uranium resources are unconformity related deposits and have grades 3-100 times higher than any other types of deposit (Jefferson et al., 2007). The Athabasca and Thelon Basins of Canada, (Figure 1-1) and the Kombolgie Basin, sub-basin of the McArthur Basin, Australia, host this type of uranium deposits.

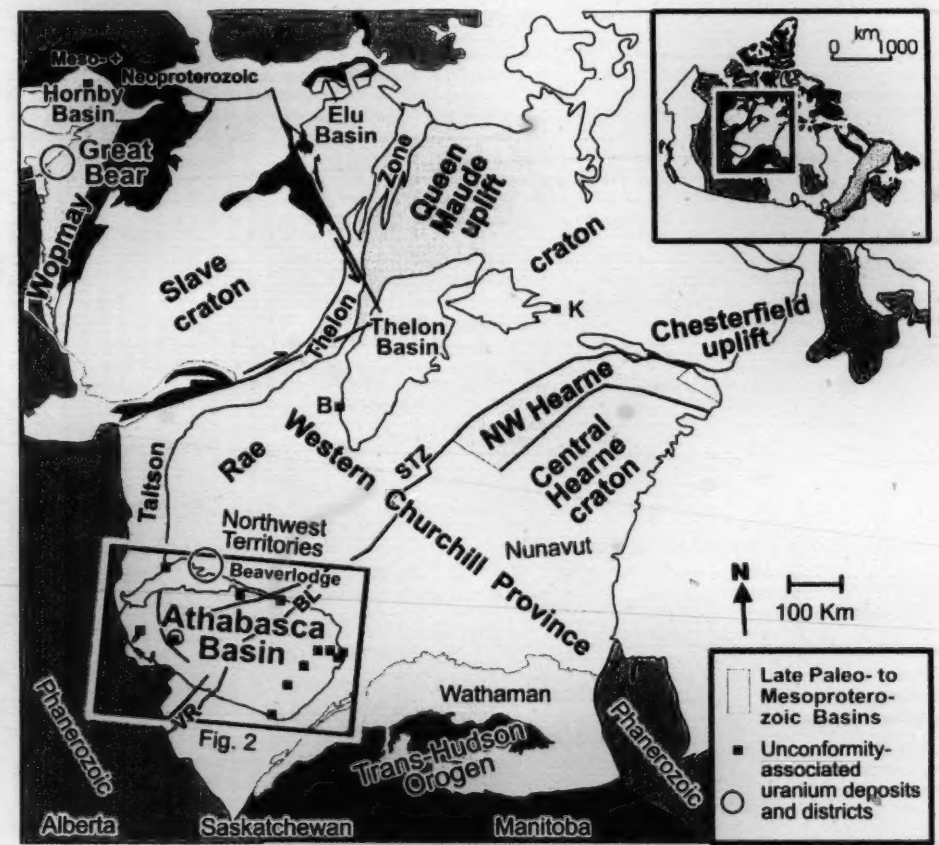

Figure 1-1. Athabasca and Thelon basins of Canada (Figure taken from Jefferson et al., 2007). VR: Virgin River Shear Zone, BL: Black Lake Shear Zone and STZ: Snowbird Tectonic Zone

In these deposits, uranium occurs as uraninite, mostly as pitchblende (Jefferson et al., 2007). The average grades of monometallic and polymetallic type uranium deposits of Canada are given in Figure 1-2 and compared to Australian deposits. Note that the McArthur River deposit, which is the focus of this thesis, is the highest grade uranium deposit in the world.

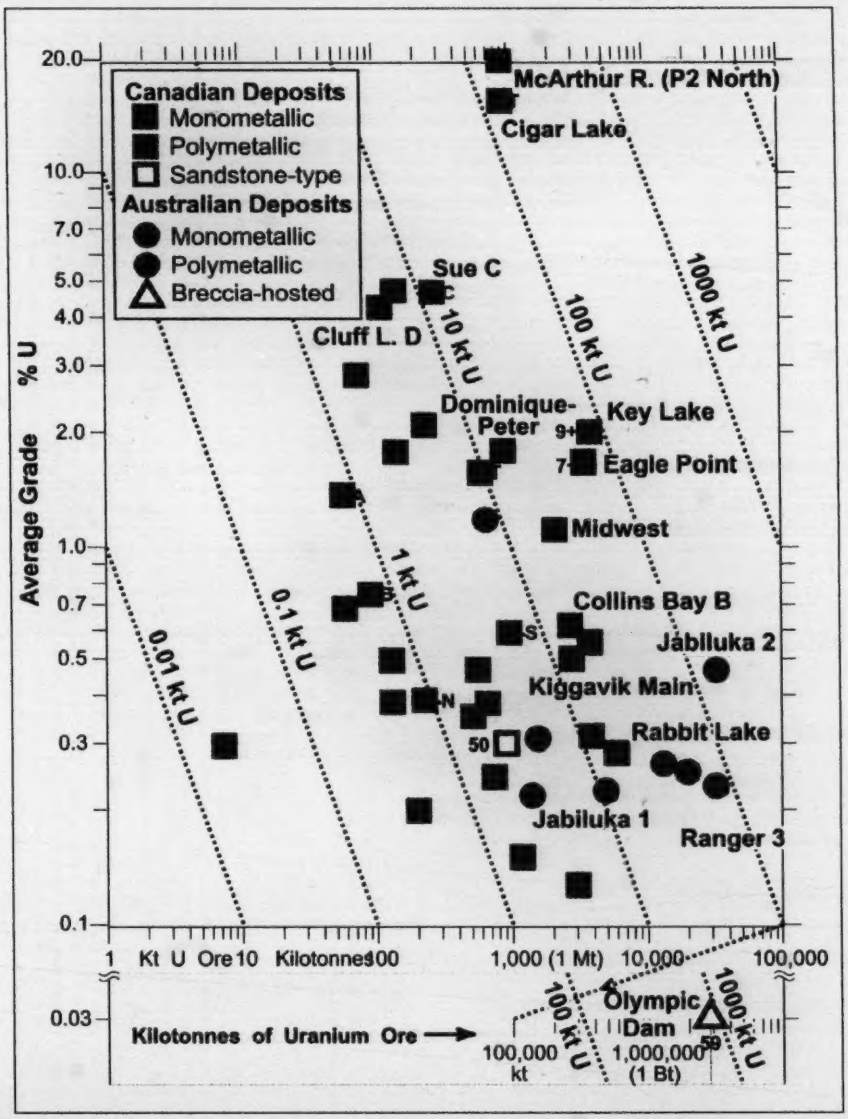

Figure 1-2. Average grades and tonnages of unconformity type uranium deposits in Canada with comparison to Australia (Figure taken from Jefferson et al., 2007). Numbers are associated to the uranium deposits, see Table 1 of Jefferson et al. (2007) for details.

Figure 1-2 shows that the grades and tonnages of the Cigar Lake and McArthur River deposits in Athabasca Basin are very high. The grades are 15 % and 22 % U and are estimated to contain 131 and 192 thousand tonnes uranium, respectively (Jefferson et al., 2007). The average grade of the whole Athabasca Basin is 1.97 % which is four times more than in Australia (Jefferson et al., 2007). Table 1-1 shows details for some of these basins.

Table 1-1. Amount of uranium resources and average grades (Table taken from Jefferson et al., 2007).

District	ore (Kt)	% U	Tonnes U
Athabasca Basin (Canada)	28810	1.922	553778.0
Beaverlodge District (Canada)	15717	0.165	25539.0
Thelon Basin (Canada)	11989	0.405	48510.0
Hornby Bay Basin (Canada)	900	0.300	2700.0
Kombolgie Basin (Australia)	87815	0.323	283304.0
Paterson Terrane (Australia)	122200	0.250	30.5
Olympic Dam (Australia)	2877610	0.030	863283.0

Uranium has become an economically important mineral and finding new uranium deposits is essential for the continued operation of nuclear power plants. Since unconformity type uranium deposits are a major source of high grade uranium ore, it is vital to understand the characteristics of these. Most shallow uranium deposits in the Athabasca Basin have been mined out, and exploration has moved into the deeper parts of the basin. Therefore, new techniques are needed to image at greater depths. To facilitate this, the government of Canada and industrial partners initiated a multidisciplinary project, the EXploration science and TECHnology (EXTECH IV) project (Jefferson et al., 2003). Most of the geophysical and geological studies took place in the McArthur River mine (Jefferson et al., 2007). Unconformity deposits are generally found where a fault intersects the unconformity (Figure 1-3). Graphite is commonly deposited in these faults and produces a very low electrical resistivity. This allows the detection of the fault with electrical and electromagnetic methods.

Electromagnetic (EM) methods can be divided into those using man-made signals (controlled source) and those that use natural EM signals (natural source). In the former, a transmitter coil creates a primary EM field. Interaction of the primary field with the Earth produces a secondary EM field. A receiver coil records the combination of primary and secondary fields and data analysis techniques are used to infer the subsurface resistivity structure. Natural source EM methods use magnetospheric and ionospheric currents as an energy source. A major advantage of natural source EM methods is that a greater depth of penetration can be achieved than with controlled source EM methods. This is because deep sounding does not require large dipoles or transmitters, just the

recording of low frequency signals. In addition, plane wave assumption allows the use of simpler mathematics for data analysis. EM methods are widely used in mineral exploration and have played an important role in uranium exploration in the Athabasca Basin (McMullan et al., 1987; Crone, 1991; Leppin and Goldak, 2005; Irvine and Witherly, 2006). However, traditional controlled source EM (CSEM) methods generally have limitations in terms of depth of penetration. An alternative EM method, audio-magnetotellurics (AMT), was evaluated during the EXTECH IV project to determine if it could contribute to deep uranium exploration. This research is described in detail in this thesis.

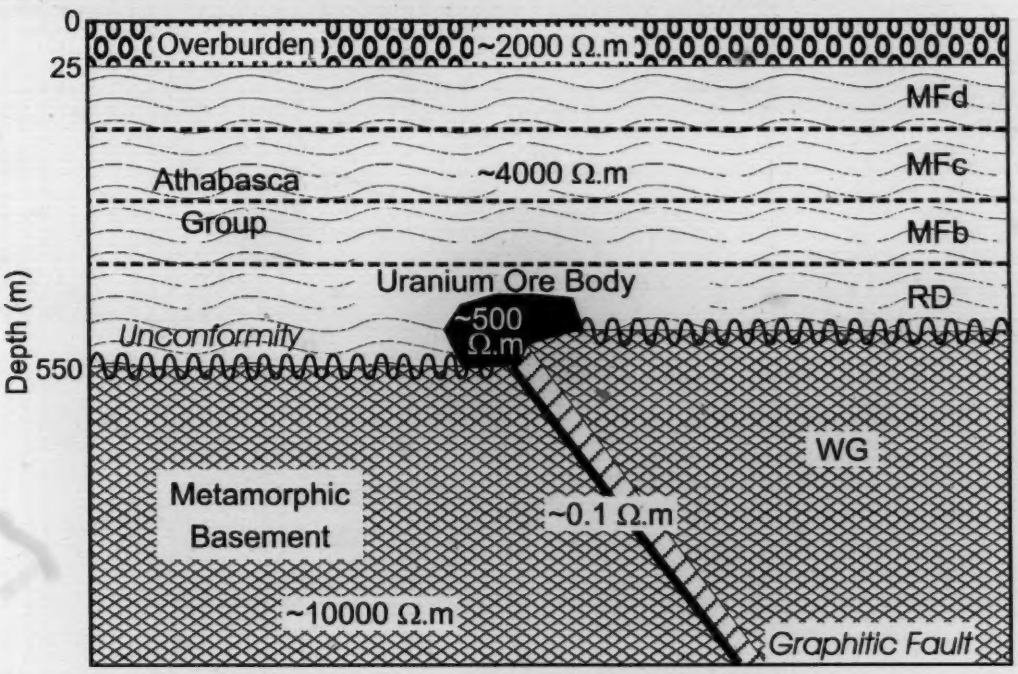

Figure 1-3. Generic model of a unconformity type uranium deposit (after McMullan et al., 1987; Mwenifumbo et al., 2004). The Athabasca Group consist of four major sandstone units from bottom to top: The Read Formation (RD, formerly MFa), Manitou Falls Formation (MFb, MFc and MFd). Metamorphic basement Wollaston Group underlies the Athabasca group (Figure is taken from Tuncer et all., 2006a).

2. THE GEOLOGY OF THE ATHABASCA BASIN AND THE MCARTHUR RIVER MINE

2.1. Introduction

The Athabasca Basin is a Proterozoic sedimentary basin that is located in northwest Saskatchewan and northeast Alberta (Figure 2-1; Jefferson et al., 2007). In this basin the 1730 Ma Athabasca Group sandstones unconformably overly graphite-rich meta-sedimentary basement rocks (Alexandre et al., 2007). These basement rocks have been divided into three major litho-tectonic zones (Figure 2-1): 1) the Taltson Magmatic Zone, 2) the Rae Province and 3) the Hearne Province (Card et al., 2007). The Rae and the Hearne provinces are Archean in age. The Snowbird tectonic zone, which includes the Virgin River and Black Lake Shear Zones, is a continental scale Paleoproterozoic suture that divides the Rae and the Hearne provinces, and is located close to the centre of the Athabasca Basin. The Taltson Magmatic Zone underlies the western part of the Athabasca Basin in the Alberta portion (Card et al., 2007). It is a Paleoproterozoic composite continental magmatic arc and collisional orogen resulting from the convergence of the Buffalo Head terrane with the Archean Churchill craton. The Carswell Structure is another important feature in the Athabasca Basin, and is a 40 km wide impact structure that is 110 Myr old and is located at the western part of the basin (Figure 2-1).

In the Athabasca Basin, the unconformity related uranium deposits consist of massive pods, veins and disseminated uraninite located at the unconformity between Proterozoic sedimentary rocks and the Archean and Aphebian metamorphic basement (Jefferson et al., 2007; Alexandre et al., 2007). The sedimentary rocks are relatively flat-lying, unmetamorphosed, late Paleo-proterozoic to Meso-proterozoic, fluvial red-bed strata. The underlying basement is tectonically interleaved Paleo-proterozoic metasedimentary and Archean to Proterozoic granitoid rocks (Jefferson et al., 2007).

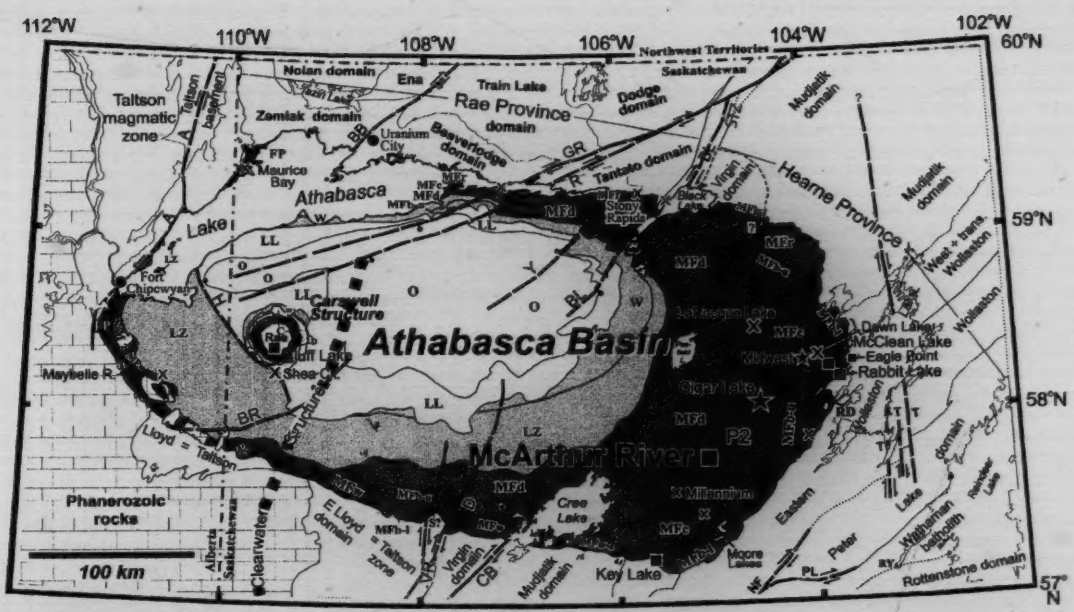

Figure 2-1. Geology of the Athabasca Basin and uranium deposits. Squares show the current uranium mines, stars show proposed mines and crosses show uranium occurrences (A: Allan Fault, BB: Black Bay Fault, BL: Black Lake Shear Zone, BR: Beatty River fault, C: Carswell Impact Structure, CB: Cable Bay Shear Zone, D: Douglas formation, FP: Fair point formation, GR: Grease River Shear Zone, H: Harrison Fault, LL: Locker Lake formation, LZ: Lazenby Lake formation, MF: Manitou Falls formation (MFd-Dunlop, MFc-Collins, MFb-Bird (u: upper, l: lower), MFr-Raibl members, MFw-Warnes), NF: Needle Falls Shear Zone, O: Otherside formation, PL: Parker Lake Shear Zone, R: Robillard Fault, RD: Read formation, RY: Reilly formation, S: Smart formation, SZT: Snowbird Tectonic Zone, T: Tabbernore Fault Zone, VR: Virgin River Shear Zone, W: Wolverine Point formation, Y: Yaworski). (Figure is taken from Tuncer et al., 2006a).

A number of sedimentary basins of Proterozoic age are found in this part of the Canadian Shield. However, the Athabasca Basin is the most important basin in terms of uranium production. In the Athabasca Basin a significant number of uranium deposits are located where the Athabasca Group unconformably overlies the western Wollaston and Wollaston – Mudjatik transition basement domains. As deposits have been extracted from the shallow parts of the basin, exploration has moved into the deeper part of the basin. Recent exploration has located the Cluff Lake and Shea Creek deposits and identified the Maybelle River prospect. Exploration has also shown potential for new unconformity related deposits in the western part of the Athabasca Basin (Jefferson et al. 2007). Since the unconformity depth is deeper in this part of the

basin it is not presently economic to extract deeper deposits (Jefferson et al., 2007). However, increasing uranium demand and prices will eventually make mining in this area feasible and new exploration methods are needed. The EXTECH IV project was initiated to develop improved exploration strategies for the deeper part of the basin. Figure 2-2 shows the statigraphic and structural cross section of the Athabasca Basin based on the results of the EXTECH IV project (Jefferson et al., 2007).

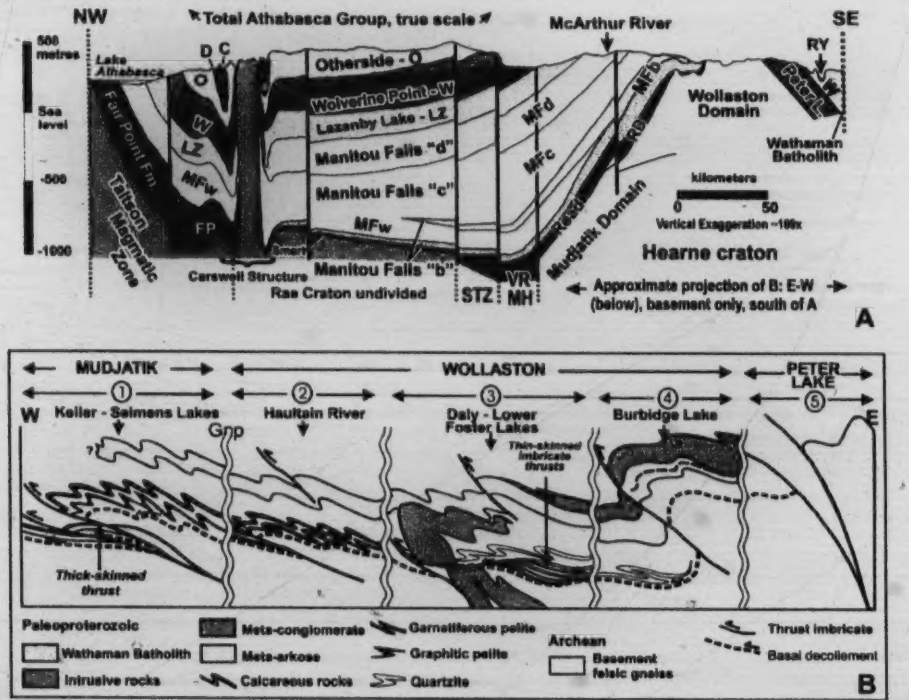

Figure 2-2. A) Lithostatigraphic cross section of the Athabasca basin. B) Structural cross section of the Athabasca basin that illustrates structural geometry of the Wollaston – Mudjatik transition zone (Figure taken from Jefferson et al., 2007).

2.2. Tectonic History of the Athabasca Basin

The basement rocks are Archean and Paleoproterozoic rocks that were last metamorphosed at 1.8 Ga by the Trans Hudson Orogen (Alexandre et al., 2007). The tectonism here is marked by brittle reactivation of fault zones in the 1.9 Ga Taltson and 1.8 Ga Trans-Hudson orogens that accommodated ductile transpression during convergence of the Slave, Rae and Superior provinces (Jefferson et al., 2007). Detailed sedimentologic and statigraphic analyses

(Bernier, 2004; Long, 2007; Yeo et al., 2007) have shown that such faults are spatially related to pre-Athabasca Group paleotopographic features such as paleo-valleys and minor fault scarps (Jefferson et al., 2007). Jefferson et al. (2007) also indicate that topographic features formed by relatively subtle continental scale tectonics influenced the movements of basinal and basement fluids, some of which precipitated world class ore deposits.

Table 2-1. Uranium related geological events and their ages (after Jefferson et al., 2007 and Rainbird et al., 2007).

Ages	***Events***
1900 Ma	Taltson Orogeny
1800 Ma	Trans-Hudson Orogeny
1750 Ma	Basement formed
1740 – 1730 Ma	Sedimentation began
1700 – 1650 Ma	Uranium deposits formed
1500 Ma	1st ore related hydrothermal event occurred
1350 Ma	2nd ore related hydrothermal event occurred
1176 Ma	1st alteration and U remobilization
900 Ma	2nd alteration and U remobilization
300 Ma	3rd alteration and U remobilization

Formation of the uranium deposits required the development of an overlying sedimentary sequence. Rainbird et al. (2006) estimated that sedimentation began in the Athabasca Basin at about 1740-1730 Ma, since the youngest metamorphic ages observed in the underlying Wollaston Domain basement rocks are 1750 Ma. Thus, it was thought that the sedimentation began after the formation of the Wollaston domain. Two ages have been determined for the Athabasca sandstones. Volcanic tuffs within the Athabasca Group (Wolverine Point Formation) have been dated at 1644±13Ma (U-Pb). Sequence 4 of the Douglas Formation, capped by organic-rich shale, were dated as about 100 Ma younger using Os-Re dating (Creaser and Stasiuk, 2007). Uranium deposits could have formed earlier, and the fluorapatite ages of >1650-1700 Ma suggest a basin-wide diagenetic / hydrothermal event at about that time. Available geochronology of the Athabasca Basin uranium deposits records one or two main hydrothermal ore-related events within the basin at around 1500 and 1350

Ma that were overprinted by further alteration and uranium remobilization events at approximately 1176 Ma, 900 Ma and 300 Ma (Hoeve and Quirt 1984; Cumming and Krstic 1992; Fayek et al., 2002a). This implies that the uranium deposits began to form while sediment was still accumulating in the Athabasca Basin, after early diagenesis and during late, high-temperature diagenesis (Jefferson et al., 2007). Table 2-1 summarizes these events.

2.3. General Characteristics of Uranium Deposition

The unconformity between the Athabasca group sandstones and the underlying basement rocks is favourable for uranium deposition. Deposits are most likely to be formed where the unconformity intersects underlying fold and thrust belts such as the Wollaston Group (Jefferson et al., 2007). This is because faults and fracture zones in these belts permit significant fluid flow across the unconformity. If these fluids contained uranium, deposition can occur if the fault contained graphite. This occurs because the reducing conditions convert uranium from relatively soluble U^{6+} ions to insoluble U^{4+} ions. Thus graphite rich faults often underlie uranium deposits. This is significant because the low resistivity of graphite allows it to be easily located with electromagnetic exploration methods.

The hydrothermal circulation associated with uranium deposition also causes alteration of the host rocks. Sedimentary and metamorphic minerals can form clays minerals such as illite and dravite (Jefferson et al., 2007). These alteration zones also show high electrical conductivities which can make them useful exploration targets. In the Athabasca Basin other types of regional-scale alteration have also been identified. These are: 1) Basin-wide pre-ore diagenetic sandstone alteration, and 2) Sub-basin-scale ore-related alteration halos (Jefferson et al., 2007). This, second type of alteration is more important for uranium exploration since it is ore related. Earle and Sopuck (1989) give an example of this type of alteration that comprises a large illite anomaly that extends in a corridor, 10 – 20 km wide from the Key Lake deposit to the northeast (Figure 2-3). There are also linear zones of anomalous chlorite and dravite in this zone. This anomaly covers some important uranium deposits (Key Lake, P-Patch, McArthur River and Millennium) in the south-eastern part of the Athabasca Basin (Jefferson et al., 2007). Therefore, it is important to delineate these alteration zones in terms of the uranium exploration because they form mostly above or sometimes near the uranium deposits.

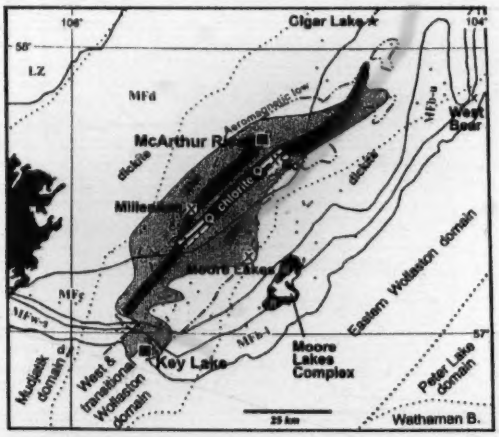

Figure 2-3. Illite anomaly with the dravite and chlorite corridors at the eastern part of Athabasca Basin (Figure taken from Jefferson et al., 2007).

The illite anomaly also appears to be associated with a 5 – 20 km wide low aeromagnetic anomaly (dotted dashed red contour in Figure 2-3). It was suggested that metaquartzite and metapelite units caused a magnetic low in this region (Jefferson et al., 2007). This region also showed K anomalies in airborne and ground spectral gamma ray surveys (Shieves et al., 2000).

2.4. Ore Types and Geological Attributes

2.4.1. Fracture controlled and clay bounded type ore deposits

Uranium deposits in the Athabasca Basin can be categorized into two different types (Jefferson et al., 2007). The first type is the fracture controlled basement ore deposit and occur in dipping shear zones such as McArthur River, Rabbit Lake, Eagle Point, Sue C, Dominique-Peter, Raven and Horseshoe. They can extend as much as 400 m below the unconformity (i.e. Eagle Point in Figure 2-4a). Disseminated and massive uraninite and/or pitchblende occupy fractures and these deposits have grades between 1 % and 3 % U_3O_8 (0.8 - 2.5 % U) (Jefferson et al., 2007).

The second type of deposit is termed the clay bounded ore deposit, and occur along, and just above, the unconformity. They comprise elongate, pipe-like and cigar shaped ore bodies with a high grade core (1 – 1.5 % U_3O_8) and a low grade halo (<1 % U_3O_8) (Jefferson et al., 2007). Most of these ore bodies have root-like extensions into the basement below the unconformity. This type of ore body is found at the following deposits : Cigar Lake, Key Lake, Dielmann, Gartner

Collins Bay, Mc Clean deposits, Midwest and Cluff Lake D (Jefferson et al., 2007). Figure 2-4 shows some examples of Athabasca Basin deposits. The Eagle Point deposit is totally fracture controlled basement hosted ore deposit (Jefferson et al., 2007). The Cigar Lake ore deposit is a dominantly clay bounded unconformity type deposit with minor basement hosted lenses and perched ore in the overlying Manitou Falls Formation. Figure 2-4c shows the Dielmann deposit at Key Lake that is both basement hosted and unconformity type uranium deposit (Jefferson et al., 2007).

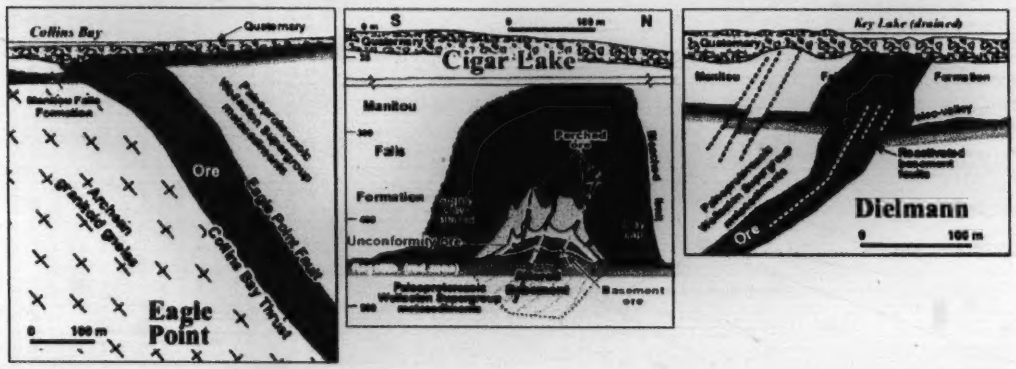

Figure 2-4. Examples of uranium deposits in the Athabasca Basin. a) Eagle Point: Basement hosted uranium deposit, b) Cigar Lake: Typical unconformity ore and c) Dielmann: Both basement hosted and unconformity type deposit (modified from Jefferson et al., 2007).

2.4.2. Monometallic and polymetallic type uranium deposits

Unconformity associated uranium deposits can be also categorized according to the metals that are present in addition to uranium (Ruzicka, 1996). Monometallic deposits contain only traces of metals other than uranium and minor amounts of copper (Jefferson et al., 2007). They are typically located below the unconformity and are fracture controlled basement hosted deposits with small perched sandstone deposits or lenses. Polymetallic deposits, mostly clay bounded, contain sulphide and arsenide minerals with significant amounts of Ni, Co, Cu, Pb, Zn and Mo. Some of those also have significant Au, Ag, Se and Pt content (Jefferson et al., 2007). They are generally located in the 25 m of the geological section above the unconformity, typically in sandstones and conglomerates (Jefferson et al., 2007; Ruzicka, 1996). The difference between these types in due to the differing fluid flow directions associated with deposition (ingress and egress type deposits).

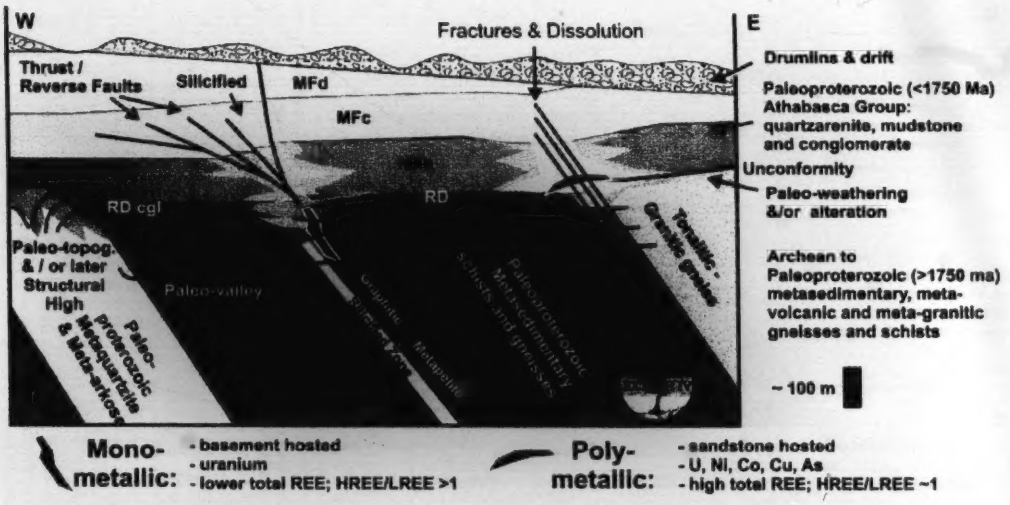

Figure 2-5. Monometallic and polymetallic type unconformity related uranium deposits in the Athabasca Basin (Figure taken from Jefferson et al., 2007).

2.4.3. Ingress and egress type uranium deposits

Another classification of the unconformity type deposit comes from the fluid flow directions and type of alteration. If the fluid flow direction was from the basement to the Athabasca sandstones, this will form an egress type uranium deposit (Figure 2-6). A significant halo of silicification is also formed in this type of deposit because the fluid flow carries minerals from the basement. In contrast, if the fluid flow is from sandstones to the basement, then the ingress type deposit will be formed with a weak alteration zone (Figure 2-6).

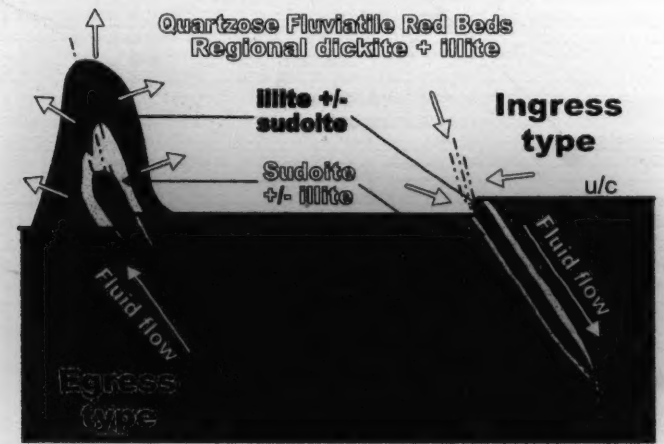

Figure 2-6. Ingress and egress type uranium deposits (Figure taken from Jefferson et al., 2007).

Ore-related illitic alteration is reflected in anomalously high illite proportions and anomalous K_2O/Al_2O_3 ratios within the sandstone (Jefferson et al., 2007). Similarly, local silicification fronts are also present in some of the larger desilicified alteration systems, e.g. Cigar Lake (Andrade 2002). Deposit related silicification is particularly intense within the Athabasca sandstone (Mwenifumbo, 2007).

Illite-kaolinite-chlorite alteration halos (Figure 2-7) are up to 400 m wide at the base of the sandstone, thousands of metres in strike length and extend hundreds of metres vertically above the uranium deposit (Wasyliuk, 2002, for McArthur River; Kister et al., 2003, for Shea Creek; and Bruneton, 1993, for Cigar Lake). This alteration typically envelops the main ore controlling structures, forming plume-shaped or flattened elongate bell-shaped halos that taper gradually upward from the base of the sandstone (Hoeve and Quirt, 1987).

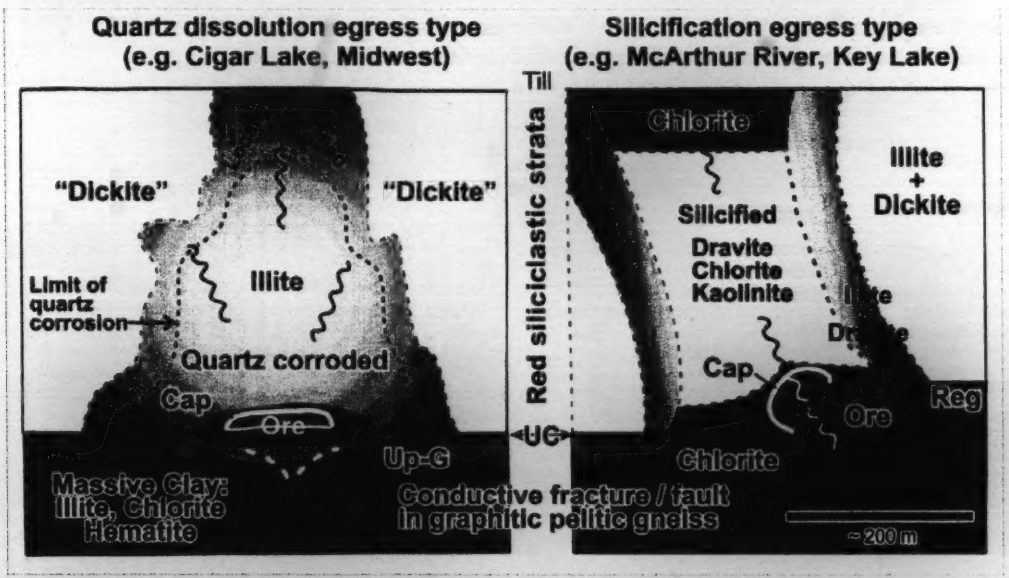

Figure 2-7. Alteration models for egress type deposits in the eastern Athabasca Basin (Figure taken from Jefferson et al., 2007). UC: unconformity, Reg: regolith, Up-G: upper limit of graphite, Cap: black-red hematite cap, Fresh: fresh basement which is Fe-Mg chlorite biotite paragneiss.

Limited alteration occurs in ingress type deposits (Figure 2-6 and 2-7). Most of them are entirely basement hosted, monometallic and have very narrow, inverted alteration halos along the sides of the basement structure, grading from illite ± sudoite on the inside, through sudoite ± illite, to Fe-Mg chlorite ± sudoite on the outside against fresh basement rock (Jefferson et al., 2007).

Some deposits, such as McArthur River, have both ingress and egress characteristics suggesting that they were formed by complex hydrothermal systems with both ingress and egress occurring (Jefferson et al., 2007).

2.5. Geology of the McArthur River Deposit

At the McArthur River mine, the near surface structure is characterized by overburden that is up to 100 m thick. The underlying Athabasca Group rocks (Figure 1-3) are sandstones and conglomerates of late Paleo- to Meso-Proterozoic age (Rainbird et al., 2007). Beneath the unconformity, the crystalline (gneissic) basement comprises the 2.5 - 2.6 Ga Wollaston Group (McMullan et al., 1987). Uranium deposits in the Athabasca Basin are structurally controlled by the Paleo-Proterozoic (sub-Athabasca) unconformity and faults that exhibit a northeast or easterly strike (Ruzicka, 1996). At the McArthur River mine, the deposit formed where the P2 fault intersects the basement. This southeast dipping reverse fault offsets the basement by 60 – 80 metres (McGill et al., 1993). The deposits are P2 North and P2 Main deposits. The age of the faulting at this location could be as young as 1.8 Ga with the age of first U mineralization between 1.7 and 1.65 Ga (Jefferson et al., 2007).

2.5.1. Regional settings of the Mc Arthur River deposit

2.5.1.1. Athabasca group stratigraphy

The middle Proterozoic Athabasca Group consists of, from top to bottom, the D, C and B units of Manitou Falls formation and the Read Formation (formerly MFa) (Ramaekers, 1981; McGill et al., 1993, Jefferson et al., 2007). Manitou Falls D member (MFd-Dunlop) is 180 m thick and consists of fine grained, well sorted sandstone (McGill et al., 1993, Jefferson et al., 2007). Manitou Falls C member (MFc–Collins) is 85 m thick and consists of quartzarenite with minor quartz pebbly beds, mudstone interbeds, clay intraclasts and conglomerate interbeds (McGill et al., 1993, Jefferson et al., 2007). The Manitou Falls B member (MFb – Bird) is 125 m thick and characterized by conglomeratic pebble beds, containing concentrations of heavy minerals and primary hematite (McGill et al., 1993). It has quartz-pebble conglomerate, quartz-pebbly quartzarenite, thin mudstone and siltstone interbeds (Jefferson et al., 2007). Read Formation (RD) comprises discontinuous basal conglomerate, intercalated coarse sandstone,

conglomerate and red mudstone (McMullan et al., 1987; Mwenifumbo et al., 2004).

2.5.1.2. Wollaston group stratigraphy

The basement rocks below the unconformity comprise two distinct sequences of metasedimentary rocks: (1) the pelite sequence and (2) the quartzite sequence (McGill et al., 1993). The hanging wall of the P2 fault belongs to the pelitic sequence, while most of the footwall rocks belong to the quartzite sequence.

2.5.2. Alteration at the McArthur River mine

Studies of the Athabasca sandstones have revealed two distinct alteration patterns. These can be classified as 1) desilicification and illitization, and 2) silicification, kaolinization and dravitization (Matthews et al., 1997) with the zone of alteration characterized by the clay mineralization. The first type shows clay enrichment whereas the second type shows clay depletion and silicification. Alteration at the McArthur River site is of type 2 with intense silicification and weak bleaching of the sandstone, thus there is very little hydrothermal clay alteration. This is consistent with the regional pattern of alteration that exhibits desilicification in the northeast portion of the Athabasca Basin and silicification in the south (Matthews et al., 1997). During silicification, silica is deposited by hydrothermal fluids and fills pore spaces and replaces the other minerals. This increases the resistivity of the rock and can be used in EM exploration.

Bleaching is caused by hydrothermal fluid flow that removes the coloured minerals from the sandstone. At McArthur River, bleaching has affected the first ~200 m of sandstones below the overburden. This includes the MFd and the upper part of the MFc formations. Bleaching is weak at other levels where most silicification occurs. Silicification increases significantly below 375 m and it is weak above this depth (McGill et al., 1993). McGill et al., (1993) suggested that the main source of silica was the basement quartzite rocks, but it is unlikely to be the source of uranium. McGill et al. (1993) and Matthews et al. (1997) showed anomalous uranium content (> 1 ppm), boron content as dravite (> 1000 ppm), chlorite content (> 10 %) and intense clay content. All these alteration minerals indicate that intense silicification occurred during the formation of the Mc Arthur

River deposit. This silicification can lead to high electrical resistivity that provides a target for the geophysical methods discussed in this thesis.

2.5.3. Mineralization

The P2 thrust fault is the primary structure that has controlled uranium mineralization at the McArthur River mine (Figure 2-8). According to McGill et al., (1993), the distribution of the mineralization can be categorized in four types:

1) Within the Athabasca Group and the hanging wall of the P2 fault,

2) Within the footwall parallel of the P2 fault

3) Along narrow horizontal zones of the footwall unconformity,

4) Within zones of structure which extend deep into the hanging wall basement rocks and disrupted FW quartzite.

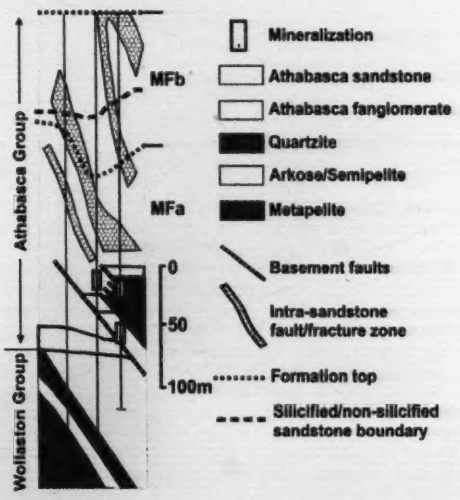

Figure 2-8. Typical geological cross section of the McArthur River P2 North deposit and the P2 fault (Figure taken from Györfi et al., 2004). Pink rectangles show the mineralization corresponds to the first three categories listed below.

Mineralization at the McArthur River mine shows both basement hosted and unconformity hosted mineralization whose formation requires both ingress and egress type fluid flow.

2.6. Geological Exploration Criteria

Having reviewed the characteristics of the Athabasca Basin uranium deposits, it is important to consider how this type of deposit can be detected in a

geological and geochemical exploration project. Some of the important geological and geochemical data that may indicate the presence of uranium mineralization include:

1) *Irregularities in the depth of the unconformity.* Jefferson et al., (2007) showed that variations in unconformity depth can be associated with uranium mineralization.

2) *The presence of basement complexes of highly deformed and metamorphosed Archean orthogneisses and paragneisses.* These complexes are known to have high uranium content (Jefferson et al., 2007).

3) *Zones with high graphite content.* This includes both graphitic strata and graphite bearing faults in the basement (Jefferson et al., 2007). Uranium ore is often concentrated at the intersection of the unconformity and reverse faults. Many uranium deposits in the eastern Athabasca Basin are close to the ancient unconformable contact between the Archean granitoid gneiss and gneiss that contains numerous graphitic units.

4) *Zones of mineral alteration.* The hydrothermal flow that forms the uranium deposits also produces alteration halos that contain illite (potassium alteration) and dravite (boron alteration). Alteration halos may also exhibit increases or decreases in the silica content. These halos can be detected with mapping and drilling, and can provide a strong indication that uranium mineralization may be present at depth (Jefferson et al., 2007). Erosion can transport these alteration products into the surficial deposits where they can be mapped.

5) *Areas of pre-existing complexity along basement structures.* This includes regions such as the Wollaston – Mudjatik transition zone and intersecting faults (Jefferson et al., 2007).

6) *Paleovalleys that formed during the initial deposition of the Athabasca sandstones.* These are exploration targets because paleovalleys are convenient environments for enhanced fluid flow. The porosity and permeability is high which is necessary for the mineral deposition (Jefferson et al., 2007).

7) *Anomalous levels of radioactive elements in groundwater and lake sediments.* Anomalies in radioisotopes of U, K and Th can give a direct indication of uranium bearing minerals (Jefferson et al., 2007).

9) *Anomalous levels of gamma ray emissions in surficial deposits*. Use of these data require an understanding of the fact that glaciation could have transported these material over significant distances (Jefferson et al., 2007).

These exploration criteria are rarely used individually for uranium exploration and are most effective when used in combination. Both surface mapping and drilling are needed to locate possible zones of mineralization. The geophysical methods described in the next chapter can extend coverage into the subsurface.

2.7. Summary

At the McArthur River mine, a 550 m thick sequence of Athabasca Group sandstones unconformably overly the 2.5 - 2.6 Ga Wollaston Group basement rocks. The uranium deposits formed where a basement fault intersects and has offset the unconformity. The fault provides a conduit for hydrothermal fluid that formed the mineral deposit. Oxidizing basinal fluids carried uranium from the sandstones and reducing fluids carried other minerals such as silica from the basement rocks to the unconformity through the fault (Figure 1-3). This deposited uranium at the top of the fault near the unconformity and silicification occurs above the unconformity due to the fluid flow. Prior to uranium ore deposition, intense silicification developed where ascending fluids flooded the sandstone with quartz. Significant silicification surrounds the ore deposit at the McArthur River (Ruzicka, 1996).

From a geophysical perspective, several features of these deposits may give rise to an anomaly in geophysical properties (the alteration zone, the ore zone, the unconformity and the graphitic fault). The type of alteration is significant because a zone of reduced silica and increased clay concentration may give lower density, low magnetics, low resistivity and low velocity values. In contrast, zones with increased silica content will exhibit the increases in these properties. Thus, geophysical methods can potentially delineate zones of alteration. Seismic exploration can image the unconformity and the intersecting faults. Graphitic faults are strong electrical conductors which are an ideal target for electrical and electromagnetic methods.

3. PREVIOUS GEOPHYSICAL STUDIES FOR URANIUM EXPLORATION IN THE ATHABASCA BASIN

3.1. Introduction

In the previous chapter, the geological characteristics of unconformity uranium deposits were reviewed. Subsurface investigation by drilling is expensive and is effective with guidance from geophysical exploration. In this chapter, previous geophysical studies are reviewed and used to give context to the audio-magnetotelluric (AMT) data that are the focus of this thesis.

Many geophysical methods have been used in uranium exploration in the Athabasca Basin. As in other types of exploration, both direct and indirect methods have been used. Direct methods attempt to directly image the zone of uranium mineralization, but these are generally not very successful for deep deposits as the resulting signal is weak at the surface. The best example of this type of exploration is the radiometry method that is used for defining areas with radioactive minerals such as K, U and Th. It is very effective for shallow deposits, but is less effective for the deeper ones. Indirect methods look for structures that could potentially host a uranium deposit, but do not directly locate the zone of mineralization. For example, electromagnetic (EM) methods can locate graphitic faults that are often spatially associated with uranium mineralization. Seismic exploration can image the unconformity and basement faults that could host uranium deposits. Gravity exploration can potentially delineate zones of silicification or alteration associated with uranium deposition. Magnetic data can delineate basement structures that may control the location of uranium deposition.

Initial uranium exploration typically utilizes regional airborne geophysics to define areas of potential uranium mineralization. These studies include airborne radiometry, airborne EM, aeromagnetic and airborne gravity surveys. After identifying prospective uranium zones, follow up geophysical surveys on the

ground use electrical and EM methods, as well as gravity, magnetic, seismic and radiometry methods.

The Athabasca Basin has been the focus of intense uranium exploration for more than thirty years. In recent years, many shallow deposits have been extracted and exploration has moved into the deeper part of the basin. Existing exploration methods have ceased to be effective when the unconformity is at depths in excess of 200 m. The Canadian government and its industrial partners initiated the EXTECH-IV project in 1999 to address this problem. The main purpose was to identify new approaches for locating deep uranium deposits. The McArthur River mine was chosen as a test site for EXTECH IV. By collecting geophysical and geological data of a known deposit, subsurface information was available for validating geophysical methods.

3.2. Regional Airborne Geophysics

3.2.1. Airborne radiometry

Airborne radiometric data have been collected over the entire Athabasca Basin and surrounding region. These data are sensitive to the presence of radioactive minerals in the upper few metres of the subsurface (Milsom, 1989). In the Athabasca Basin, the regional variations have been complicated by the fact that most near surface material has been transported significant distances by glaciation during the ice ages (Campbell et al., 2002). The regional radiometry data are shown in Figure 3-1. Potassium (K), equivalent uranium (eU) and equivalent thorium (eTh) values are generally low compared to the surrounding areas. This is due to the fact that radioactive elements are concentrated in basement rocks which are farther from the surface when the basin is deepest. Lower radioactivity levels are observed on the western side of the basin compared to the eastern side of the basin. This could be due to an increase in radioactivity levels in the Quaternary deposits and eTh rich sandstone facies in the Athabasca Basin. In general, the Athabasca Basin sandstones contain very low concentrations of K and eU, and higher values of eTh. Higher eTh values are found in the eastern part of the basin, including the McArthur River area and are due to the fact that some members of the Manitou Falls Formation (MFa and MFb) are particularly rich in Th-bearing detrital minerals (Campbell et al., 2002). Ratios of certain radioactive elements show some significant variations. The ratio

of eTh/K to eU/K separates the basin from the surrounding area and are highest at the western part of the Athabasca Basin. However, none of these maps show a correlation with the location of known uranium deposits. Thus, while this method can guide reconnaissance exploration, it is not useful for exploration when deposits are deeply buried.

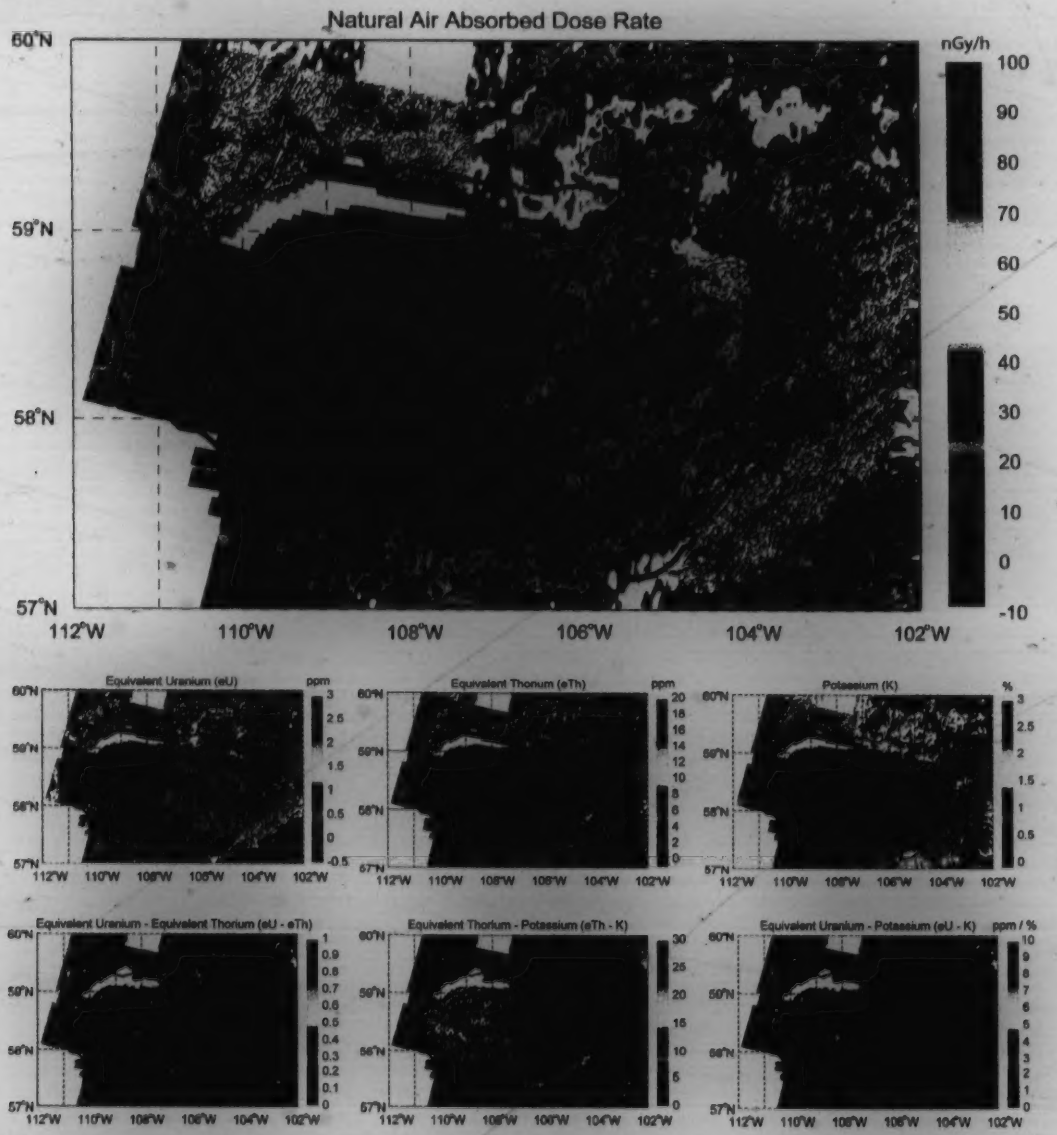

Figure 3-1. Regional radiometry data from the Athabasca Basin. The panel at the top shows the rate of a natural air absorbed dose (also called Total Count). The-mid panels shows the K, eU and eTh and the bottom panels shows the ratios of eU/eTh, eTh/K and eU/K from left to right. The redrawn from data from Geological Survey of Canada. Black line shows the limit of Athabasca Basin.

3.2.2. Aeromagnetic data

Aeromagnetic data is widely used in the early stages of most mineral exploration, including the search for uranium mineralization. It can effectively map the basement geology and allow the identification of basement fault systems and alteration features (Matthews et al., 1997). Figure 3-2 shows regional aeromagnetic data.

Figure 3-2. Total residual magnetic field in the Athabasca Basin and the surrounding area. The Geological Survey of Canada collected the magnetic data at elevation of 305 m with line spacing of 800 m. Dashed line showed one of the low magnetic trends interpreted as the Wollaston Domain – Mudjatik Domain transition zone. Black line shows the limit of Athabasca Basin. Taken from Matthews et al., (1997)

Most of the known unconformity type uranium deposits are located in the magnetic low trends (blue colours) in the eastern Athabasca Basin (Figure 3-2 and 3-3). This is coincident with the boundary of the Mudjatik and Wollaston domains. Northeast trending graphitic faults are also coincident with the magnetic low trends (Matthews et al., 1997). These anomalies could be due to the presence of non-magnetic material within the faults and shear zones that give a magnetic low.

Figure 3.4 shows the first vertical derivative of the total magnetic field. This quantity enhances the short wavelength component and is sensitive to near surface structure. Figure 3.4 shows little correlation between sharp changes in gradients and the locations of known uranium deposits.

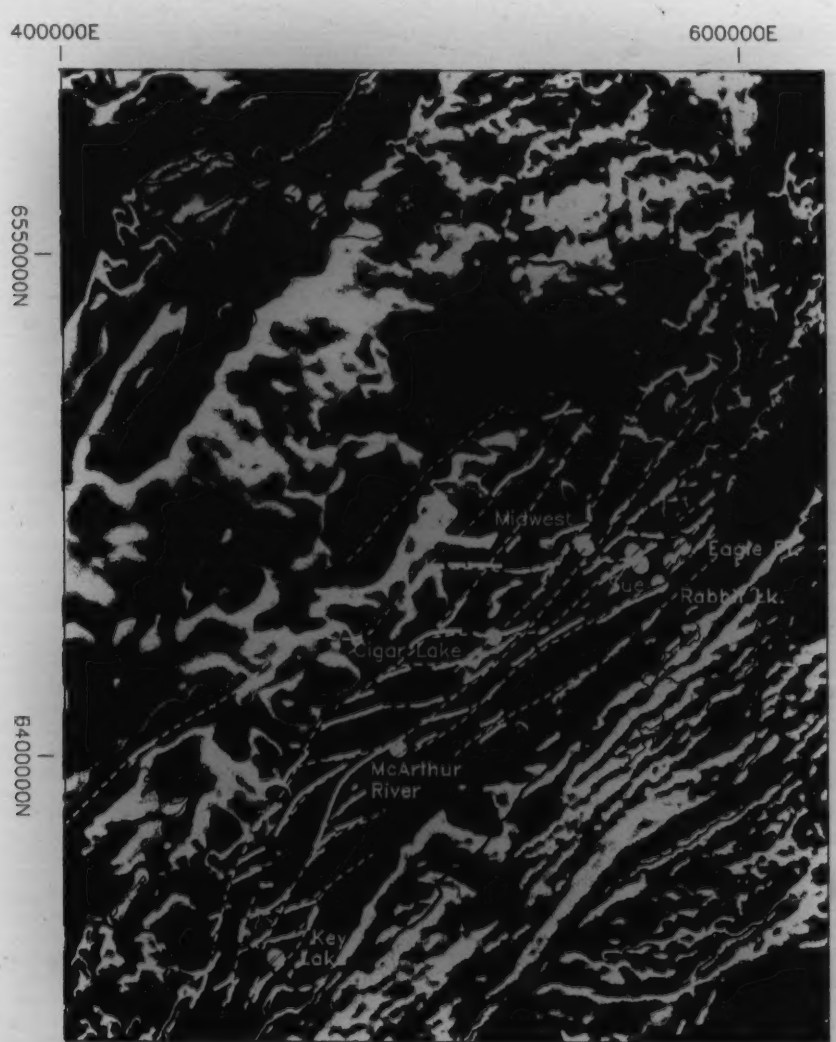

Figure 3-3. The agreement between the magnetic anomaly and basement geology (Figure is taken from Matthews et al., 1997). White dots shows the known uranium deposits, and white lines shows the graphitic conductors mapped by EM studies, the white dashed lines show the shear zones interpreted by EM and the linear trends of low magnetic intensity. Black line shows the border of the Athabasca Basin.

In uranium exploration, aeromagnetic data can delineate the basement structures such as geological domains. However, it cannot effectively locate buried uranium deposits or underlying shear zones.

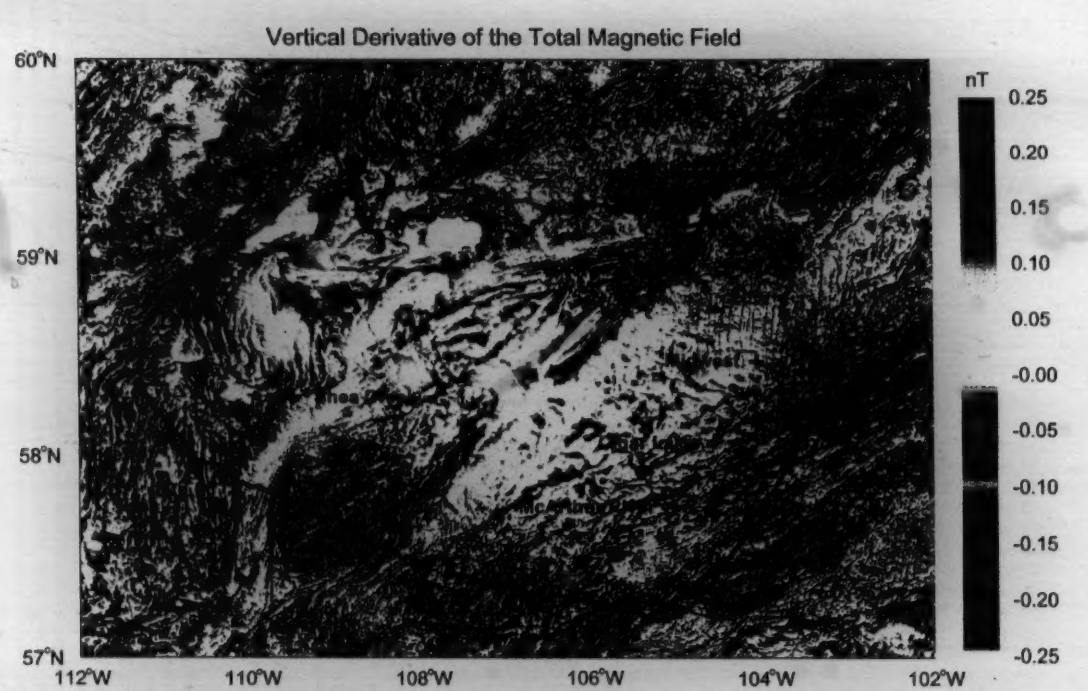

Figure 3-4. Shaded relief map of the vertical derivative of the residual magnetic field of the Athabasca Basin and the surrounding area. + sign shows some of the main uranium deposits of the Athabasca Basin.

3.2.3. Regional gravity data

Regional gravity data have also been used to delineate the basement geology in the Athabasca Basin. The Geological Survey of Canada acquired gravity data with both airborne and land surveys. The average data spacing ranges from 5 to 10 km. Details of data reduction are given by Matthews et al., (1997). An average crustal density of 2.67 g/cm^3 for the Bouguer correction is too high for Athabasca sandstones, and Matthews et al. (1997) accounted for this fact and reprocessed the data (Figure 3-5) using a density of 2.1 g/cm^3.

The Bouguer anomaly shows little correlation with the spatial extent of the Athabasca Basin. This is because the Bouguer anomaly is dominated by variations in basement density, as evidenced by the northeast to southwest strike of the anomalies. The Bouguer anomaly map is characterized by northeast – southwest anomalies with both high and low gravity values. The gravity highs are correlated with granulite facies metamorphic rocks and metamorphic terranes, composed of granitic gneisses and supracrustal rocks, which represents the cores of Archean crustal blocks. The gravity lows are often associated with

amphibolite facies terranes, in part retrograde granulites, composed of granitic gneisses and supracrustal rocks, and in part Hudsonian mylonite zones, for example the Virgin River Shear Zone (Matthews et al., 1997).

Figure 3-5. Corrected Bouguer gravity anomaly map for the Athabasca Basin (Figure is taken from Matthews et al., 1997).

Figure 3-6 shows a two dimensional density model derived from the data on profile AA' in Figure 3-5. The model indicates density variations of less than 0.1 g/cm^3 within the 25 km thick upper crust along the profile (Matthews et al., 1997). Drill hole and seismic data was also used to constrain the sandstone thickness at the Athabasca Basin. Paleovalleys at the unconformity are favourable locations for uranium deposition because they could have been zones of enhanced fluid flow during mineralization. Paleovalleys are an important exploration target and can potentially be detected with gravity exploration. Note that the basement density in Figure 3-6 has very small horizontal variations. It is unlikely that such variations could be detected in field data.

Regional gravity anomalies can provide some constraints on the geometry of basement structures. Changes in the geological domains give a gravity signature, which can guide uranium exploration by defining the different basement domains. However, it is not as useful as magnetic exploration, since gravity data are spatially smoother and less sensitive to small-scale anomalies than magnetic data.

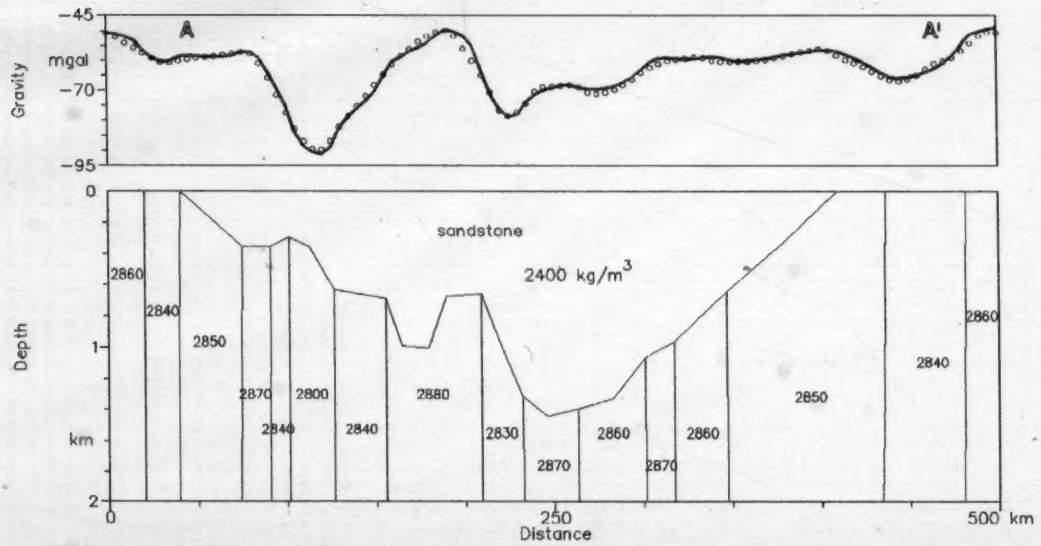

Figure 3-6. Two dimensional gravity model of line A-A' in Figure 3-4. Green circles show the observed gravity data where solid black line shows the fit of the model which was given in the bottom panel. The thickness of the Athabasca sediments is inferred from drill hole and seismic data (Figure is taken from Matthews et al., 1997).

3.2.4. Airborne electromagnetic data

Unconformity uranium deposits are often found with graphite (Jefferson et al., 2007). The low resistivity of the graphite makes these zones electrical conductors that can be detected with EM methods. By using airborne EM methods, initial exploration can cover large areas very easily. Figure 3-8 shows typical electrical resistivity properties in the Athabasca Basin. The Athabasca sandstones and the underlying basement rocks are characterized by high values of electrical resistivity. Alteration zones have variable resistivity depending on the degree of silicification. Silicified zones have high resistivities due to the silica content in pore spaces, while desilicified zones have relatively low resistivities due to enhanced clay content in the pore space. The overburden and lake waters have low resistivities in the Athabasca Basin, and are generally thin enough that they do not affect the EM results. Only thick lake sediments may have limited the depth of penetration of EM methods. Moreover, regolith at the unconformity is generally not a significant conductor (Irvine and Witherly, 2006). The lowest resistivities observed in the Athabasca Basin are the graphitic metapelites in the basement rocks (Figure 3-7).

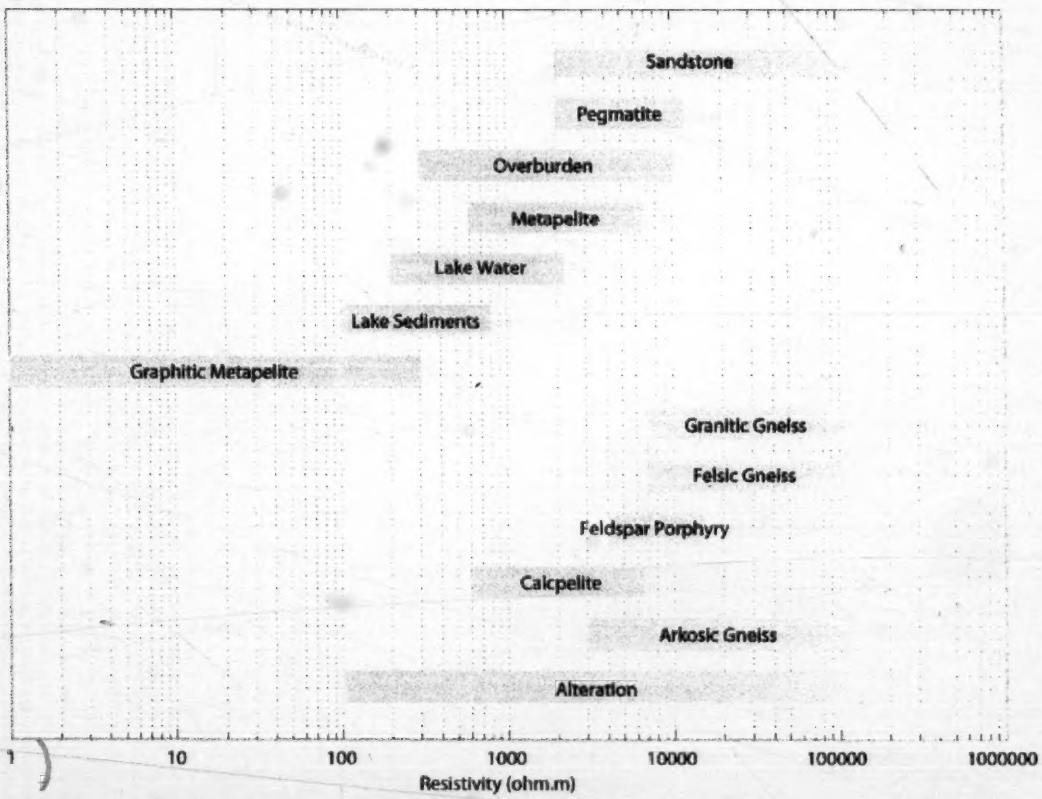

Figure 3-7. Electrical resistivity properties of rocks found in the Athabasca Basin (after Cristall and Brisbin, 2006; Irvine and Witherly, 2006).

Table 3-1. Comparison of the VTEM and the MEGATEM system configurations (http://www.geotechairborne.com/FILES/CaseStudies/VTEM_MEGATEM_2006.pdf).

	VTEM	MEGATEM
Transmitter loop area	531 m^2	406 m^2
Pick dipole moment	615,000 NIA	1,540,000 NIA
Transmitter current	289 A	630 A
Transmitter number of turns	4	6
Transmitter height	30 m	120 m
Reciever height	30 m	70 m
Survey speed	22 m/s (80km/h)	65 m/s (9234 km/h)
Recoding rate	10 /s	4 /s
Distance between samples	2.2 m	16.3 m

Unconformity deposits can lie at a significant depth in the Athabasca Basin, and the emphasis has been on airborne EM methods capable of deep exploration. These include time domain MEGATEM and VTEM (Versatile Time-domain Electromagnetic) because of their large dipole moment and relatively high signal-to-noise ratio (Irvine and Witherly, 2006). Both systems were designed for deep exploration and their advantages and disadvantages are discussed by Irvine and Witherly (2006). Table 3-1 shows the comparison of the MEGATEM and VTEM specifications.

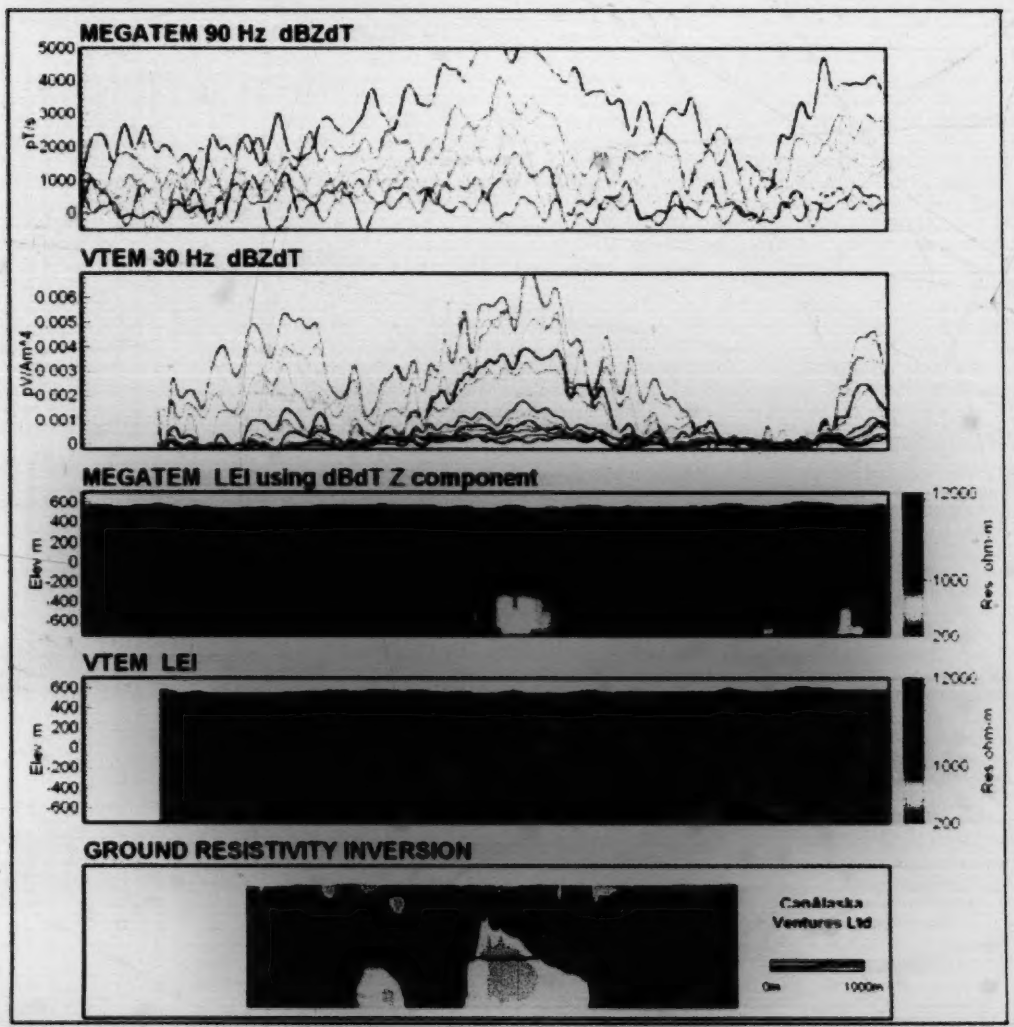

Figure 3-8. MEGATEM, VTEM and ground resistivity data and conductivity depth sections of the line in the Athabasca Basin (Figure is taken from Irvine and Witherly, 2006). (LEI: Layered Earth Inversion, dBZdt: time derivative of the z component of the B field).

Figure 3-8 shows an example of these methods from an undisclosed location in the Athabasca Basin, with a comparison between the MEGATEM, VTEM and ground resistivity data collected with a pole – pole electrode array. The graphitic basement conductor was imaged with hot colours below the known unconformity depth approximately at 800 m. Irvine and Witherly (2006) suggest that the green coloured area with mid resistivity values above the conductor (Figure 3-8) may indicate the presence of an alteration zone. Extremely low background amplitude indicates that both sandstone and basement resistivities are very high (>50000 Ω.m). The ground resistivity survey was consistent with the airborne EM results, since it also imaged the deep conductor below the unconformity depth. However there is also another strong conductor at the left of the main conductor which was not imaged by the AEM data. Inversion of the ground resistivity data also generated some small scale, shallow conductors, which indicates that the ground survey has greater sensitivity to the small scale structures than the AEM survey.

However, none of these methods gives a clear image of the deep basement conductor. They give information about the presence of a conductor but cannot define the geometry of the basement conductors. Therefore, new EM methods are needed to define conductor geometry at greater depths (1-2 km range).

3.3. Previous Geophysical Studies at the McArthur River deposit

In the previous section, regional scale geophysical studies were shown to be effective tools to locate prospective areas for detailed ground follow up. In this section, geophysical studies on the kilometre scale at the McArthur River P2 North deposit are reviewed. As described above, indirect geophysical methods are primarily utilized in the Athabasca Basin. The exploration strategy is to locate (a) basement conductors that terminate at the unconformity and (b) define the spatial extent the alteration zones. Basement conductors are likely basement faults containing graphite related to the uranium mineralization. Significant alteration (silicification) above the unconformity indicates that extensive fluid flow occurred through these faults, which is a necessary condition for uranium mineralization. Thus, geophysical exploration methods are focused on detecting basement faults, and zones of silicification above the unconformity. These include:

1) seismic imaging of the unconformity and basement faults

2) gravity exploration that can delineate silicified zones above the deposits

3) magnetic data that can delineate basement structures,

4) borehole studies to enhance the lithological information as well as the physical properties and

5) EM methods that are used to map the graphitic faults in the basement

3.3.1. Seismic imaging at the McArthur River deposit

Historically, seismic reflection has been primarily used in hydrocarbon exploration. However, there has been a recent trend to apply these methods to mineral exploration (mostly base metals) in hard rock environments (Milkereit et al., 2000; Salisbury et al., 2000; L'Heureux et al., 2005). This application of seismic exploration is quite different to hydrocarbon exploration and a number of data processing issues have had to be addressed. Crystalline rock is more heterogeneous than sub-horizontal sedimentary sequences and this can causes significant seismic scattering. Low signal to noise ratio and a lack of prominent marker horizons add to the difficulty of exploration (L'Heureux et al., 2005). In general, 2D seismic interpretation must be used with caution. If the subsurface structure does not have a well defined strike or dip, then out of plane reflections (sideswipe) can seriously contaminate the 2D reflection images and produce serious artefacts (Milkereit et al., 2000). To evaluate the ability of seismic reflection to contribute to unconformity uranium exploration, a high-resolution regional seismic reflection survey was carried out as part of the EXTECH IV project (Figure 3-9). Details of the seismic data processing was described by Gyorfi et al. (2007).

The objectives of the seismic survey were:

1) to map the stratigraphy of the Athabasca group sandstones,

2) to image the unconformity between the sandstones and the basement,

3) to characterize the seismic attributes of the unconformity

4) to locate faults that control the deposition of the uranium deposit,

5) to attempt to image the ore deposit directly, and

6) to define the regional structures (White et al., 2007).

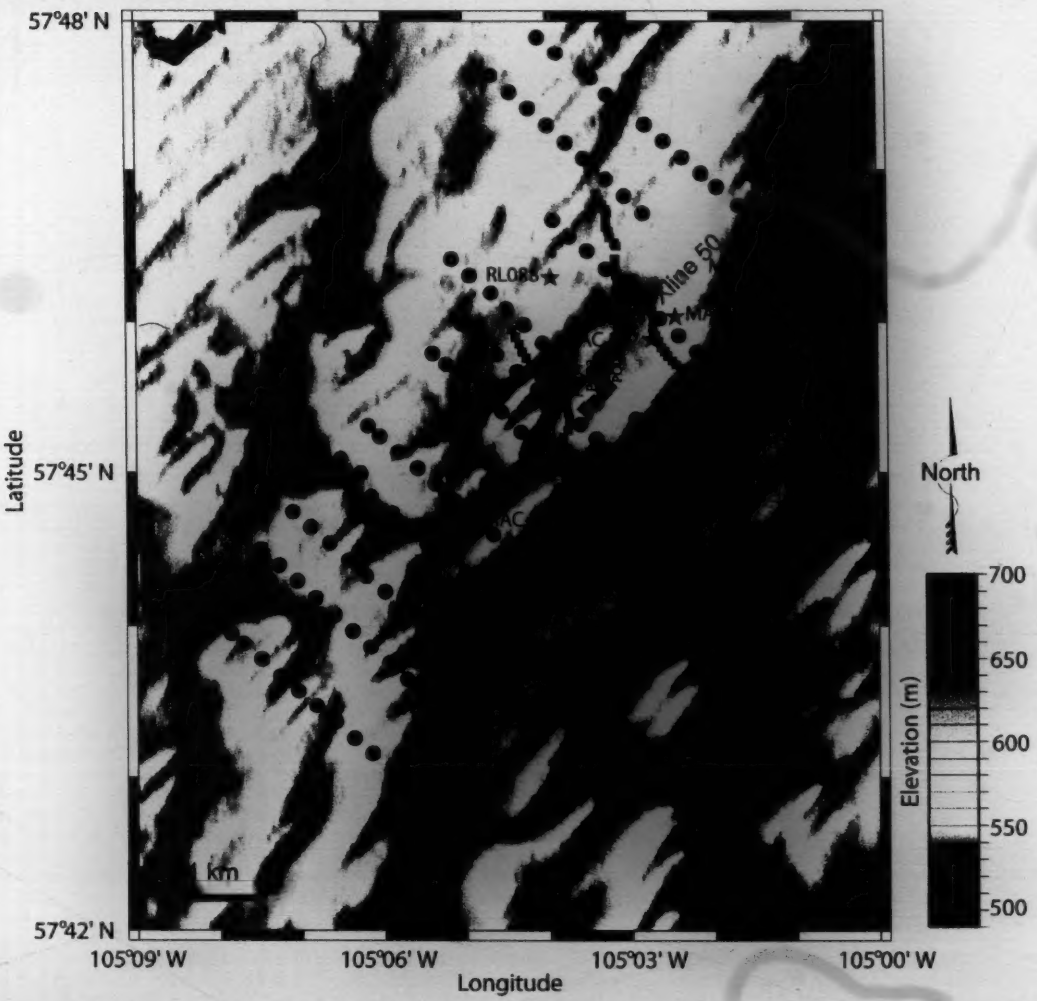

Figure 3-9. Location of the seismic lines (blue) at the McArthur River property with the AMT stations (red circles) and borehole locations (black stars). Black diamond signs show the uranium pods. Coordinates of the seismic lines were taken from White et al. (2007). Dashed blue line shows the location of the cross-line 50.

Hajnal et al. (2002; 2003; 2007) interpreted regional structures and showed that a high velocity zone above the unconformity was coincident with the P2 North ore body. This was interpreted as a zone of alteration. The east dipping P2 fault was imaged beneath the ore deposit that was interpreted as 2500 m thick structure that continues down to 4000 m depth. Sub-horizontal bright reflectors and north dipping sub-parallel reflectors were also imaged in the deeper parts of the McArthur River as well as the reflection from Moho (Hajnal et

al., 2002). White et al. (2002; 2007) and Györfi et al. (2004; 2007) describe Line 12 (southern seismic profile), and Györfi et al. (2002; 2007) describe Line 14.

On Line 12, there is a shallow, laterally continuous reflection at approximately 120 m depth but its origin is unknown. A laterally continuous reflection was imaged at depths of 400 – 600 m, and was interpreted as the unconformity. Laterally limited sub-horizontal reflections were also imaged between these reflectors, which might represent silicification or porosity. There is also evidence of an angular disconformity. The P2 fault was also detected beneath station 400.

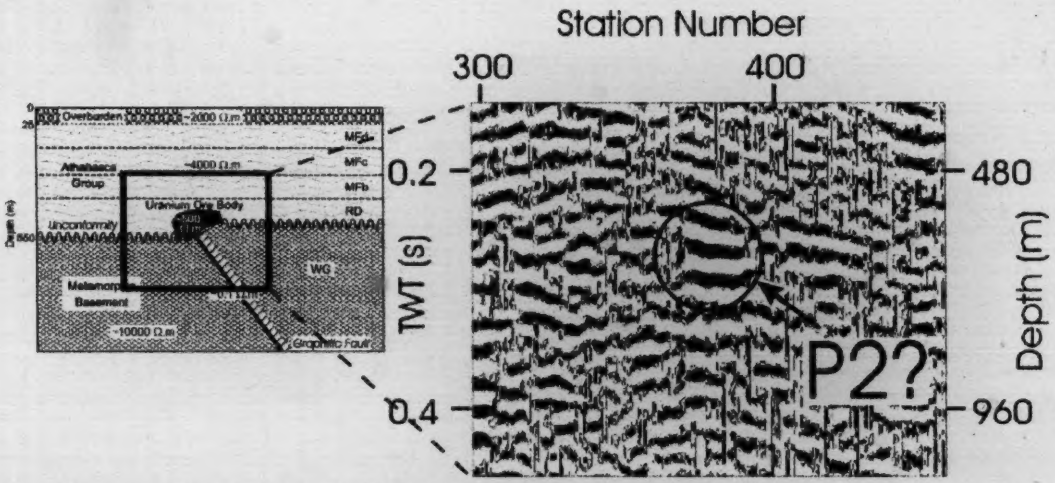

Figure 3-10. Possible seismic reflection response of the uranium deposit itself around the P2 ore body (modified from White et al., 2002).

Is it possible to directly image the uranium deposit? White et al. (2002; 2003; 2007) suspected that they might be observing the seismic signature of the McArthur River uranium deposit on Line 12. Figure 3-10 shows a detail of the seismic section approximately around the ore body. Assuming an average velocity of 4800 m/s (Table 3-2), the depth was estimated as 500-550 m below the surface. However, it is not certain if this reflection is the ore body. It could be a reflection from the associated halo of silicification (White et al., 2002).

Synthetic seismic modelling studies were also carried out. The aim of these studies was to define the resolution and the limitations of the seismic data. The details can be found in White et al. (2002; 2007). These results of the modelling study suggest that the seismic diffraction response is associated with the uranium deposits.

The final interpretation of lines 12 and 14 by Györfi et al. (2007) are shown in Figure 3-11 and Figure 3-12 respectively. Line 14 is located at the northern part of Line 12, and it is also perpendicular to the P2 fault trend (Figure 3-9).

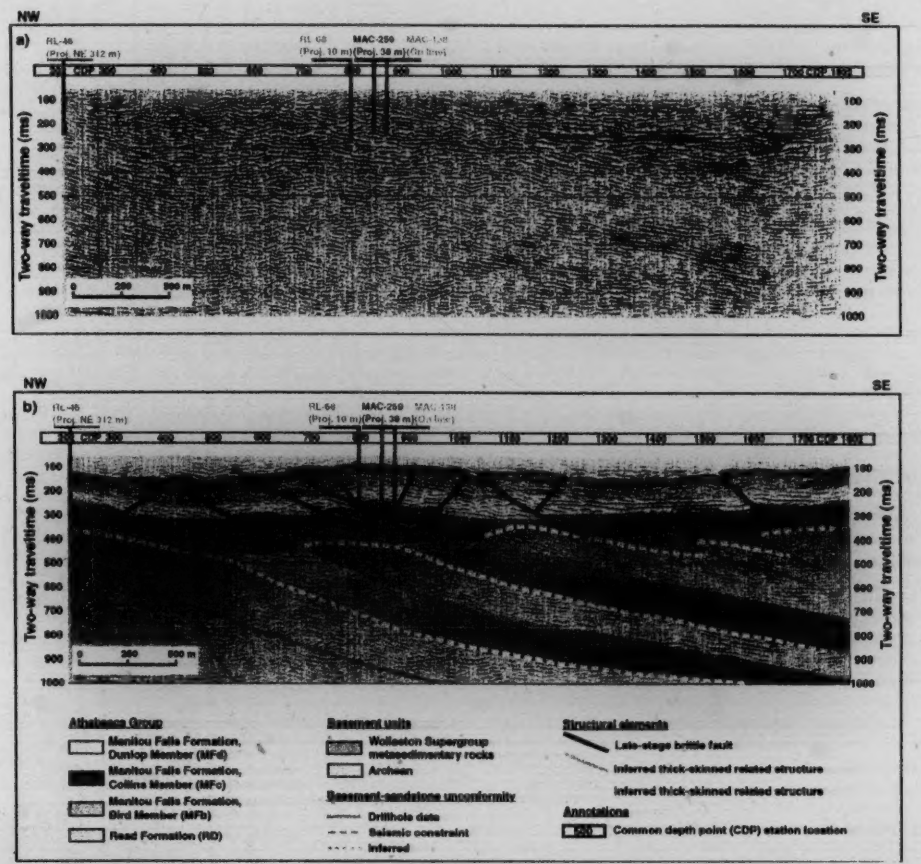

Figure 3-11. Top panel shows the final migrated data and the bottom panel shows the interpretation of the 2D high resolution seismic Line 12 (Figure is taken from Györfi et al., 2007). Note that the line is perpendicular to the P2 fault trend (see Figure 3-9).

The interim interpretation of Line 14 is 1) the P2 fault is very complex deformation zone possibly of transpressive nature, 2) the Wollaston Group was involved in the same deformation process as the Athabasca sandstone faults, 3) imaging the unconformity is limited due to the thickness of the regolith, 4) internal discontinuities located at different stratigraphic levels within the sandstone, and 5) the internal sandstone discontinuities and the complex image of P2 fault are consistent with the theory of syn-depositional faulting related to P2 structure (Györfi et al., 2002).

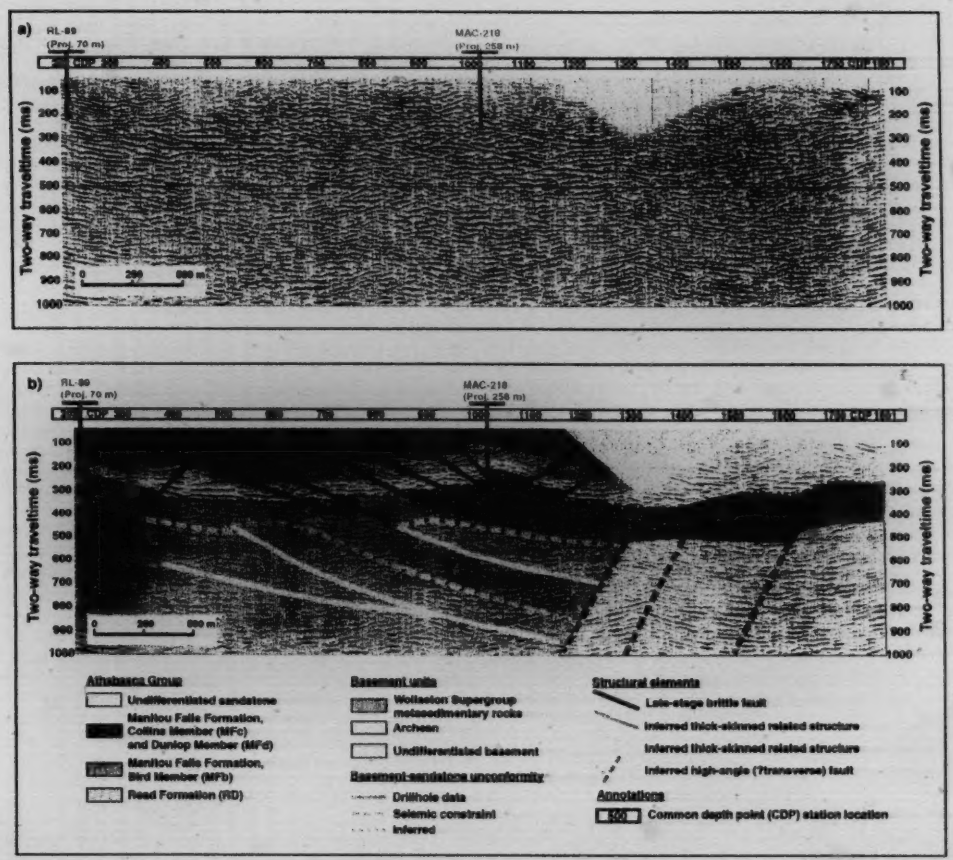

Figure 3-12. Top panel shows the migrated seismic section for Line 14, the bottom panel shows the interpretation (Figure is taken from Györfi et al., 2007). The unconformity at the sandstone / basement interface was well imaged. Intersecting faults and fault offsets were also identified in the seismic section.

All the figures above show structures normal to the P2 fault. However, Györfi et al. (2004) also exhibit the result of the cross-line 50 that is parallel to the P2 fault trend. Figure 3-13 shows the preliminary interpretation of this cross-line. This figure supports the idea that high-angle transtensional faults are controlling the unconformity and laterally offsetting the P2 trend. In summary, seismic exploration at the McArthur River mine has shown that useful information can be obtained from modern reflection data. A number of the objectives listed above have been addressed as follows:

1) Seismic data could not readily distinguish between different members of the Manitou Falls formation.

2) The unconformity is well imaged by the seismic data.

3) The seismic attributes of the unconformity are significant but they need more constraints from drilling to relate these for the geological significance.

4) The P2 fault and many other fault zones were well imaged.

5) There is no convincing seismic signature of the uranium orebody.

6) The depth of the basement (unconformity) and other regional features such as Moho can obtained from the seismic data (White et al., 2007).

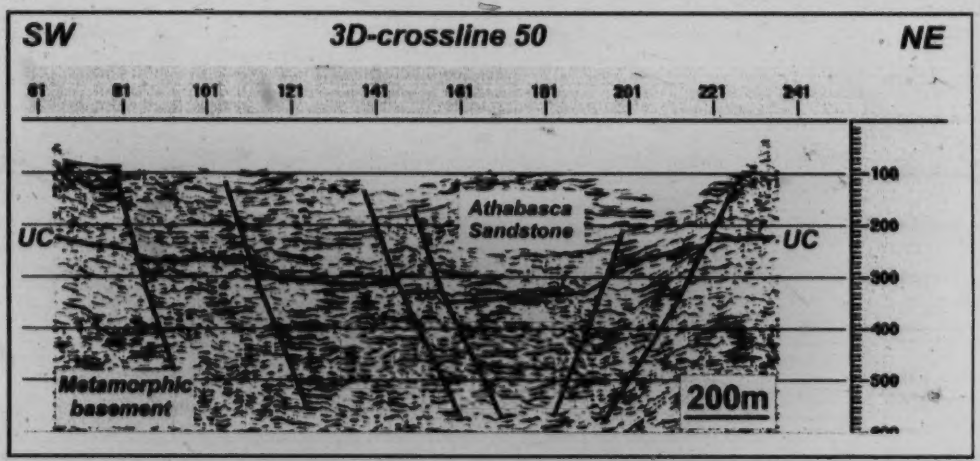

Figure 3-13. Interpretation of the cross-line 50 (Figure is taken from Györfi et al., 2004). Note that this line is parallel to the P2 fault trend.

3.3.2. Gravity exploration at the McArthur River deposit

Several factors can produce a gravity anomaly associated with an unconformity uranium deposit. Wood and Thomas (2002) used known density values to estimate the magnitude of anomalies that might be observed in the Athabasca Basin. Since the sandstones have a lower density than the basement rocks, changes in basement depth caused by faulting could give anomalies in the range 0.5 - 1 mGal. Topography on the unconformity surface could give anomalies 0.5 – 2 mGal. Zones of alteration are anticipated to give gravity lows in the range 0.4 – 1 mGal while silicification could increase the density and give a small positive Bouguer anomaly. These gravity anomalies are small and may not be distinguishable from background geological noise in field data. To determine if these anomalies could be detected over a known uranium deposit, a 27 km long high-resolution gravity profile was collected across the McArthur River deposit as

part of the EXTECH IV project (Figure 3-14). The average station spacing was 50-100 m (Wood and Thomas, 2002) and data were reduced with standard procedures. The Bouguer anomaly was computed with a surface density of 2 g/cm^3 that is typical for the Athabasca sandstones (Wood and Thomas, 2002). The Bouguer anomaly data are shown in Figure 3-15 and show variations of 2.9 mGal along the profile (Wood and Thomas, 2002).

Figure 3-14. Bouguer gravity anomaly map of the McArthur River Mine area. (Figure is taken from Wood and Thomas, 2002). The thick black line shows the high resolution gravity profile and the blue dot shows the McArthur River deposit. Black dots shows the gravity stations. Contour interval is 0.5 mGals.

As in most gravity data, the separation of regional and residual effects was complicated in these data (Telford et al., 1990). This occurs because shallow structure causes short spatial wavelength anomalies and deeper structure causes longer wavelength anomalies. Short wavelength gravity anomalies were observed with wavelengths less than 500 m and were found to be partially correlated with surface elevation (drumlins). Drilling revealed that the overburden thickness was also correlated with the elevation and in the range 20-120 m (Wood and Thomas, 2002). However, new information from seismic and gravity studies indicated that such changes due to the irregularities in the overburden

sandstone contact can be also related to the silicification (Thomas and Wood, 2007). Thus, these short wavelength features were included in the model. Long wavelengths gravity anomalies (>2500 m) are due to deeper structure such as variations in basin depth and basement density. These effects are not of primary interest in a study of the uranium deposits; however, short wavelength anomalies superimposed on long wavelength ones were used to model the silicified zones which was the main objective of the gravity study. Thus, long wavelengths were also included in the modelling study (Thomas and Wood, 2007).

To evaluate if alteration could be detected, the data analysis was focussed on intermediate wavelength (500–1800 m) anomalies (Figure 3-15). A density model was constructed with constraints from seismic, magnetic and borehole data (Wood and Thomas, 2002). The modelling shows the silicification with wavelength from 400 to 1700 m with amplitudes ranging from 0.2 to 0.4 mGal (Thomas and Wood, 2007).

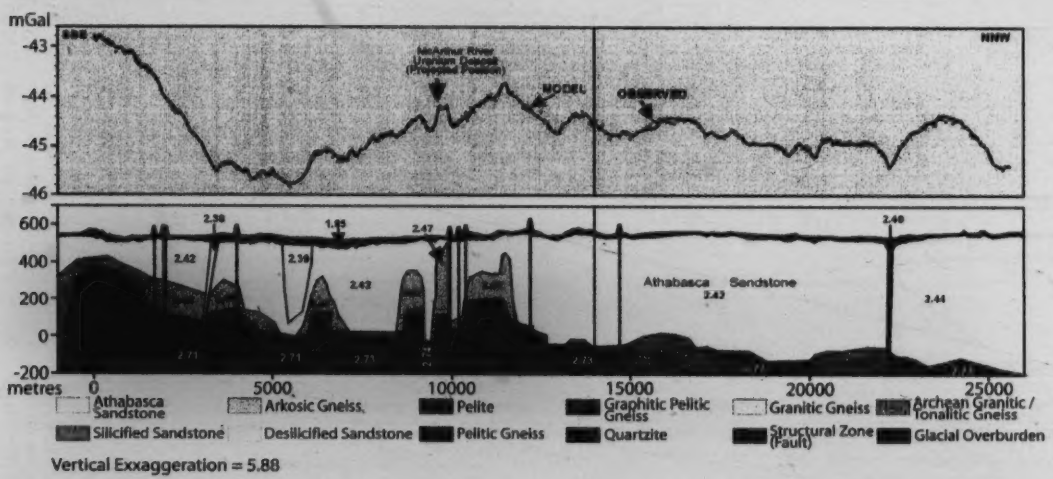

Figure 3-15. Gravity modelling of the intermediate wavelength anomalies (Figure taken from Wood and Thomas, 2002).

To summarize, a density model was generated from the gravity data that was consistent with the known subsurface structure at the McArthur River. This included (1) locations of fault controlled basement relief, (2) changes in the overburden thickness and (3) density changes caused by alteration (silicification / desilicification) above the unconformity. However, the inherent non-uniqueness of gravity data must always be considered, since different density models can be found that also fit the observed data. In combination with other geophysical data,

gravity data can map the basement depth and delineate the alteration zones. However, gravity data alone are insufficient to give useful information about the uranium mineralization.

3.3.3. Magnetic studies at the McArthur River deposit

The regional scale magnetic studies, presented earlier in this chapter, reflect the characteristics of the basement rocks. To focus on structures around the deposit, it is important to understand the magnetic properties expected in the subsurface. If there is no contrast in magnetic properties then magnetic exploration will not be useful. Table 3-2 shows the ranges of the magnetic susceptibilities reported for basement rocks (Annesley and Madore, 1993); Thomas and McHardy, 2007). Note that Athabasca sandstone is magnetically transparent due to the low susceptibility values, and this allows the underlying basement domains to be differentiated.

Table 3-2. Ranges of magnetic susceptibilities in the Wollaston domain (after, Annesley and Madore, 1993; Thomas and McHardy, 2005).

Rock Type	Number of samples	Susceptibility (x 10^{-3} SI)
Archean granitoid rocks	279	0.2 – 0.7
Aphebian granitoid rocks	15	0 – 8.0
Pegmatite	62	0 – 0.8
Quartzofeldspathic gneiss	85	0 – 8.8
Albite gneiss	18	0 – 17.6
Psammatic gneiss	37	0 – 0.4
Metaquarzite	15	0 – 0.2
Pelitic and / or psammopelitic gneiss	259	0 – 3.8
Graphitic pelitic gneiss	97	0 – 0.4
Chlorite schist	9	0 – 0.4
Calc-silicate gneiss	24	0 – 0.5
Amphibolite (metagabbro, metadiorite)	50	0 – 100.5
Banded iron formation	3	0 – 11.3

High susceptibility values generally indicate higher content of magnetic minerals. In high magnetic latitudes (such as the study area) zones of high susceptibility correspond to positive magnetic anomalies (assuming only induced

magnetization). Thus, magnetic highs and lows can be associated with the type of basement rock. Rocks with lower susceptibility will generally exhibit magnetic lows e.g. psammatic, pelitic, psammopelitic and graphitic pelitic gneiss forms at the fault and shear zones.

A detailed view of the aeromagnetic data at the McArthur River Mine is shown in Figure 3-16. The data collection was described in the Section 3.2.2. The remnant magnetization was ignored since no ultramafic rocks have been reported in this area. Only in ultramafic rocks does remnant magnetization generally exceed that of the induced magnetization.

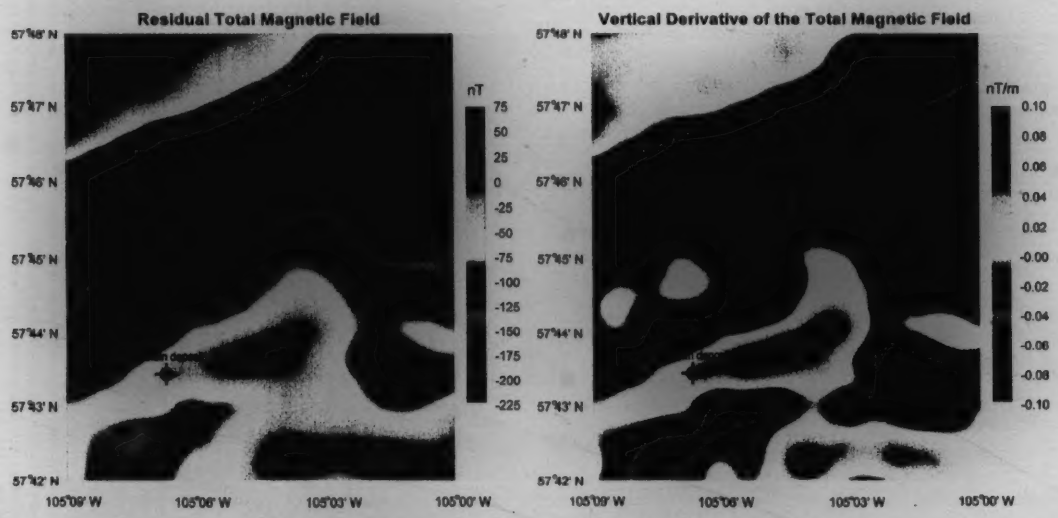

Figure 3-16. Residual magnetic field and its vertical derivative at the McArthur River mine. Black symbols indicate the uranium deposits. Aeromagnetic data was provided by Geological Survey of Canada.

The low magnetic trend extending southwest-northeast has been interpreted to represent a zone of Aphebian metasedimentary basement rocks. These rocks have a relatively low susceptibility (Table 3-2) and frequently host graphitic conductors (Matthews et al., 1997). Thomas and Mc Hardy (2007) pointed out that the magnetic lows near McArthur River deposit are often associated with pelitic - psammopelitic gneiss and lesser quartzite, intermediate levels with psammatic gneiss and highs with granitoid units. While the magnetic low can define rocks that are related to the uranium deposits, there is no direct expression of the uranium deposits in the magnetic field data (Thomas and McHardy, 2007).

Ground magnetic data can give larger anomalies than airborne data, since they are collected closer to the target. Ground magnetic data at McArthur River were described by Matthews et al. (1997) who stated that "*the P2 conductor follows a poorly defined, northeast – southwest trending magnetic corridor, interrupted by several east – west trending breaks, which coincide with the interpreted strike of transcurrent faults*". This suggests that more detailed ground magnetic exploration may be a useful addition to regional airborne coverage.

In summary, the magnetic method is useful in the initial stages of exploration. As an indirect exploration method it can delineate the different basement domains, and may identify to locate structures that may host uranium deposits. However, it is not able to directly detect the uranium deposit or locate graphitic faults.

3.3.4. Borehole data from the McArthur River deposit

Borehole data can be used to extend surface geophysical measurements and to validate models based on surface data. Mwenifumbo et al. (2004) describe borehole studies at the McArthur River site (Figure 3-9). Laboratory measurements of resistivity, density, P-wave velocity and porosity were also made on Athabasca sandstones and basement rocks to correlate with the in situ measurements (Mwenifumbo et al., 2004). McArthur River boreholes (MAC 197, MAC218 and RL088) intersected the high-grade uranium deposits and the crystalline basement. These boreholes were partially cemented to prevent the leakage of radioactive materials (Mwenifumbo et al., 2004) and consequently there is little deep information available from these boreholes. However, boreholes RL092 and RL103 intersected the basement in regions of low-grade uranium content and were not cemented.

Figures 3-17 and 3-18 show gamma-ray, resistivity, density, velocity and acoustic impedance logs from boreholes MAC218 and, RL088 respectively. The relatively high gamma-ray activity in MFc, MFb and MFa is mostly due to Th and lesser amount of U. There is also a correlation between resistivity, density and the P-wave velocity (Vp) logs due to the change in porosity. As expected, resistivity, density and seismic velocity increase with depth as the porosity decreases (Mwenifumbo et al., 2004).

Logs from MAC218 illustrate a dramatic change in rock properties at a depth of 320 m. At this depth the density, Vp and acoustic impedance (Z) all increase. The reflectivity is around 0.127. Below 400 m, these parameters decrease because there is more fracturing (Mwenifumbo et al., 2004). There are higher resistivities in MFd compared to MFc because there is increase in porosity at the MFc (Mwenifumbo et al., 2004). The alteration zone and the alteration type can be defined by changes in the physical properties.

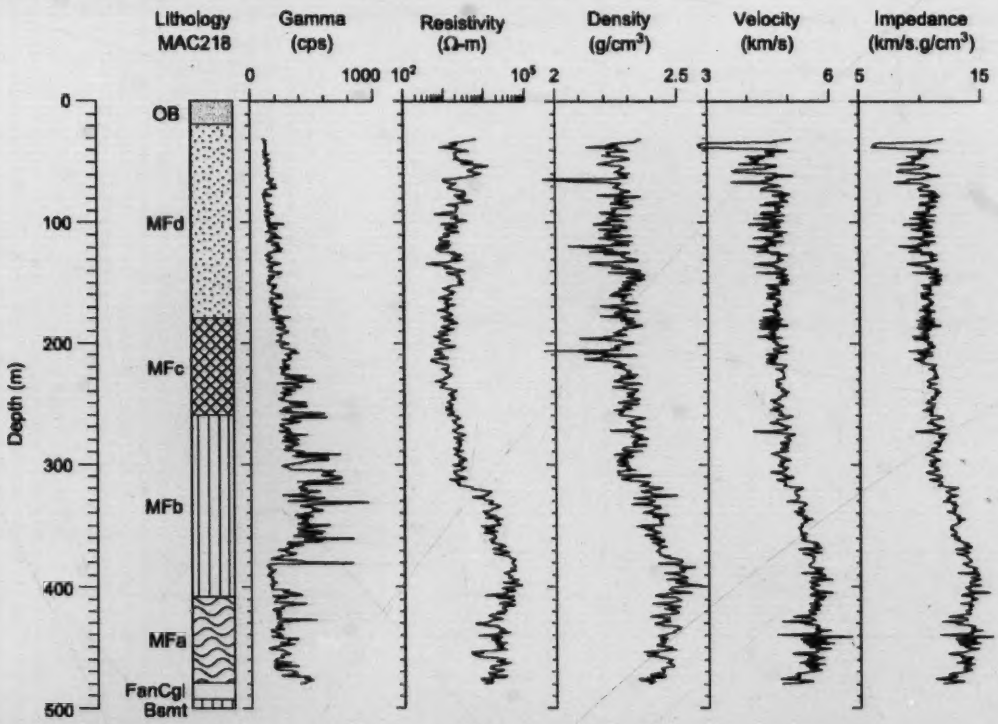

Figure 3-17. Borehole MAC218. OB: Overburden, MFa,b,c,d: Manitou Falls a, b, c, d members, FanCGl: Fan Conglomerate and Bsmt: Basement (Figure is taken from Mwenifumbo et al., 2004). MFa is also known as the Read Formation.

Well logs in MAC197 and RL092 (not shown) are similar to MAC218 (Figure 3-17). Values of resistivity, density and velocity are in accordance. They increase with depth due to a decrease in porosity as a function of silicification (Mwenifumbo et al., 2004). The zone of low Vp between 510 and 560 m correlates with changes in resistivity and is due to fracturing (Mwenifumbo et al., 2004). Resistivity, density and Vp also indicate the silicification increases between 420 m and 500 m depth (Mwenifumbo et al., 2004).

In contrast, RL088 (Figure 3-18) shows slightly different characteristics. The decrease in resistivity, density and Vp values between 190 and 300 m might reflect the increased porosity in the Athabasca sandstone as a result of desilicification in MFd and MFc (Mwenifumbo et al., 2004).

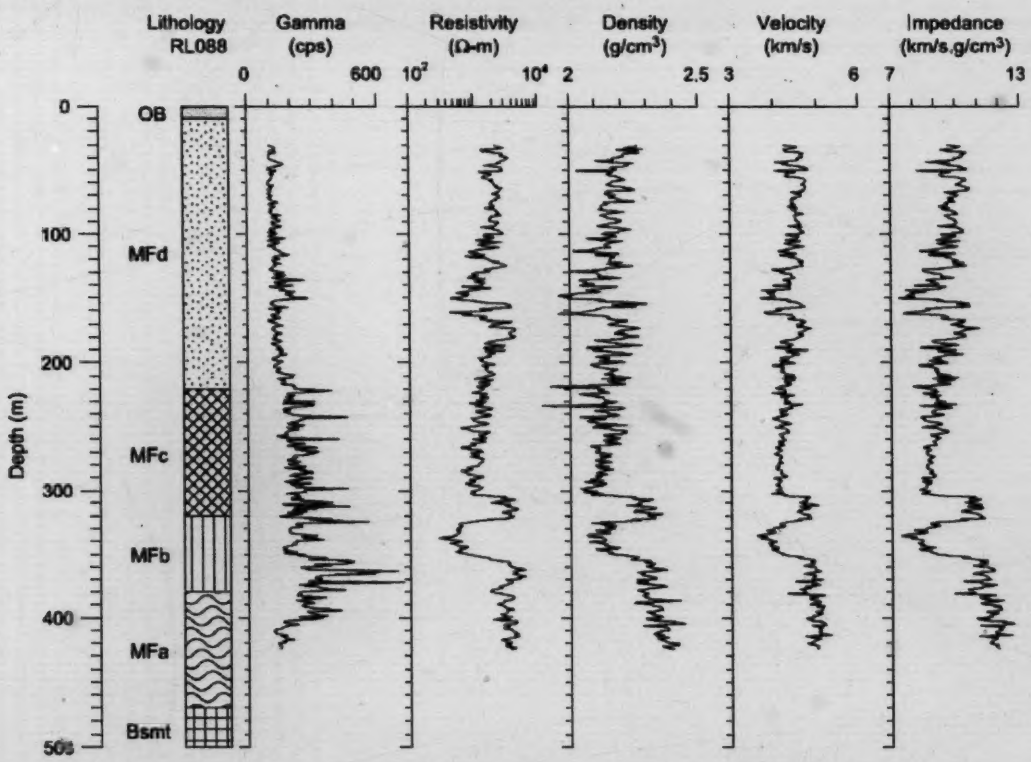

Figure 3-18. Borehole RL088 (Figure is taken from Mwenifumbo et al., 2004).

3.3.5. Electrical and electromagnetic studies at the McArthur River

The regional airborne EM data described in section 3.2.4 showed the presence of major basement conductors in the Athabasca Basin. It has long been known that these basement conductors (graphitic faults) are often associated with unconformity type uranium deposits and are a primary target for exploration. Airborne electromagnetic data in the eastern Athabasca Basin were initially collected in 1977-8 using the Mark VI INPUT time domain system. These data showed high background noise levels and were re-flown in 1981 (McGill et al., 1993). Owing to the large depth to the unconformity in this part of the Athabasca Basin, no basement conductors were detected by these airborne EM surveys at the McArthur River site.

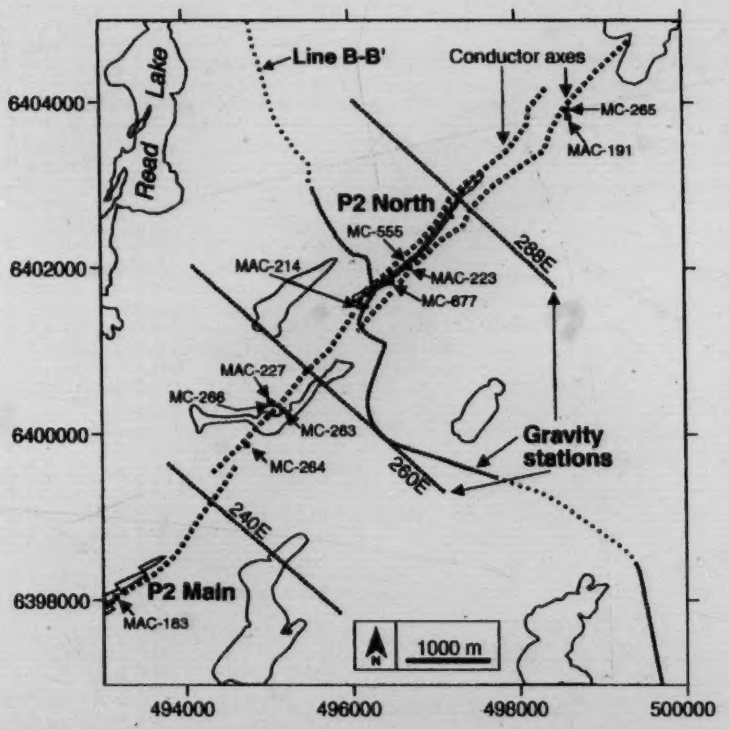

Figure 3-19. Conductor axis as located by time domain EM surveys in the McArthur River area (Figure is taken from Thomas and Wood, 2007).

To image deeper structures, a number of ground EM surveys were implemented. In 1984-5 surveys with the DEEPEM time domain system located the P2 conductor and traced it along strike for more than 13 km (McMullan et al., 1987). This conductor was found to be coincident with a major uranium deposit in 1988 after drilling (Matthews et al., 1997). A Geonics EM37 (time domain) survey was also carried out after the McArthur (P2 North) discovery of 1988 (Matthews et al., 1997). Some 1500 km of Fixed Loop TDEM coverage was completed between 1980 and 1992. All these EM surveys indicated the presence of a strong conductor at 500 m depth (Matthews et al., 1997) with the trend defined in Figure 3-19. The deposit occurs just west of the P2 conductor. Moving Loop data were also collected at the McArthur River site with the UTEM (University of Toronto EM) system. The P2 conductor generates a strong response, which decays slowly and persists at late time indicating a deep and strong conductor. A range of data processing techniques, including thin sheet modelling, suggested that the conductance was around 30 S, with the top of the conductor at a depth of ~ 400 m dipping approximately 75° to the east (Matthews et al., 1997).

Far field frequency domain methods are simpler to interpret than large loop EM methods and several surveys have been implemented at the McArthur River deposit. Their main advantage is that the plane wave makes data analysis simple and depth sounding can be achieved by varying the frequency of the transmitted signal. The VLF method is one of the most widely used, and uses continuously operating radio transmitters. It has the advantage that the survey crew does not need to operate a transmitter, but the high frequency used gives limited depth penetration.

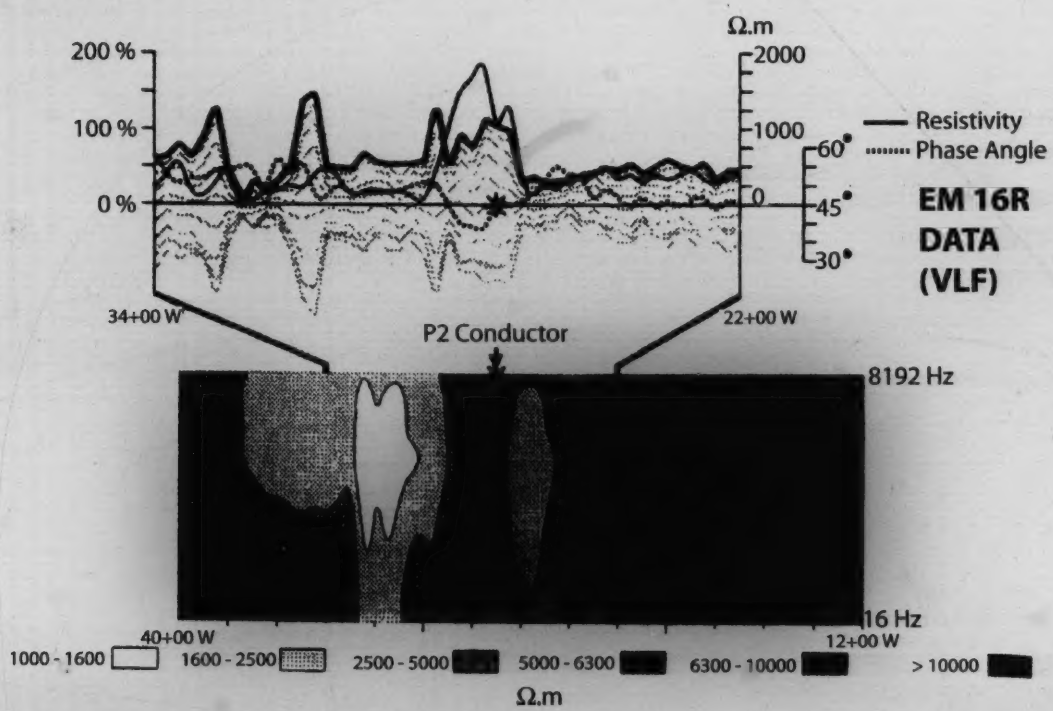

Figure 3-20. Upper panel = VLF data. Lower panel = pseudosection of CSAMT data (Figure is taken from McGill et al., 1993).

The Controlled Source Audio Magnetotellurics (CSAMT) method has potential for deeper exploration compared to VLF because it uses lower frequencies. However, the CSAMT method requires additional field crew for installing and operating a transmitter. Nevertheless, using a CSAMT transmitter is logistically simpler than the large-loop methods. A CSAMT survey was undertaken at the McArthur River above the P2 conductor. The method is very similar to the AMT method (the main focus of this thesis) and shows a resistive feature above the P2 Fault (Figure 3-20). This was interpreted as the intense

silicification (400 m thick) immediately above and to the west of the uranium deposit. However, there is no indication of a basement conductor even at the lowest frequency (16 Hz). Apparent resistivity values are also very high which support the previous statement.

3.4. Summary

In this chapter, geophysical methods used in uranium exploration during the EXTECH-IV project have been reviewed. Radiometry data showed no anomaly at the McArthur River Mine. Gravity data alone suffer from non-uniqueness and is only effective when combined with other geophysical methods. Magnetic data can be effective in identifying the fault and shear zones. However, these zones are quite wide and do not permit direct location of uranium deposits. Seismic exploration gave results that are more promising and were able to image the unconformity and the basement faults. The seismic data may also image the ore deposit directly. However, seismic is an expensive method and the processing is time consuming. 2D seismic exploration may not give reliable images and 3-D surveys may be needed to get reliable results. Electromagnetic methods, which image the graphitic faults associated with the uranium mineralization, are the most promising methods. These methods image the graphitic faults and alteration zones, and have been widely used in uranium exploration elsewhere. However, as uranium exploration moves into the deeper parts in the Athabasca Basin, traditional EM methods become ineffective. Larger loops are required which increases the cost of the exploration. Therefore, the goal of the EXTECH IV project was to develop improved geophysical methods for deep uranium exploration. The audio-magnetotelluric method, which uses the natural sources for subsurface imaging, is one such method and it's application to uranium exploration is described in this thesis.

4. MAGNETOTELLURIC METHOD

It was emphasized in the previous chapter that electromagnetic (EM) methods have played an important role in uranium exploration in the Athabasca Basin. Conventional EM methods have been used to locate graphitic basement faults that are often associated with uranium deposits. However, as uranium exploration moves into deeper parts of the basin, it has been found that existing EM methods cannot image conductors that are present at the depth of the unconformity (often >500 m). This is especially true if conductive overburden is present. In principle, EM methods that utilize large loops could be adapted for deeper investigation, but the logistical effort and cost would be significant. Natural source methods such as magnetotellurics (MT) represent an alternative strategy for deeper exploration. MT records naturally occurring plane EM waves with small receiver dipoles and is thus logistically quite simple. Recent advances in instrumentation allow frequencies up to 10 kHz to be recorded so no transmitter is required for shallow exploration. Tikhonov (1950) gave the first formulation of the magnetotelluric method, which was later expanded by Cagniard (1953). Details of the magnetotelluric method are described by Vozoff (1991) and Simpson and Bahr (2005). MT has been previously used to locate graphitic basement conductors. However previously analyses did not focus on detailed 3-D studies or critical resolution tests. In this thesis, the first modern application of MT to unconformity uranium exploration is described. Before describing the EXTECH-IV AMT survey, the basics of the AMT method are reviewed.

4.1. The Source of Magnetotelluric Signals

The magnetotelluric method uses natural electromagnetic signals to remotely sense the electrical resistivity structure of the subsurface. Since the depth of exploration is inversely related to the square root of the frequency, the MT method can be categorized into three distinct exploration regimes.

1) Long period MT data are used to image depths from 1-1000 km and use signals with frequency below 0.1 Hz. Resolution in the upper 1-2 km is low owing to the long wavelength of these low frequency signals.

2) Broadband MT (0.001 – 500 Hz) is used for crustal scale studies.

3) Audiomagnetotellurics (AMT) uses high frequencies (10000 - 1 Hz) to study shallow structure. This gives good resolution on scales of 10 – 1000 m and is thus most suited to mineral exploration.

At frequencies below 1 Hz, the EM signals used in MT originate in the ionosphere. These variations are caused by fluctuations in the strength and density of the solar wind. At frequencies above 1 Hz, the source is global thunderstorm activity, which propagates worldwide in a waveguide bounded by the conducting earth and ionosphere (Vozoff, 1991). As lightning strikes occur rapidly, AMT signals are generally present over quite a wide frequency band. However, signals can be weak in the so-called AMT dead band around 2 kHz, especially in the daytime.

4.2. Electromagnetic Wave Propagation in a Conductor

EM signals, generated outside the Earth, travel in the air as a wave. The amplitude decreases through geometric spreading but without attenuation. When these signals enter the Earth the non-zero conductivity of the Earth causes strong attenuation and the EM signals travel by diffusion. Their behaviour can be described by Maxwell's equations:

$$\nabla \cdot \mathbf{E} = \frac{\rho}{\varepsilon_0}, \quad \nabla \cdot \mathbf{B} = 0, \quad \nabla \times \mathbf{B} = \mu \mathbf{J} + \mu\varepsilon \frac{\partial \mathbf{E}}{\partial t}, \quad \nabla \times E = -\frac{\partial \mathbf{B}}{\partial t} \qquad (4.1)$$

where **E** is the electric field strength, **B** is the magnetic flux density, **H** is the magnetic field strength, **J** is the electric current density, σ is the electrical conductivity, μ is the magnetic permeability, ε is the permittivity and ρ is the electric charge density. The first of these equations is Coulomb's Law which quantifies how much electric field is generated by free electric charges. The second equation is based on the observation that magnetic field lines must form closed loops and hence magnetic monopoles do not exist. The third equation is an expression of Ampere's Law and quantifies how much magnetic field (**B**) is generated by a specified electric current density (**J**). It also includes the

displacement current term that was introduced by Maxwell. The fourth equation is Faraday's Law and its physical meaning is that a changing magnetic flux generates an electric field. To solve these equations, three constitutive equations must also be defined

$$\mathbf{J}=\sigma\,\mathbf{E}, \qquad \mathbf{B}=\mu\,\mathbf{H}, \qquad \mathbf{D}=\varepsilon\,\mathbf{E}+\mathbf{P} \tag{4.2}$$

where **D** is the displacement or the electric flux density and **P** is the polarization.

In general, σ, μ and ε are constant in time but vary with position in the Earth. For earth materials μ and ε vary little from their free space values and thus can be assumed to be constant. The free space values for μ and ε are $\mu_0=4\pi 10^{-7}$ H/m and $\varepsilon_0=8.85\ 10^{-12}$ F/m.

The third and fourth Maxwell's equations can be coupled to give the following equation for **E**,

$$\nabla\times(\nabla\times\mathbf{E})=-\frac{\partial}{\partial t}\left(\mu\sigma\,\mathbf{E}+\mu\varepsilon\frac{\partial\mathbf{E}}{\partial t}\right) \tag{4.3}$$

If it is assumed that there are no free charges in the subsurface ($\nabla\cdot\mathbf{E}=0$), then this expression can be simplified to

$$\nabla^2\mathbf{E}=\mu\sigma\frac{\partial\mathbf{E}}{\partial t}+\mu\varepsilon\frac{\partial^2\mathbf{E}}{\partial t^2} \tag{4.4}$$

where the first term represents signals that travel by diffusion (conduction current) and the second term represents wave propagation (displacement current). Note, this equation assumes that the charge density (ρ) is zero. To solve equation 4.4 for the context of magnetotellurics, some simplifications must be made. Firstly, it is assumed that the EM fields exhibit a simple harmonic time variation of the form $\mathbf{E}=\mathbf{E}_o e^{-i\omega t}$ where ω is angular frequency. The electric field, **E**, can be written as the product of two functions

$$\mathbf{E}(x,y,z,t)=\mathbf{E}_0(x,y,z)e^{-i\omega t} \tag{4.5}$$

where $\mathbf{E_o}$ does not vary with time. Substitution into equation 4.4 gives

$$\nabla^2\mathbf{E}_o+\omega\mu(i\sigma+\omega\varepsilon)\mathbf{E}_0=0 \tag{4.6}$$

At the low frequencies used in MT, the current flow via conduction is dominant and the displacement term can be ignored. Thus, it is assumed that all EM energy in the Earth travels by diffusion and the spatial variation of the electric field can be written as $\mathbf{E}_0(x,y,z)$ where:

$$\nabla^2 \mathbf{E}_o + i\omega\mu\sigma \mathbf{E}_o = 0 \qquad (4.7)$$

If it is now assumed that the incident wave is planar, polarized in the x-direction and propagating downwards in the z-direction, equation (4.7) can be simplified giving:

$$\frac{\partial^2 E_x^o}{\partial z^2} + i\omega\mu\sigma E_x^0 = 0 \qquad (4.8).$$

To solve this equation a trial solution can be used of the form

$$E_x^o(z) = Ae^{kz} \qquad (4.9)$$

Boundary conditions are applied such that E_x^0 = E_s at z=0 and E_x^0 is bounded as z approaches infinity. It can be shown that the solution has the form:

$$E_x^0(z) = E_x^0(z)e^{-z/\delta}e^{iz/\delta} \qquad (4.10)$$

where δ is called the skin depth (in metres) and defined as

$$\delta = \sqrt{\frac{2}{\omega\mu\sigma}} = \sqrt{\frac{T\rho}{\pi\mu}} = 503.29\sqrt{\frac{\rho}{f}} \qquad (4.11)$$

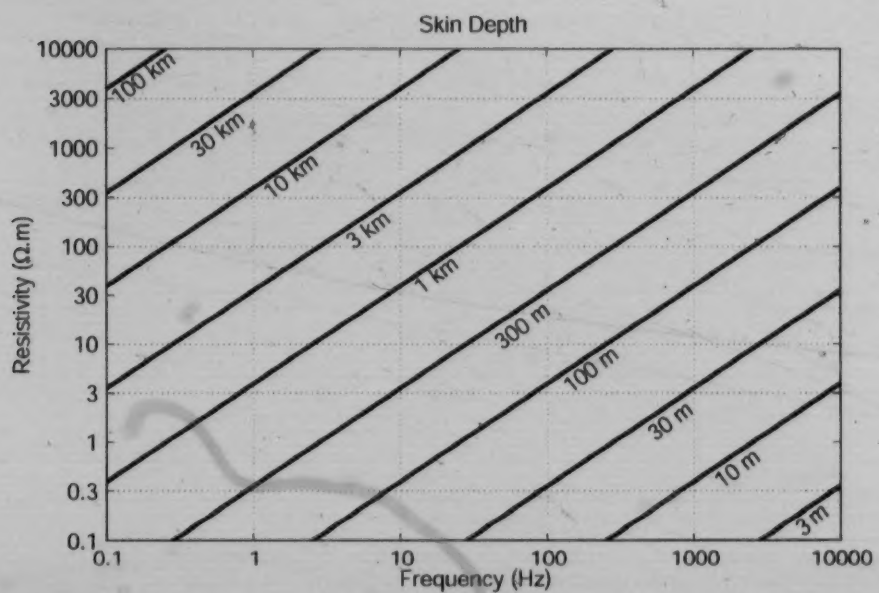

Figure 4-1. Illustration of the skin depth (depth of penetration), which shows the relationship between the AMT frequencies and the resistivity of the medium of the survey area.

Skin depth is defined as the depth at which the initial amplitude of the electromagnetic wave decays to 1/e of the surface value. In other words, it is the

depth at which the initial electric field amplitude has decayed to ~37 % of the value at the surface. Figure 4-1 illustrates the relationship between the resistivity of the earth, the frequency of the EM wave and the skin depth. Higher frequencies have short skin depths and do not penetrate to great depths. In contrast, low frequencies can penetrate deeper. The resistivity of the Earth also controls the penetration depth since EM waves will travel deeper in a more resistive medium. Figure 4-2 also demonstrates this phenomenon, showing that higher frequencies terminate at shallow depths while lower frequencies propagate to greater depths.

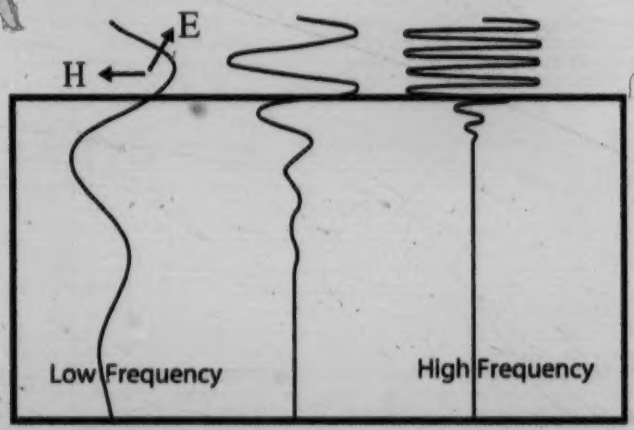

Figure 4-2. Physics of electromagnetic waves in a halfspace (Figure is modified from http://www-geo.phys.ualberta.ca/~unsworth/MT/MT.html). High frequencies penetrate to the shallow depths where low frequencies penetrate to the deeper parts of the earth.

4.3. Interaction of EM Signals with a Uniform Earth

It can be shown that when an incident EM signal strikes the Earth's surface, most of the energy is reflected back into the air (Simpson and Bahr, 2005). Only a small fraction travels into the Earth. It can also be shown that the ratio of horizontal electric and magnetic fields contains information about the electrical resistivity of the subsurface. This ratio is termed the impedance and it is a function of frequency

$$Z_{xy}(\omega) = \frac{E_x(\omega)}{H_y(\omega)} \tag{4.12}$$

for a halfspace, it can be shown that,

$$Z_{xy}(\omega) = \frac{-i\omega\mu}{k_1} \qquad (4.13).$$

Since $k_1 = \sqrt{-i\omega\mu\sigma}$, it follows that

$$Z_{xy}(\omega) = (1-i)\sqrt{\left(\frac{\mu\omega}{2\sigma}\right)} \qquad (4.14).$$

The apparent resistivity can then be expressed as:

$$\rho_a(\omega) = \frac{1}{\omega\mu}\left|\frac{E_x(\omega)}{H_y(\omega)}\right|^2 \qquad (4.15).$$

The apparent resistivity in Equation (4.15) represents an average resistivity of the Earth from the surface to a depth equal to a skin depth. Another important parameter of the MT method is the phase which can be defined as the argument (Φ) of the impedance $Z_{xy}(\omega)$ (Figure 4-3)

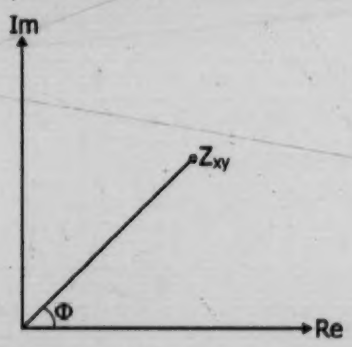

Figure 4-3. The definition of phase in an Argand diagram.

$$\arg(Z_{xy}) = \frac{\mathrm{Im}(Z_{xy})}{\mathrm{Re}(Z_{xy})} \qquad (4.16),$$

It is simple to show that:

$$\Phi = \tan^{-1}(-1) = \frac{\pi}{4} \Rightarrow 45^\circ \qquad (4.17).$$

When an electromagnetic wave propagates in the air, there is no phase difference between the electric and the magnetic fields of the Earth. However, it is 45° in a homogeneous, conductive Earth (Eq. 4-17). Therefore, if the Earth has a uniform resistivity, the apparent resistivity and phase would be constant at all frequencies. In contrast, if the Earth has a more complex geoelectrical structure then both the apparent resistivity and the phase will vary with frequency. A

comparison of homogeneous and two layer earth model AMT responses is presented in Figure 4-4.

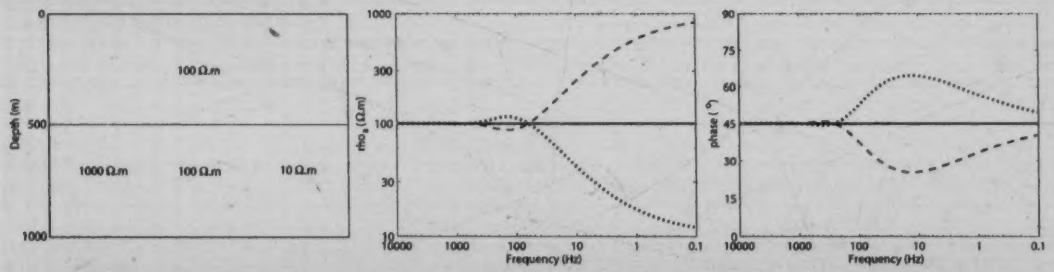

Figure 4-4. The subsurface electrical model (left panel) and associated resistivity (middle panel) and phase (right panel) curves. The solid line represents the homogeneous half-space model. The dashed curve represents a model in which the second layer is more resistive. The dotted curve represents a model in which the second layer is less resistive.

Note that the magnetotelluric phase is sensitive to changes in resistivity with depth (Figure 4-4). When the resistivity increases with depth, the phase is below 45°. In contrast, a decreasing resistivity with increasing depth results in phase values greater than 45°. Note that the wave number in the ground (k_1) is much larger than the wave number in the air ($k_1 >> k_0$). If Snell's Law is applied, then it will be seen that the transmitted angle θ_t does not depend strongly on the incident angle θ_i. Therefore, the direction of approach of the electromagnetic wave does not matter, since all incident electromagnetic signals will propagate vertically in the Earth (Figure 4-5).

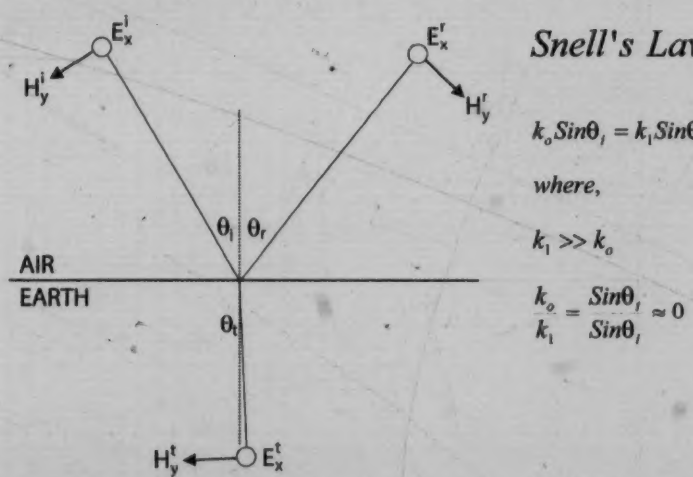

Figure 4-5. Propagation of EM signals with Snell's Law (Unsworth, 2003 Geoph424 lecture notes).

4.4. MT Impedance over a Two Dimensional Earth

In the one-dimensional case, the same value will be obtained for $Z_{xy}(\omega)$ and $Z_{yx}(\omega)$, regardless of the orientation of the measured electric and magnetic fields provided they are orthogonal. However over a 2D Earth the value of $Z_{xy}(\omega)$ and $Z_{yx}(\omega)$ will vary as the azimuth of *x*-axis changes. Mathematically this can be expressed by writing the impedance as a 2 x 2 tensor.

$$\begin{pmatrix} E_x(\omega) \\ E_y(\omega) \end{pmatrix} = \begin{pmatrix} 0 & Z_{xy}(\omega) \\ Z_{yx}(\omega) & 0 \end{pmatrix} \begin{pmatrix} H_x(\omega) \\ H_y(\omega) \end{pmatrix} \tag{4.18}$$

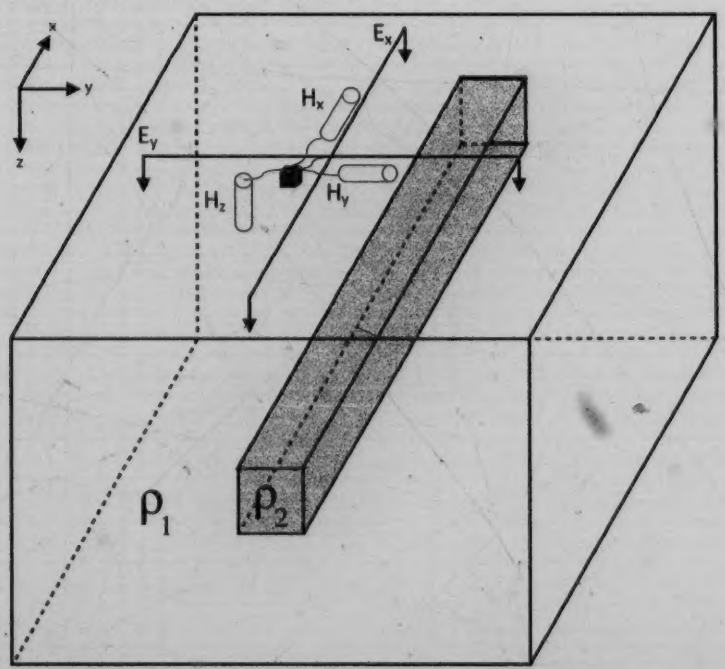

Figure 4-6. Configuration of MT in the field above the prism model ($\rho_2<\rho_1$).

Figure 4-6 shows the basic configuration for measuring MT data in the field. E_x and E_y are the dipoles which measure the electric field and H_x, H_y and H_z are magnetic field components measured by induction coils in AMT. Since there are two main components of the impedance, different apparent resistivity formulae can be derived such as:

$$\left.\begin{aligned} \rho_{xy}(\omega) &= \frac{1}{\omega\mu}\left|Z_{xy}(\omega)\right|^2 \\ \rho_{yx}(\omega) &= \frac{1}{\omega\mu}\left|Z_{yx}(\omega)\right|^2 \end{aligned}\right\} \tag{4.19}$$

Consider a 2D earth where the geological strike is parallel to the *x*-axis. The subsurface resistivity varies only in the *y* and *z*-directions and all structures are assumed to extend to $x=\pm\infty$. In contrast to the 1D case, it is now possible that the vertical EM field components are non-zero. For a 2D prism model, if the background halfspace resistivity ρ_1 is 100 Ω.m and the prism resistivity ρ_2 is 1 Ω.m, then the electric current will preferentially flow along the conductive prism (Figure 4-6).

It can be shown that in a 2-D Earth Maxwell's equations can be separated into two independent subsets.

SET 1: E_x, H_y and H_z

$$\frac{\partial H_z}{\partial y} - \frac{\partial H_y}{\partial z} = \mu\varepsilon\, E_x; \quad \frac{\partial E_x}{\partial z} = -i\omega\, H_y; \quad \frac{\partial E_x}{\partial y} = -i\omega\, H_z \qquad (4.20).$$

This subset of field components has an electric field polarized parallel to the strike direction. The magnetic field components are confined to the *y*-*z* plane. This is called the Transverse Electric (TE) mode or E-polarization (Figure 4-7).

SET 2: H_x, E_y and E_z

$$\frac{\partial E_z}{\partial y} - \frac{\partial E_y}{\partial z} = \mu\varepsilon\, H_x; \quad \frac{\partial H_x}{\partial z} = -i\omega\, E_y; \quad \frac{\partial H_x}{\partial y} = -i\omega\, E_z \qquad (4.21).$$

These components have a magnetic field polarized parallel to the strike direction. The electric field components are confined to the *y*-*z* plane. This is called the Transverse Magnetic (TM) mode or B-polarization (Figure 4-7).

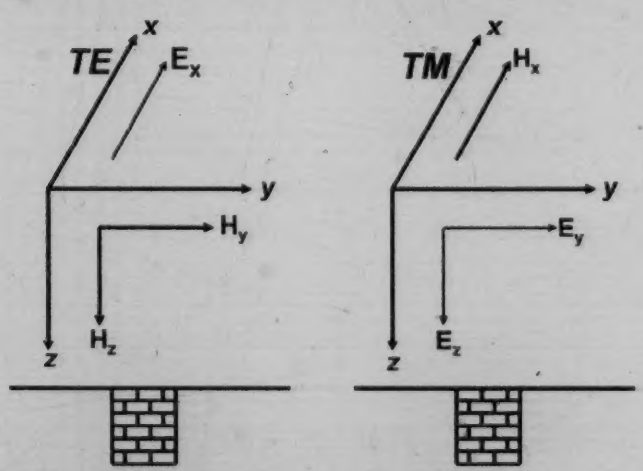

Figure 4-7. TE and TM modes in magnetotellurics.

Thus different values of impedance will be computed if the instrument is rotated through 90° and these are called Z_{xy} and Z_{yx}. In field practice, both Z_{xy} and Z_{yx} are measured simultaneously. The *xy* component is computed from the electric field parallel to strike and the magnetic field orthogonal to strike (TE mode). The *yx* component is computed from the magnetic field parallel and electric field orthogonal to strike (TM-mode) (Figure 4-7).

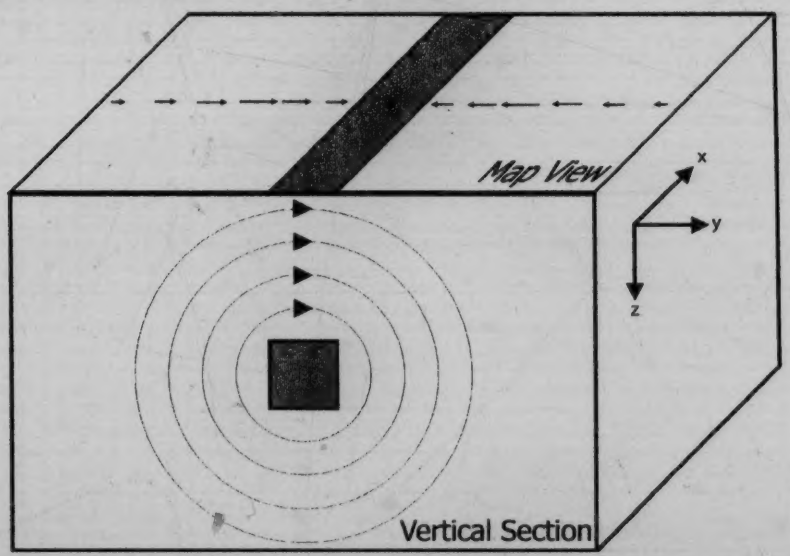

Figure 4.8. Behaviour of the vertical magnetic field over a 2D earth. Induction vectors point towards a conductor as in the convention of Parkinson (1962).

In a 2D earth, the TE mode generates non-zero vertical magnetic fields. Consider the case of a conductive body oriented in the x-direction (Figure 4-8). The current in the conductive body will flow in and out of the plane of the diagram. At the instant shown in the figure, the magnetic field is up on the left of the conductor and down on the right. This field behaviour can be used to image subsurface structures. Induction vectors are computed using the ratio of the vertical to the horizontal magnetic field components. The vertical magnetic field equation is given as

$$\mathbf{H}_z = \begin{pmatrix} T_x & T_y \end{pmatrix} \begin{pmatrix} \mathbf{H}_x \\ \mathbf{H}_y \end{pmatrix} \tag{4.23}$$

where T is called the tipper and has both real and imaginary parts,

$$\left.\begin{aligned} T_x &= \mathrm{Re}(T_x) + \mathrm{Im}(T_x) \\ T_y &= \mathrm{Re}(T_y) + \mathrm{Im}(T_y) \end{aligned}\right\} \tag{4.24}.$$

The real and imaginary parts of the induction vectors in Wiese convention (1962) are given as

$$\left.\begin{aligned} IV^{\mathrm{Re}} &= \mathrm{Re}(T_x)\mathbf{E}_x + \mathrm{Re}(T_y)\mathbf{E}_y \\ IV^{\mathrm{Im}} &= \mathrm{Im}(T_x)\mathbf{E}_x + \mathrm{Im}(T_y)\mathbf{E}_y \end{aligned}\right\} \qquad (4.25)$$

The Parkinson convention (Parkinson, 1962) places a minus sign in front of the terms with T_x in equation 4.25. This forces the induction arrows to point towards a conductor (Figure 4-8). In contrast, induction arrows point away from the conductor in Wiese convention. In this thesis, the Parkinson convention is used throughout. The magnitude of the arrows is also important in terms of defining the location of the conductor. If the conductor is close to the location of the MT station, the magnitude of the induction vector will be small. As measurements are made further away from the conductor, the arrows will initially increase in length (Figure 4-8). Eventually, at large distance the induction vectors will again diminish as the response of the conductor tends to zero.

4.5. Time Series Analysis in MT

During an AMT/MT survey, the time variations of electric and magnetic fields are recorded as a function of time. Figure 4-9 shows a sample time series due to a lightning strike in Central California. The analysis in the previous section was in the frequency domain, so it is simplest to convert the measured data into the frequency domain. Methods that can be used to give statistically robust estimates of the impedance tensor are described by Egbert and Booker (1986; 1989; 1993) and Egbert (1989; 1997; 2002).

In recent decades, two major advances have improved the quality of MT impedances obtained from field data. The first has been the remote reference technique (Goubau et al., 1979; Gamble et al., 1979; Clarke et al., 1983). In this technique, MT data are recorded simultaneously at two different sites and the remote reference processing can be shown to remove noise that is incoherent between the two locations. However, correlated noise cannot be removed with this method. Typical sources of noise include 1) ground motion, 2) power lines, 3) electric trains, 4) cathodically protected pipelines, 5) water pumps, 6) electric fences, 7) vehicles and trains, 8) animal disturbance and 9) water flowing over electrodes. The distance required between the survey area and the remote

reference varies depending on the type of noise. For example, 500 m is enough to eliminate magnetic noise caused by ground motion while 500 km may be needed to remove noise originating in direct current (DC) electric trains. The second important development in MT signal processing has been the application of statistically robust techniques for estimating the impedance tensor (Egbert and Booker, 1986; 1989; 1993 and Egbert, 1989; 1997; 2002).These methods are used to average multiple estimates of the impedance which are derived from different parts of a long time series recording. Least-squares estimates are not generally successful, so the robust methods are used to recognize outliers and reduce their effects by down-weighting in the averaging process.

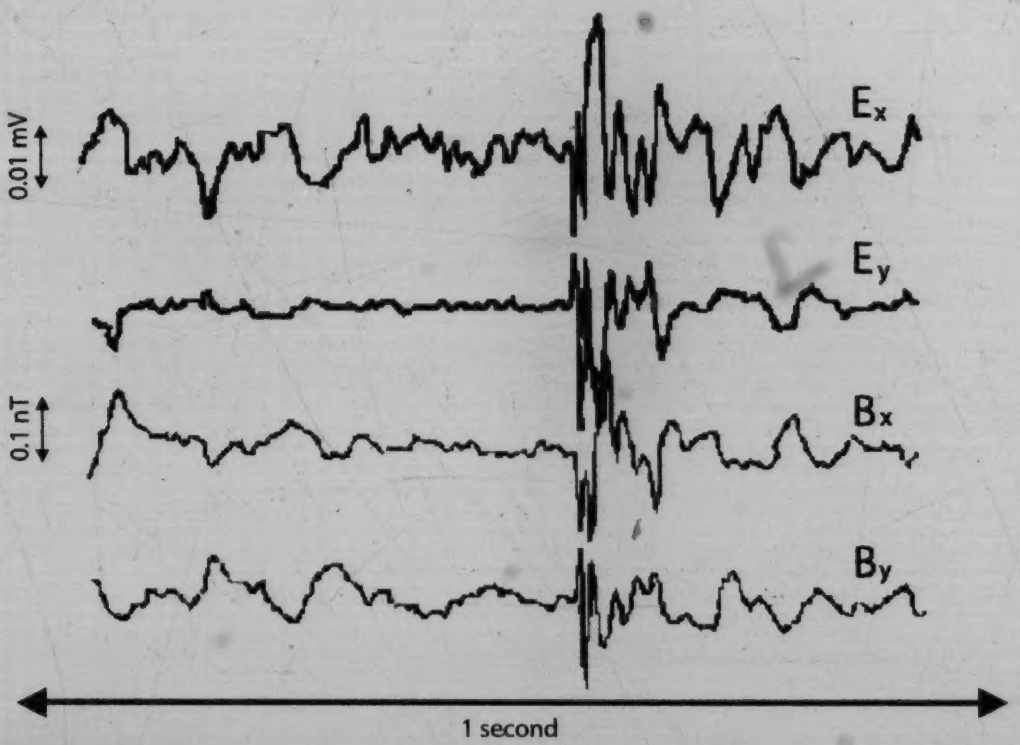

Figure 4-9. A sample time series at the AMT frequencies due to a distant lightning strike recorded in Central California (modified from http://www-geo.phys.ualberta.ca/~unsworth/MT/time_series_lightning.gif).

4.6. Applications of AMT Method

Broadband MT exploration has been used in many applications. This has included tectonic, geothermal, environmental, geotechnical and mineral exploration (Vozoff, 1991). In previous years the naturally occurring high

frequencies needed for shallow exploration could not be recorded because of noise in the magnetic sensors, and a transmitter was used to generate them in the CSAMT technique. However, improved magnetic sensors now allow natural signals to be recorded in the 10000-1 Hz frequency band. Thus, a transmitter is not needed and AMT can be used in applications that previously required the additional signal from the CSAMT transmitter.

AMT has been used in groundwater applications where the groundwater table is too deep for time-domain EM methods. Ritz et al. (1997) described a groundwater study in a coastal area of Reunion. They located three layers in their study 1) a resistive cover (100- 300 m thick) consisting of dry volcanic flows, 2) Basaltic layer saturated with fresh water and 3) basaltic layer saturated with salt water (seawater).

There are many examples of the application of the AMT method to mineral exploration. Lakanen (1986) described one of the first applications of the AMT method to mineral exploration in a base-metal survey in Finland. However, this study was limited by the cumbersome instrumentation that was used in those years and very limited analysis algorithms. Jones and McNeice (2002) used modelling studies to investigate the sensitivities of AMT data to steeply dipping targets. They suggested that the TM mode data might not be useful for target detection or delineation; while the TE mode and vertical field transfer function could reveal steeply dipping targets. They further suggested using the combination of these components of the data. Jones and Garcia (2003) described the application of AMT data to base-metal exploration at Okak Bay, Labrador, Canada. Okak Bay is a small inlet located just north of the very large Ni-Cu-Co Voisey's Bay deposit. They showed that the AMT data could detect massive sulphides and the 2D modelling of 3D bodies was valid and could be made more useful with well log (resistivity) information from a single hole. This approach allowed a thin mineralization zone to be detected at depth of ~500 m, where Transient EM (TEM) method suggested 100 – 200 m depth.

Leppin and Goldak (2005) described the application of AMT exploration data to an unconformity type uranium deposit at Virgin River in the Athabasca Basin, Alberta. They imaged deep basement conductors and associated alteration halos. At Wide Lake, they imaged a 700 m deep 450 m thick zone of altered sandstones. They also imaged a 5 km wide illitic lower sandstone at Stewardson Lake at a depth of 600 to 1000 m. Furthermore, they observed a 3

km wide anomaly below 1150 m depth that was interpreted as two parallel basement conductors.

Queralt et al. (2007) also used the AMT method to study the geometry of a massive sulphide body at Bathurst, New Brunswick, Canada and performed both 2D inversions and 3D modelling. They found that at high frequencies, 2D modelling was valid. However at low frequencies only the TM mode could be interpreted in a 2D fashion. Thus, they concluded that 2D inversion could resolve the top of the 3D body but not the base.

In this thesis AMT data are applied to the unconformity type uranium exploration at McArthur River. The data analysis, 2D and 3D inversion and modelling studies, and interpretation are described in the following chapters.

5. EXTECH IV AUDIO-MAGNETOTELLURIC DATA COLLECTION AT THE McARTHUR RIVER MINE

As has been shown in previous chapters, the location of basement conductors is an important part of geophysical exploration for unconformity uranium in regions such as the Athabasca Basin and Thelon Basins in Canada and in the Kombolgie Basin in Australia (Jefferson et al., 2007). As exploration moves to greater depths in these basins, existing electromagnetic (EM) methods are not capable of adequately mapping deep basement conductors. Existing ground EM methods such as UTEM and DEEPEM, and airborne EM methods such as MEGATEM and VTEM have a maximum depth of penetration of 800-1000 metres in ideal conditions. Overburden in these regions can limit this penetration depth and alternative EM methods are needed for deep exploration.

As was described in the previous chapter, the AMT method has recently developed into a useful exploration tool that has a number of advantages over other EM methods. The quieter magnetic sensors that are now available remove the need to use a transmitter in the 1-10000 Hz frequency band. The logistics are simplified by small receiver dipoles and the fact that no large transmitter loops are needed. This allows the collection of large datasets capable of constraining resistivity structures in 3-D. The plane wave EM fields simplify the data interpretation. Finally, the skin depth phenomenon allows penetration depth to be increased by simply recording lower frequencies that are naturally present.

To investigate how useful AMT data could be in the context of unconformity uranium exploration, a test survey was commissioned as part of the EXTECH-IV project (EXploration Science and TECHnology Initiative). EXTECH I and II were initiated for massive sulphide research in the Rusty Lake – Snow Lake Greenstone Belts in Manitoba and Bathurst Mining Camp in New Brunswick respectively. EXTECH III was initiated for gold research in Yellowknife in Northwest Territories. EXTECH IV was a project supported by the Canadian government, a number of uranium mining companies and academic researchers.

The goal of the project was to enhance the state of knowledge about the Athabasca Basin uranium deposits in Alberta and Saskatchewan. The project was mostly focussed on the McArthur River deposit, since this was one of the largest and best characterized unconformity uranium deposits in the Athabasca Basin. By studying a well understood deposit, new geophysical results could be verified with extensive subsurface data such as well logs.

5.1. EXTECH-IV AMT Data Acquisition

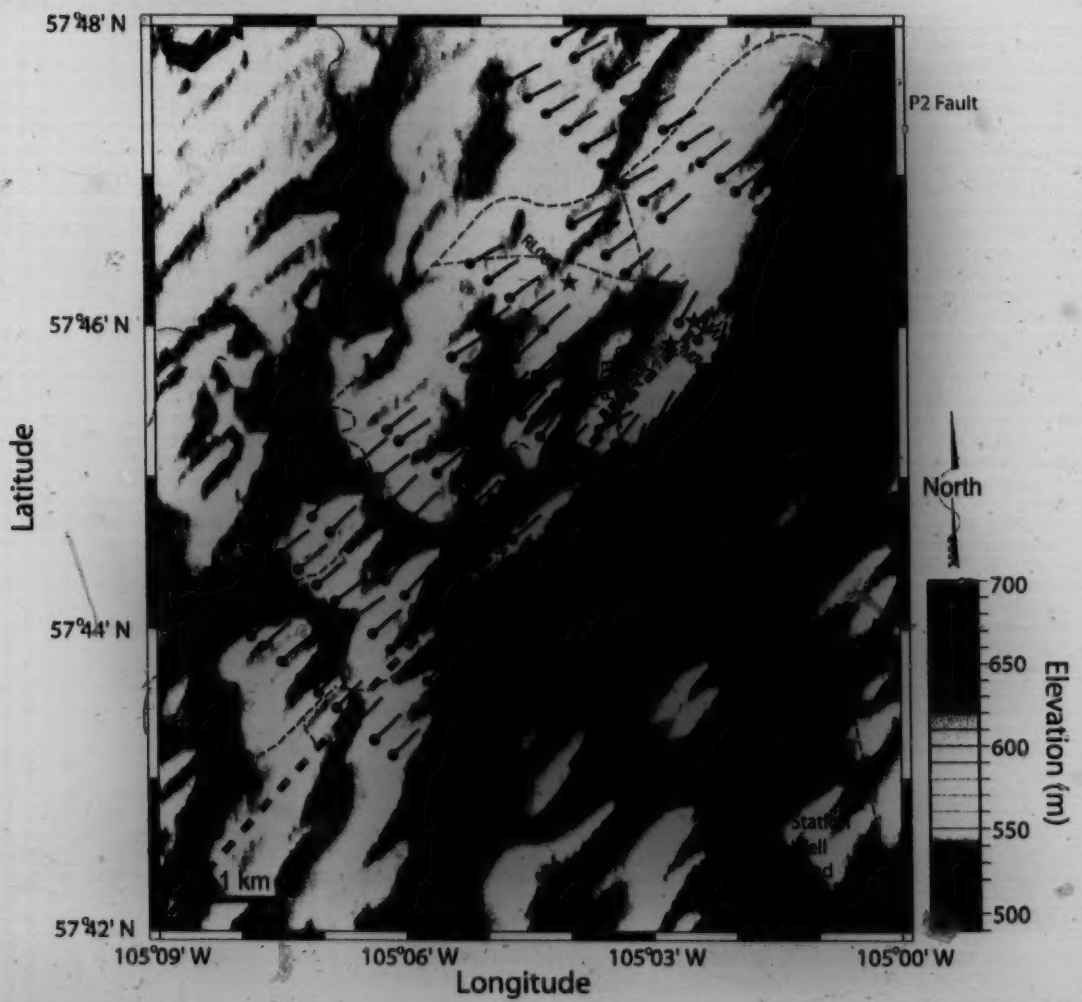

Figure 5-1. Station locations of the EXTECH-IV AMT data set at the McArthur River mine. Blue diamond signs indicate the uranium pod locations. The black lines show strike directions derived by tensor decomposition for real data over a frequency range 1000 – 1 Hz. Northeast - southwest striking topography features are due to the glacial flow. Dashed red line shows the direction of the P2 Fault.

Geosystem SRL recorded AMT data in 2001 and 2002 at the McArthur River mine (Craven et al., 2007). The 2002 AMT data set consisted of 132 stations on 11 parallel profiles that crossed the P2 fault at right angles (Figure 5-1). Data collection used Metronix AMT systems, and the magnetic fields were measured with BF-6 and BF-10 induction coils produced by Electro-Magnetic Instruments (Craven et al., 2007). The distance between profiles was approximately 800 metres, and the station spacing was approximately 300 metres (Figure 5-1). AMT data coverage in the survey area was designed to allow a fully 3D analysis. The time series data were recorded with sampling rates of 40960, 4096 and 256 Hz, and electric field dipoles were approximately 50 m in length (Craven et al., 2007). Usable AMT data were obtained over the frequency range 10200 – 3 Hz (Craven et al., 2007). Coherent time series segments from each sampling rate were selected automatically for robust analysis to reduce the effects of bias because of electromagnetic noise. An iterative re-weighting scheme was used to provide a robust estimate of the apparent resistivities and phases (Larsen et al., 1996).

5.2. Dimensionality and Strike Analysis

As described in the previous chapter it is essential to understand the dimensionality of an AMT dataset before attempting forward modelling or inversion. This can determine if a 2-D approach will be valid, which can save the effort and cost of a full 3-D AMT data analysis. In the case that a 2-D analysis is valid, dimensionality calculations can determine the best fitting geoelectric strike direction. Note that there is a 90° ambiguity in the strike direction and geological information is needed to choose the correct direction. The profiles at the McArthur River mine were designed to be orthogonal to the anticipated strike direction i.e. parallel to the P2 fault. In this study, the role of dimensionality computations was to confirm that the geoelectric strike was parallel to the well characterized geological strike.

Early methods of computing geoelectric strike simply rotated the data mathematically until the sum of diagonal components of the impedance tensor Z_{xx} and Z_{yy} was minimized (Swift, 1967). However, a more general approach called tensor decomposition is now widely used. This is preferred to rotation because it recognizes that AMT data are often distorted by small scale resistivity structures at the surface. This distortion can change both the direction and the

magnitude of the electric fields. One of the first widely used decomposition algorithms was developed by Groom and Bailey (1989). In this study a refined version of the Groom-Bailey algorithm was used that can analyse multiple stations (McNeice and Jones, 2001). This tensor decomposition was applied to the AMT data in the frequency range of 1000 – 1 Hz. The geoelectric strike direction is shown in a rose diagram in Figure 5-2. A well-defined geoelectric strike direction (45°) can be observed, and this is parallel to the P2 fault direction as expected. The geoelectric strike direction can also be presented in map format (Figure 5-1). A current channelling angle is also shown in Figure 5-2. Current channelling describes the process where subsurface structure concentrates electric currents, primarily through galvanic effects (Lezaeta and Haak, 2003). The channelling direction represents a combination of the regional (2D) geoelectric strike and the local (3D) distortion. Therefore, if distortion is strong it is possible to have different angles for the geoelectric strike and current channelling. The angles for geoelectric strike and current channelling are similar in Figure 5-2, confirming that at McArthur River the distortion is relatively weak.

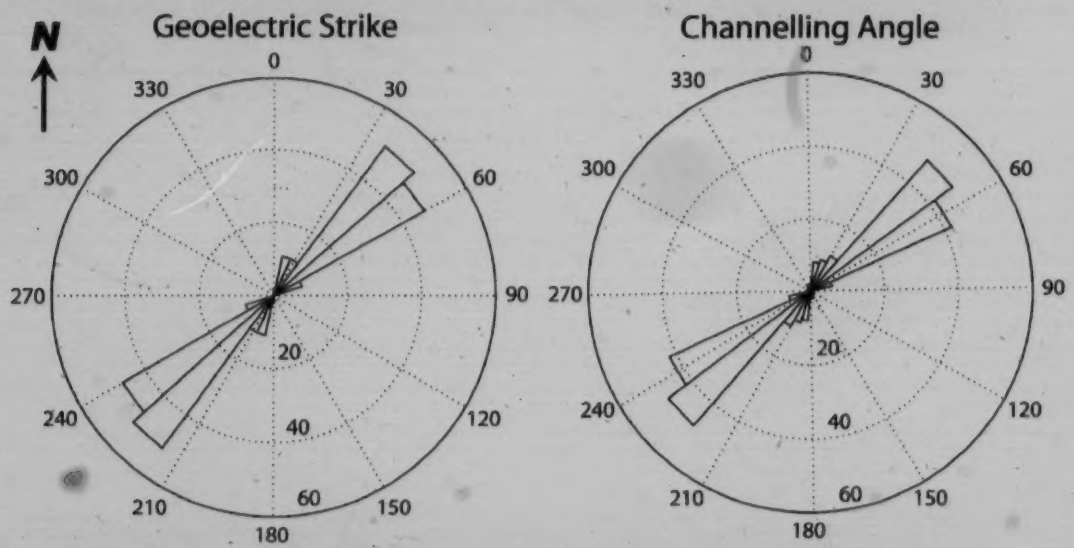

Figure 5-2. Rose diagrams of geoelectric strike and channelling angle computed with the algorithm of McNeice and Jones, (2001).

Tensor decomposition makes a number of assumptions that must be valid if the results are to be considered reliable. This includes 1) the assumption that the undistorted impedance data are regionally 2D and 2) that the magnetic fields have not been distorted (McNeice and Jones, 2001). The degree to which these

assumptions are valid can be assessed by considering the root-mean-square (r.m.s.) misfit that is computed by the algorithm. The values shown in Figure 5-3 are generally low indicating that the application of the tensor decomposition is valid. The exceptions occur at two locations with high r.m.s. misfit values. One area is in the northeast corner of the survey area and the other close to the mine site.

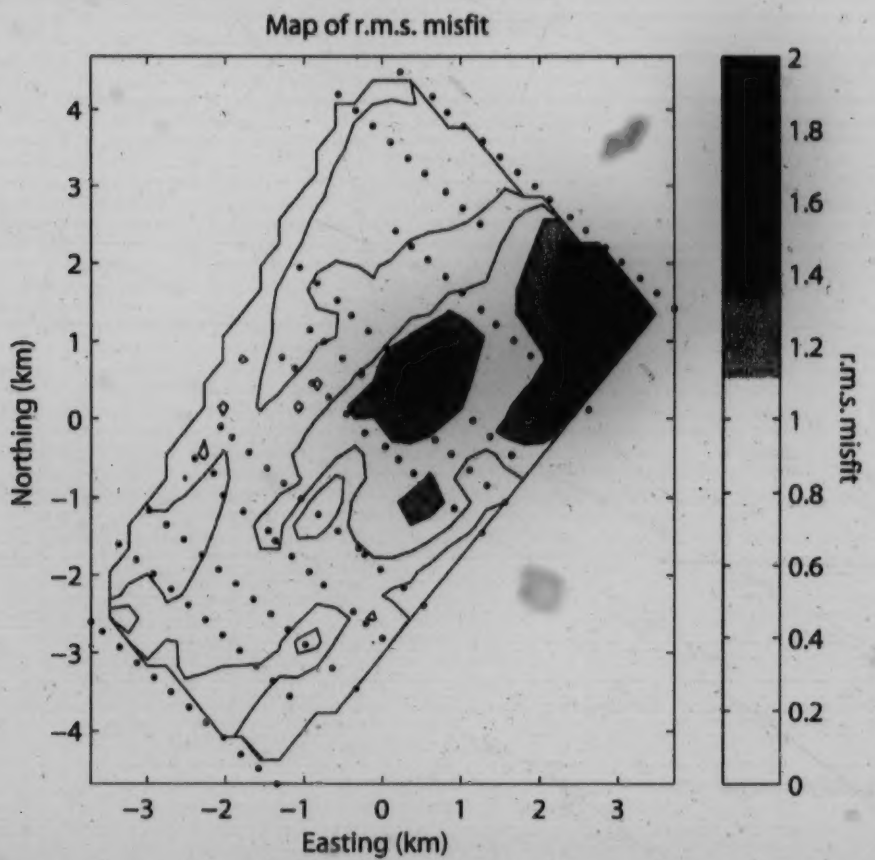

Figure 5-3. The contour map of the r.m.s. misfit values obtained from the tensor decomposition code mostly shows values below the acceptable value of 1.5.

Figure 5-4 shows the parameters that characterize the galvanic distortion, the so-called twist and shear angles. The possible maximum and minimum values for the shear angle are -45° and 45°, and for the twist angle are -60° and 60° respectively (McNeice and Jones, 2001; Jones and Garcia, 2003). If the shear or twist angle is close these limits, then this indicates the electric fields are linearly polarized and orthogonal (regional) components of the electric field cannot be reconstructed. Values of twist and shear angle at McArthur River

range between -20° and 20° indicating that strong distortion is not present. Combined with the low r.m.s. misfit values, these observations show that a 2D approach is reasonable for this dataset. All data were then rotated to a coordinate system with the *x*-axis in the N45°E direction.

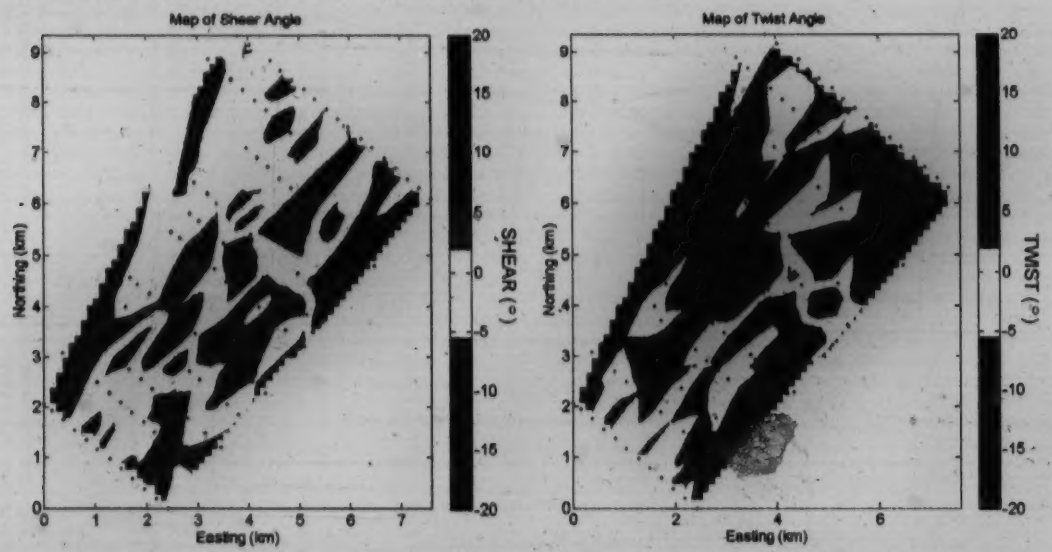

Figure 5-4. Contour map of the shear and twist angles at the McArthur River area derived from tensor decomposition with the McNeice and Jones (2001) algorithm. These values are not close to the maximum possible values, which suggest that the distortion is not strong in this area.

5.3. Vertical Magnetic Field and Induction Vectors

Over a 1-D layered Earth, no vertical magnetic field is generated by electromagnetic induction. However, if the subsurface is 2-D or 3-D then vertical magnetic fields can be generated, and they can be displayed as induction vectors (see Chapter 4). These vectors can also give additional information about the dimensionality of the AMT data set. Figure 5-5 shows the real induction vectors at a frequency of 100 Hz. Simple skin depth arguments show that this frequency samples the subsurface to a depth of approximately 2 km. Induction vectors parallel to the profile are an indication of a 2D resistivity structure and are observed on lines 224 – 248. Vectors on most profiles show a reversal, marking the location of a conductor. The situation is more complex to the north, and the induction vectors are oriented at a significant angle to the profile direction. Note that induction vectors show more evidence of 3D behaviour than the tensor

decomposition. The reason is that AMT impedances are primarily sensitive to structures below the station, whereas vertical magnetic fields (induction vectors) are most sensitive to structures located to the side of the station (Tuncer et al., 2006a). The reason for this behaviour will be further investigated by modelling studies in the following chapters.

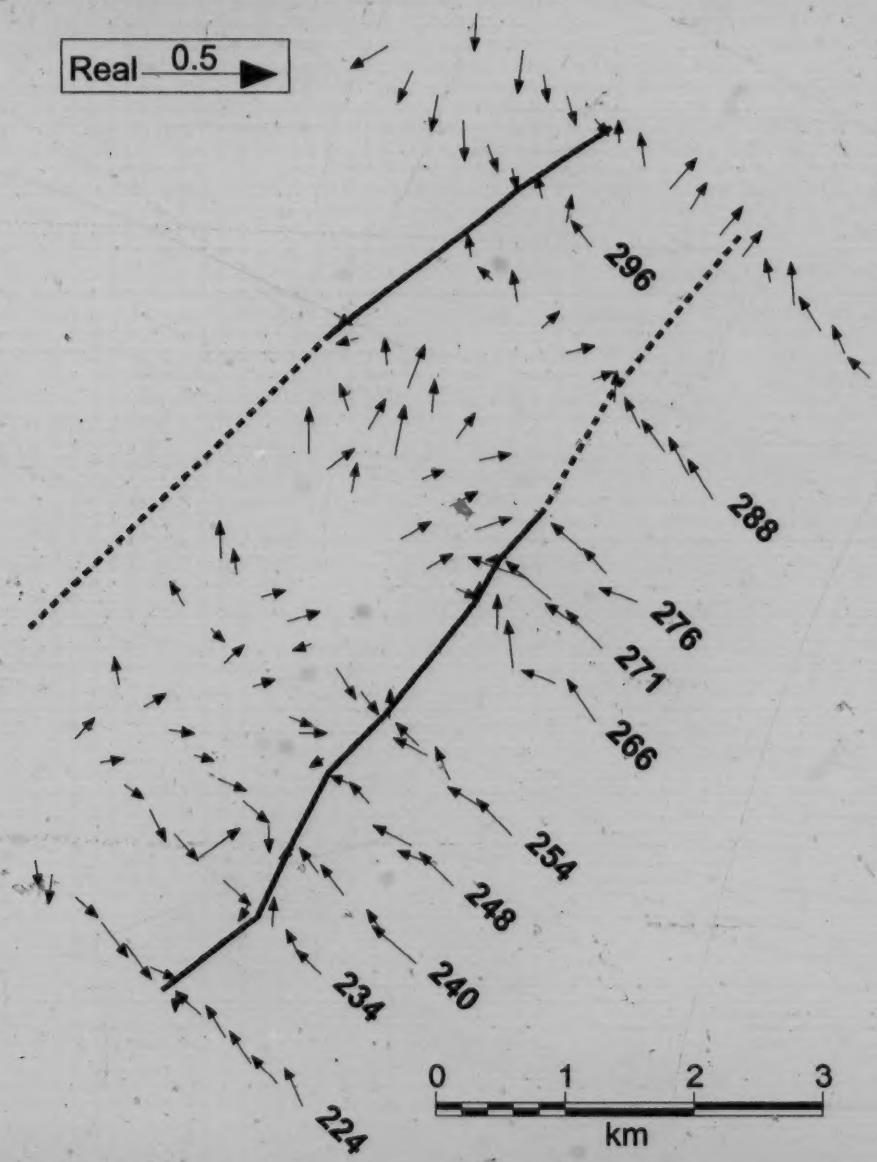

Figure 5-5. Real induction vectors at 100 Hz frequency in the Parkinson (1959) convention. Note that the induction vectors point at a conductor in this convention. Solid red line shows the conductor, dashed red line shows the possible extension of the conductor.

5.4. Apparent Resistivity and Phase Curves

Having shown that a 2-D analysis is justified, and a strike direction is well defined, the TE and TM modes can be defined. The TE mode comprises electric current flowing parallel to geoelectric strike (N45°E) while the TM mode comprises electric currents flowing across strike (N135°E). Typical curves are shown in Figure 5-6. The figure illustrates that the AMT data are of good quality, except for the AMT dead band where the signal is weak around 2 kHz.

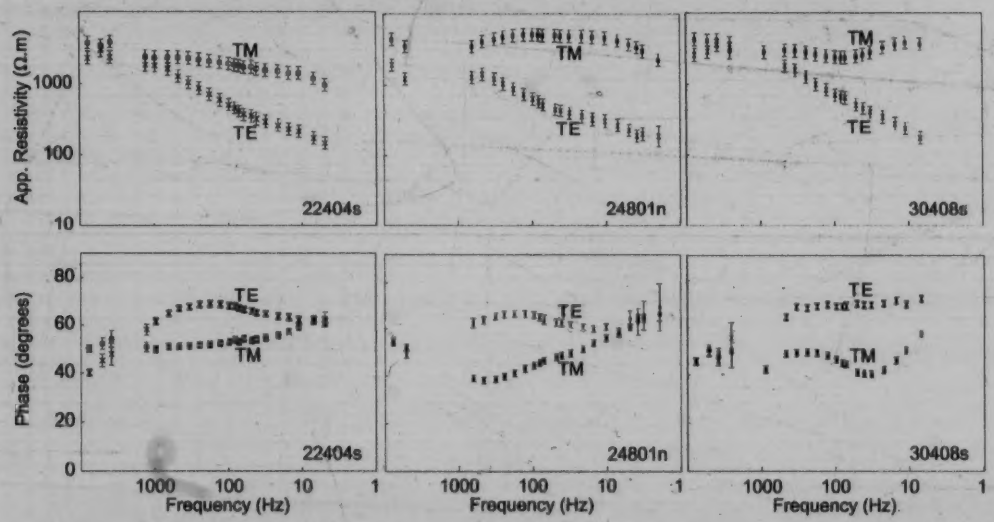

Figure 5-6. Sample data curves of TE and TM mode AMT data for stations on lines 224, 248 and 304. Note that there are no data near 2 KHz in the AMT dead band.

5.5. Pseudosections

When a profile of AMT stations has been collected, it is convenient to display the results as a pseudosection (Figure 5-7). Pseudosections for the other profiles are presented in Appendix A. Over a 2D earth, the TE and TM modes give different apparent resistivity values and are sensitive to different aspects of the subsurface structures. The TE mode is the most sensitive to along strike conductors, whereas the TM mode is the most sensitive to along strike resistors (Berdichevsky et al., 1998). The pseudosection illustration in Figure 5-7 shows limited site-to-site variation in apparent resistivity in the TE mode because the electric field is parallel to the geoelectric strike. Since the current flow is parallel to the strike there is no edge effect at the boundaries of conductors. Thus, site-to-

site variation is relatively smooth in the TE mode. However, the TM mode pseudosection shows more site-to-site variation because near surface bodies strongly affect the TM apparent resistivity. Current flows across the structure and it shows an edge effect at the boundaries of the structure, since there is a sharp change in the physical properties of the media. In the TE mode pseudosection, the location of the conductor is indicated by generally lower apparent resistivities in the centre of the profile. On the other hand, the TM mode is less sensitive to the presence of the basement conductor than the TE mode.

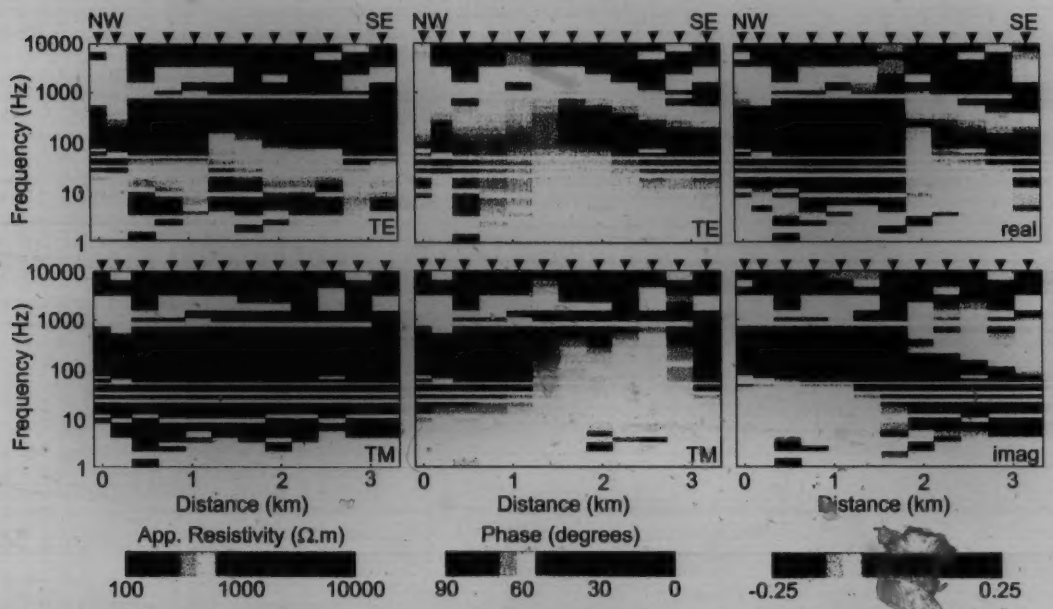

Figure 5-7. Pseudosections of the AMT data of line 224 with the defined strike direction of N45°E. White areas show deleted data (i.e. AMT dead band).

A 2-D Earth generates vertical magnetic fields that are part of the TE mode. When plotted in map form as induction vectors, they have the property that they reverse direction above conductors. The vertical magnetic field can be written as

$$H_z = T_{zx}H_x + T_{zy}H_y \qquad (5.3)$$

where T_{zx} and T_{zy} are defined as projections of the magnetic field transfer function (tipper). In a purely 2-D situation the TE mode has H_x zero and the vertical magnetic field transfer function is defined by just T_{zy}. The real part of this transfer function can be plotted as a pseudosection, as in Figure 5-7. Note that it changes sign at a distance of 1.5 km, indicating the presence of a conductor.

5.6. Conclusions

The AMT data at McArthur River are characterized by a geoelectric strike direction of N45°E and which is parallel to the known geology. Low r.m.s. misfits of the tensor decomposition indicate that the data are relatively 2D. Dimensionality analyses suggest that there is no strong distortion in the McArthur River AMT data. Induction vectors also indicate a relatively 2D structure, but also reveal some more complicated near surface structure. Having understood the dimensionality of the subsurface, the AMT can now be inverted, as described in the following chapter.

6. INVERSION OF THE McARTHUR RIVER AMT DATASET

In the previous chapter, it was shown that a 2D analysis is justified for the McArthur River AMT data set. Therefore, 2D inversion was applied to the data set to determine the subsurface resistivity structure. The large, evenly distributed AMT data set also allows a 3-D inversion to be used to investigate the validity of the 2-D approach. This was in the spirit of the EXTECH IV project since it allowed a new method to be rigorously evaluated for use in the Athabasca Basin as well as in similar basins worldwide.

6.1. Two Dimensional Magnetotelluric Inversion

Tensor decomposition and induction vectors showed that the McArthur River AMT data were relatively 2-D. Thus an initial approach was to use a standard 2-D inversion to convert the frequency domain MT data into a model with true depth on the vertical scale. Iterative linearised inversion is the most widely used approach for solving nonlinear inverse problems of geophysics (Oldenburg, 1990). In this approach, an initial resistivity model is generated and the predicted MT data are computed. The difference between the predicted and measured MT data is then computed. The model sensitivities are then computed and used to calculate a change in the resistivity model that will improve the fit to the measured MT data. This process is repeated (iterated) until a stable resistivity model is obtained that fits the MT data. Another key concept is that the model must be regularized (Tikhonov and Arsenin, 1977). This is needed since there are generally more model parameters than data points and this leads to an underdetermined problem. Extra constraints are developed from the requirement that the model satisfies some additional conditions e.g. it is spatially smooth, close to some *a priori* model etc. In the last 15 years, 2D inversions for MT data have advanced significantly. Computer speed and memory previously limited the size of model that could be used and approximations had to be made in order for the inversion to run in a reasonable time. For example the Rapid Relaxation

Inversion (RRI) approach of Smith and Booker (1991) used an approximation for the sensitivity of data values to model parameters. With faster computers and larger memory, direct solutions are now possible with exact computations of the sensitivities (a) 2D Occam MT (Constable et al., 1987; deGroot-Hedlin and Constable, 1990) , (b) ABIC (Uchida 1993a; 1993b) (c) NLCG - Rodi and Mackie (2001) (d) REBOCC in 2D (Siripunvaraporn and Egbert, 2000). One of the most widely used of these inversions is that of Rodi and Mackie (2001) and this was used primarily in this study. The NLCG algorithm has a number of advances that make it both stable and computationally efficient. One of the most important of these is the use of non-linear conjugate gradients to compute the sensitivities. The sensitivities are not directly computed which avoids the storage of a very large array of numbers.

6.1.1. Two-dimensional inversion of the audio magnetotelluric data from the McArthur River

The AMT data were inverted using the NLCG6 algorithm of Rodi and Mackie (2001). This inversion seeks a resistivity model that fits the observed AMT data, and also satisfies a specified regularisation function. This generally requires a spatially smooth resistivity model but can also include other requirements.

The initial approach was to separately invert the individual components of the AMT data. The TE mode, the TM mode and T_{zy} were inverted separately to check the internal consistency of the AMT data (Figure 6.1). As expected the TE mode is most sensitive to along strike conductors and clearly images a conductor in the centre of the profile 224. This feature is not seen in the TM-mode only inversion because TM mode is quite insensitive to conductors (Berdichevsky et al., 1998). The T_{zy} data locate the horizontal position of the conductor very well, but do not reliably determine the depth. As mentioned in the previous sections, the three components of the data are sensitive to different aspects of the sub-structures and give different subsurface images (Figure 6-1). Therefore, to obtain a reliable image of the subsurface resistivity, a joint inversion is needed (Figure 6.1). The basement conductor is sharper in the TE-TM inversion and also the resistive features are more obvious when compared to the TE mode inversion. The joint inversion of the TE mode and T_{zy} data also gave similar results. The TM–T_{zy} joint inversion result was somewhat different to the others and is more

similar to the TM mode result. Inclusion of the vertical magnetic field data exhibits more evidence of the conductor. In addition, the TE-TM-T_{zy} joint inversion images a strong conductor that begins at a depth of 550 m (Figure 6-1), which is coincident with the depth of the unconformity at this location. It was found that the TE-TM and the TE-TM-T_{zy} inversions gave the most reliable images of the subsurface. This these two inversions were used for the interpretation of the data.

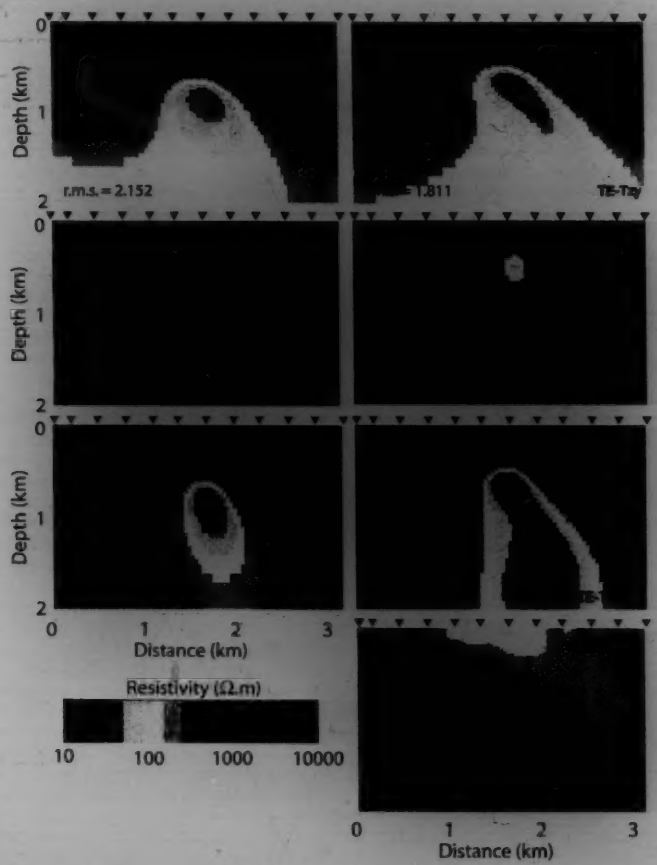

Figure 6-1. Resistivity models derived for profile 224 with 2D AMT inversions. Black triangles show the station locations and there is no vertical exaggeration.

Figure 6-1 also shows the root mean square (r.m.s.) misfit values for each inversion. The r.m.s. misfit expresses the statistical difference between the measured AMT data and the response predicted by the inversion model. Error floors of 20 %, 5 % and 0.025 were applied to apparent resistivity, phase and tipper respectively. The error floor is the minimum standard error that can be allowed for an individual data point. If the declared standard error is less than the

error floor, then the standard error is increased to the defined error floor. This approach is used to ensure that a large proportion of the data points are fit, rather than just those with the smallest standard errors. An ideal r.m.s. misfit value should be between 1-2. If the r.m.s. misfit is lower than 1, then this may mean that the AMT data are being overfit or that the standard errors are too large. If the r.m.s. misfit is higher than 2, then this means that the inversion model is not fitting the data or that the declared standard errors are too small. A range of error floors were used, but when lower values were used for apparent resistivity, the models were quite rough. The r.m.s. misfit values obtained are generally acceptable. The AMT data and the fit to the measured data are shown in Figure 6-2 at selected stations on line 224. Small scale structure at the surface or very thin overburden layer may cause a static shift in the AMT resistivity curves (Jones, 1988). However, no serious static shifts were observed in this AMT data set. Static shifts encountered in the McArthur River dataset were quite small that it was not necessary to correct for them explicitly in the 2D inversion.

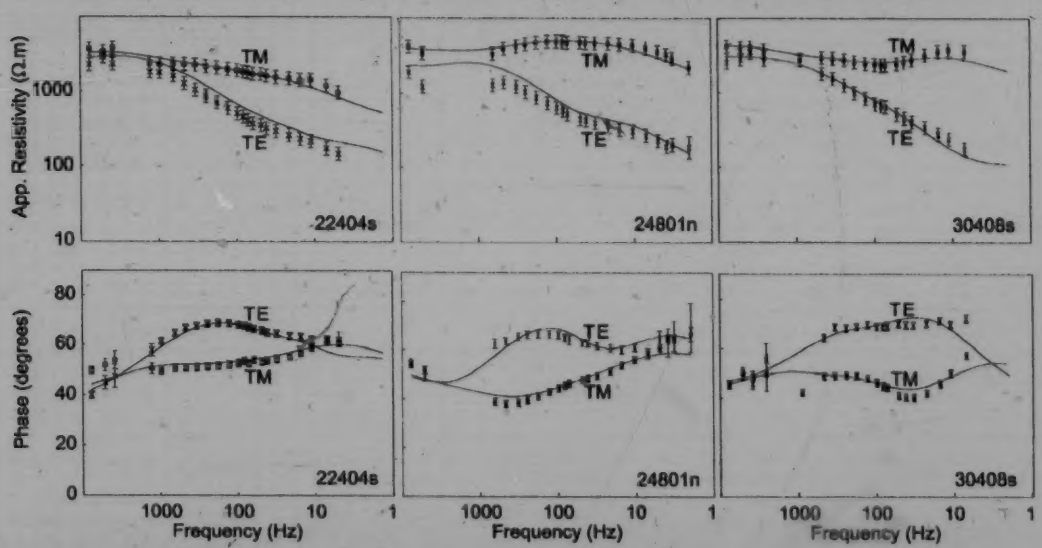

Figure 6-2. Sample data curves of TE and TM mode data for stations on profiles 224, 248 and 304. Continuous lines show the fit of the response of the inversion models for the TE mode and TM mode data. These data are shown in Figure 5-7 (Figure is taken from Tuncer et al., 2006a).

The inversions shown in Figure 6-1 were repeated for all profiles of the McArthur River AMT data set (Figure 5-1) and these inversion models are presented in Appendix B. Figure 6-3 shows the r.m.s. misfit values of the TE-TM and TE-TM-T_{zy} inversions for each profile and indicates that they are satisfactory.

Only around the mine area (profile 276) was the r.m.s. misfit value significantly higher. This might be because of the gap on line 276 or because the mine itself is located on this profile. In the latter case, EM noise from the mine may have degraded the quality of the AMT data. However, such an effect was not obvious in the AMT time series data recorded at these sites.

Figure 6-4 illustrates the resistivity models obtained by TE-TM and TE-TM-T_{zy} 2D inversions. Both inversion models are similar except for line 276, which was discussed above. Although the TE-TM inversion generally gives a better fit to the AMT data (see the r.m.s. misfit values in Figure 6-3), this resistivity model differs significantly from the other TE-TM models. The TE-TM inversion shows a strong conductor at the surface while the TE-TM-T_{zy} inversion for the same profile places it deeper, as observed on other profiles. Thus, the TE-TM model of profile 276 should not be considered reliable.

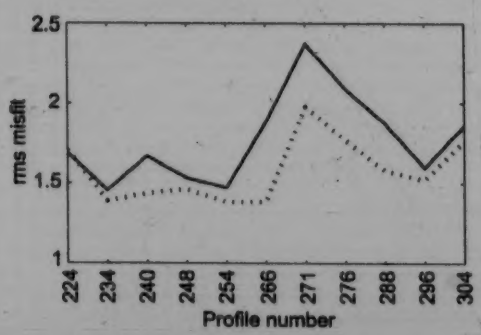

Figure 6-3. The r.m.s. misfit values for TE-TM (dashed) and TE-TM-T_{zy} (solid) inversions for each profile (Figure is taken from Tuncer et al., 2006a).

As noted earlier, the induction vectors in Figure 5-6 suggest a departure from a simple 2D geometry for the northern AMT profiles (266 – 304). Thus the tipper data from northern profiles must be used with caution. Although the TE-TM-T_{zy} results give low r.m.s. misfits for profiles 224 – 254, the TE-TM inversions could be more reliable than for other profiles. The r.m.s. misfits shown in Figure 6-3 also support this idea because the TE-TM-T_{zy} inversions have smaller r.m.s. misfit values for line 224, possibly because of the two-dimensionality indicated by the profile parallel induction vectors (Figure 5-6). The r.m.s. misfits are higher for the TE-TM-T_{zy} inversions where the induction vectors are not parallel to the profiles, perhaps indicating 3D or anisotropic effects in the McArthur River AMT data set.

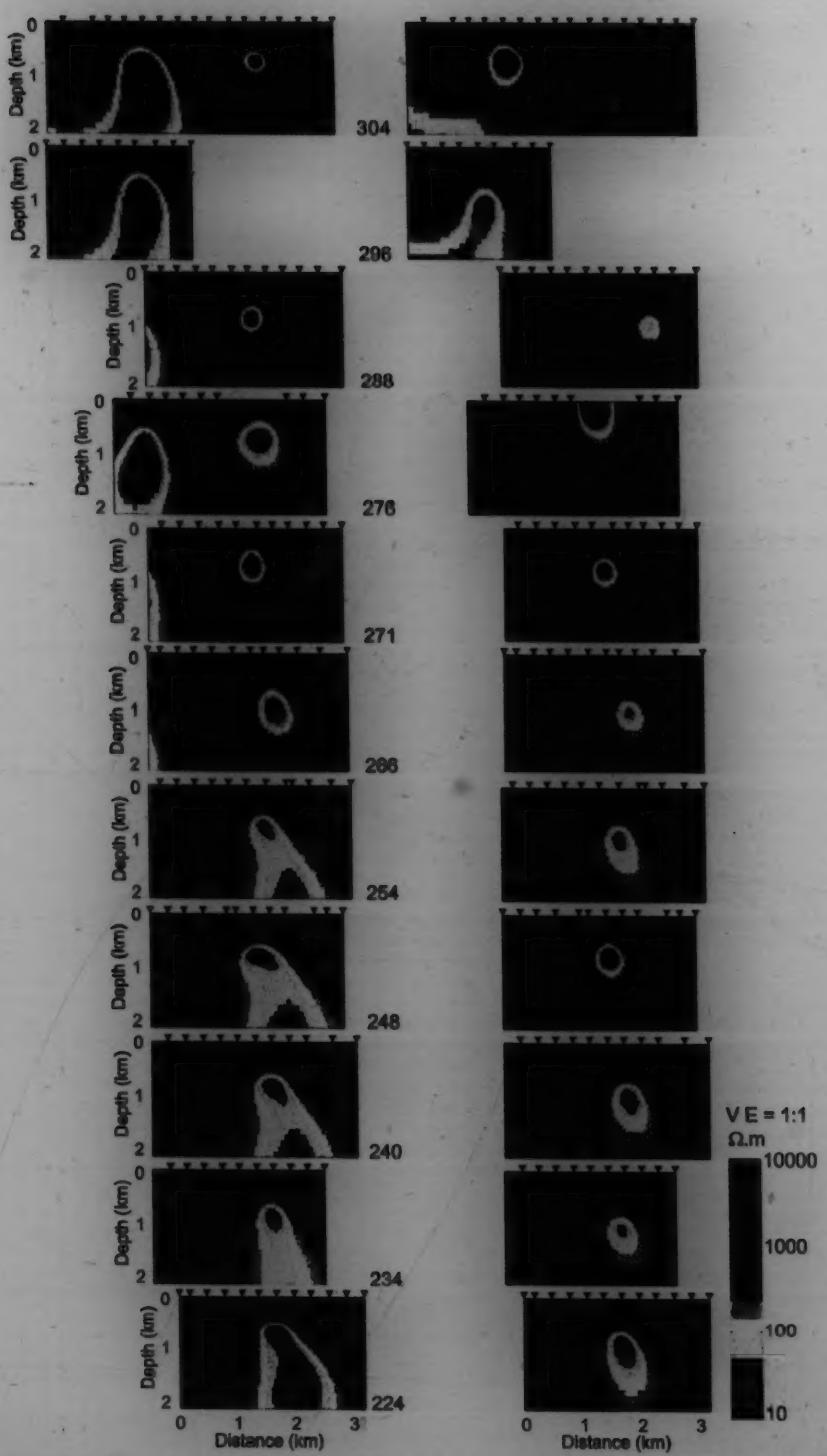

Figure 6-4. Resistivity models for all profiles derived with 2D inversions. Left column shows the TE-TM-T_{zy} inversions and the right column shows the TE-TM inversions (Figure is taken from Tuncer et al, 2006a).

To examine the robustness of the 2D inversion models, a range of inversions were performed with different inversion control parameters. (Figure 6-5). The smoothing parameter τ controls the trade-off between fitting the AMT data and producing a spatially smooth model. A higher value of τ gives a smoother model, whereas a lower value of τ gives a rougher model. The parameter α controls the ratio of horizontal to vertical smoothness. Higher values of α give horizontally smooth resistivity models, while lower values of α give vertically smooth resistivity models. Thus, for layered Earth models, high values of α would be more appropriate. In contrast, a low value of α would be more appropriate for vertical geological structures such as faults and dikes. The inversions in Figure 6-4 used τ=10 and α=1 and gave results typical of a broad range of τ and α values.

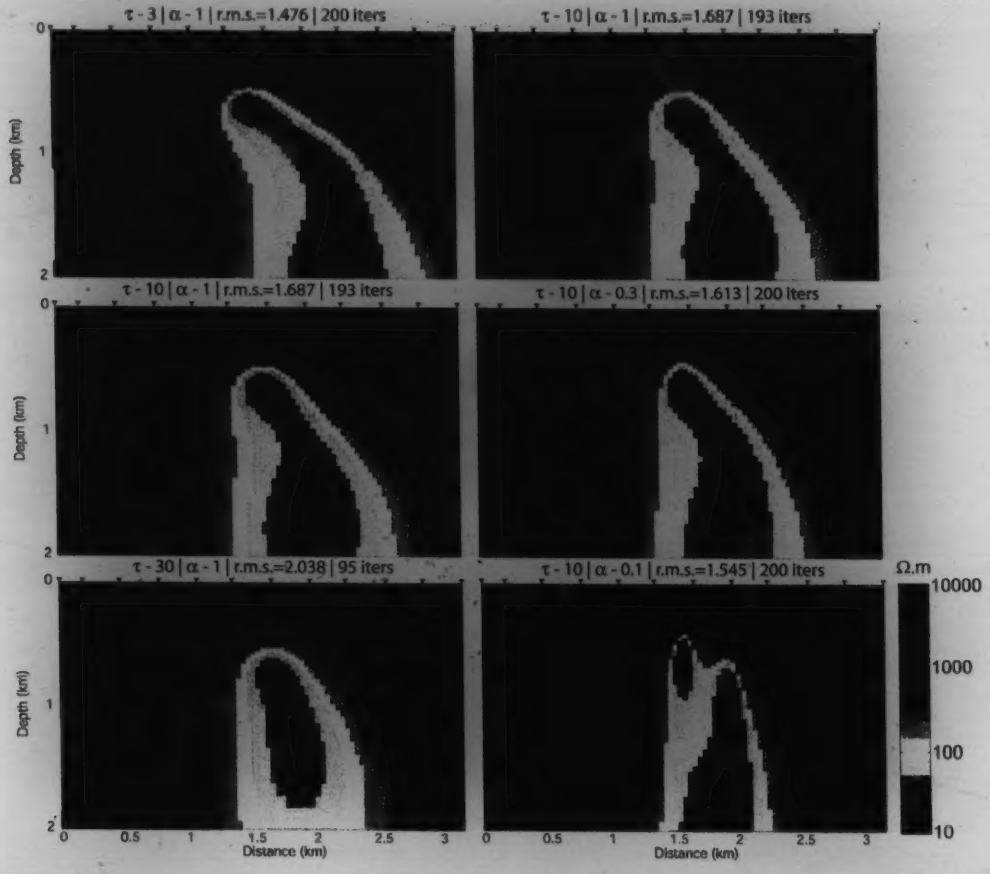
τ - 3 | α - 1 | r.m.s.=1.476 | 200 iters
τ - 10 | α - 1 | r.m.s.=1.687 | 193 iters
τ - 10 | α - 1 | r.m.s.=1.687 | 193 iters
τ - 10 | α - 0.3 | r.m.s.=1.613 | 200 iters
τ - 30 | α - 1 | r.m.s.=2.038 | 95 iters
τ - 10 | α - 0.1 | r.m.s.=1.545 | 200 iters
Depth (km)
Distance (km)
Ω.m
10000
1000
100
10

Figure 6-5. Inversion results for profile 224 with different τ values (3, 10 and 30) and α=1 (left panel), and α values (1, 0.3 and 0.1), and τ=10 (right panel). r.m.s. misfit values and iteration numbers are also given in the figure for comparison.

Figure 6-5 shows the inversion models obtained with different smoothing parameters. In the left panel of Figure 6-5, α =1 and τ = [3, 10, 30] from top to bottom. Figure 6-5 shows that the inversion model does not change significantly as τ is varied. In the right panel of Figure 6-5, τ =10, and α = [1, 0.3, 0.1] from top to bottom. Only the lowest α value gives a model that is significantly different from the other five models. Thus the models obtained with default values τ=10 and α=1 can be considered stable, and not dependent on a specific choice of these parameters.

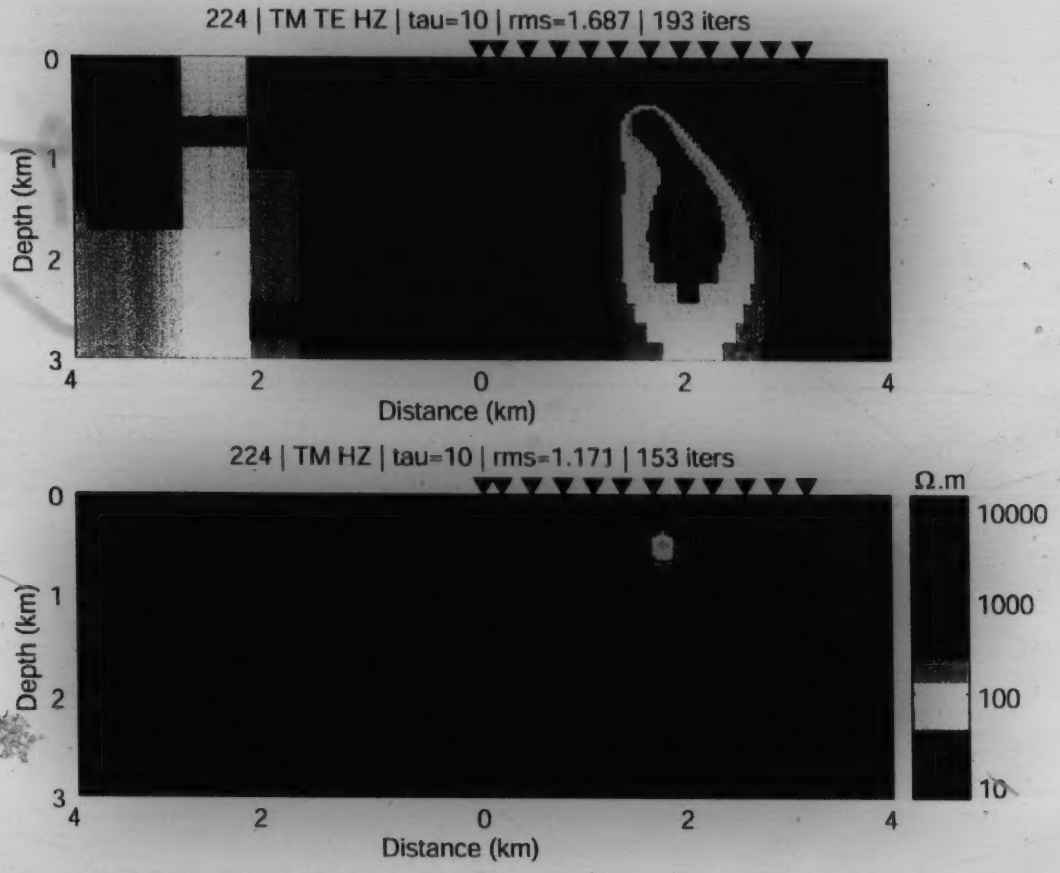

Figure 6-6. Models obtained by TE-TM-T_{zy} and TM-T_{zy} inversions of the AMT data on profile 224. These inversions illustrate the presence of a second conductor to the northwest of the survey area.

The conductor imaged in the 2D inversions is clearly located in the basement with the top at a depth of approximately 500 m. It extends to a depth of at least 2 km. In the southwestern part of the McArthur River area, the conductor appears to dip to the southeast. Around the mine, the conductor is weaker, but

the AMT data from these profiles are lower in quality than data from other profiles. In the northeastern part of the survey area, two basement conductors are imaged. The second stronger conductor could be another graphitic fault northwest of the main conductor (P2 reverse fault). The inversion results suggest that the second conductor may extend to the southwest, because the same feature can be seen just beyond the northwest end of the models for profiles 224 – 248 (this part of the models is not shown in Figure 6-4). A representative model is shown in Figure 6-6 for profile 224. It is expected that the tipper data require this second conductor because tipper data are sensitive to the conductors that are not beneath the station locations. However, the TM-T_{zy} joint inversion does not image this second conductor. It appears that only the TE mode data detect this conductor. This indicates that the requirement for a second conductor should be tested further.

The induction vectors, shown in Figure 5-6, also indicate the presence of two conductors. This is clear at a frequency of 100 Hz, where the induction vectors at the northwest end of lines 240, 248, 254, 266 and 271 may indicate another conductor (Tuncer et al., 2006a). This result is also consistent with the presence of a conductor at the western edge of the survey area, but is in contrast to the TM-T_{zy} joint inversion result.

The other feature that is obvious in the model shown in Figure 6-4 is a resistive halo (5000 -10000 Ω.m) above the basement conductor, above the unconformity. This feature is clearest on lines 224 – 254. The reason for this resistive feature could be silicification associated with the uranium ore formation (see Chapter 2). However, it could also be an artefact of the regularization used in the inversion. The high resistivity contrast between the graphitic conductor and the metamorphic host rock may cause this artefact (Mackie, R. L., personal communication, 2006). This is tested with synthetic inversions in the next chapter.

However, it is clear from 1D studies that AMT is inherently sensitive to the presence of a resistor associated with silicification. A synthetic AMT response was calculated from the resistivity depth profile assuming a layered earth model (1D) at the location of well MAC265 (Craven et al., 2002; 2007). A resistive zone between 140 and 240 m might represent the silicification.

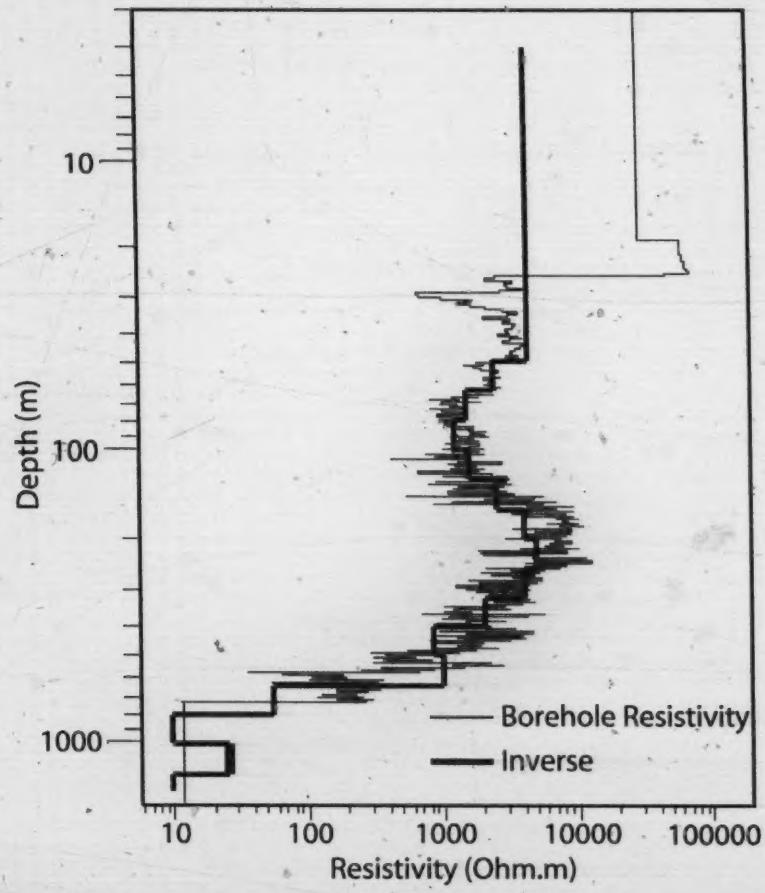

Figure 6-7. Plot of well log resistivity and 1-D AMT inversion at borehole MAC265 (Craven et al., 2002; 2007). The resistive zone in the depth range 140-240 metres were interpreted as silicified alteration zone. This image suggests that 1D AMT modelling can be used to locate silicified zones.

6.2. Three Dimensional magnetotelluric Inversion

The EXTECH-IV AMT data coverage at the McArthur River site is appropriate for three dimensional (3-D) inversion studies. Therefore a number of 3D inversion algorithms were applied to the AMT data set. The first 3D inversion that was used was the Reduced Basis Occam's (REBOCC) algorithm of Siripunvaraporn et al. (2005a). This is a modified version of Occam's inversion technique. In the original Occam's inversion (Constable et al., 1987; deGroot-Hedlin and Constable, 1990) the computation was performed in the model space. However, there are typically more model parameters than data values and this approach becomes very inefficient when the model has many parameters, such

as in a 3-D inversion. Siripunvaraporn and Egbert (2000) reformulated the 2D Occam inversion for MT data into the data-subspace, which requires less computation time than in the model space. Siripunvaraporn et al. (2005a) extended this method into 3D for magnetotelluric inversion.

Figure 6-8 shows vertical slices of the resistivity model obtained from the 3D TE-TM joint inversion of the REBOCC algorithm. There are some similarities and some differences when compared to the 2D inversions. The models for the southern profiles are similar in both the 2D and 3D inversions. The conductor associated with the P2 fault is very prominent in these sections. Another conductor is also visible and it is closer to the P2 fault on the northern profiles. Resistivity sections for the northern profiles are more complicated with a number of basement conductors present. The P2 conductor is not that conspicuous and disappears on lines 296 and 304. Resistivity models for lines 271, 276 and 288 may indicate the presence of three basement conductors. This may need further analysis that includes more 3D inversion runs with different parameters or different starting models. Unfortunately, the 3D AMT inversion is very time consuming and this has not been possible.

To make the computation times reasonable, a coarse mesh was used with size of 56 x 56 x 33, aligned parallel and orthogonal to the survey lines. This can be compared to the relatively fine meshes used in 2D inversions (i.e. 0 x 180 x 90 for line 304). In addition, only the off-diagonal elements (Z_{xy} and Z_{yx}) of the impedance tensor were inverted at 16 frequencies for 131 sites (Craven et al., 2006; Tuncer et al., 2006a). As shown in chapter 4, diagonal elements are non-zero in 3D case. Thus, using only off-diagonal elements might reduce the effect of 3D structures.

To test the stability of the 3D REBOCC inversion, the AMT data were also inverted using the 3D NLCG algorithm of Mackie et al., (2001). The NLCG6 inversion includes the vertical magnetic field and inverts all four elements of the impedance tensor. Including diagonal tensor elements in the 3D inversion allows a more reliable imaging of 3D structures. In addition, the NLCG6 inversion can estimate static shifts coefficients. Static shifts are small, frequency-independent offsets of the apparent resistivity curve caused by near surface structure. In total, 9 frequencies were inverted in the frequency band 10-1000 Hz. Error floors were 5 % for off-diagonal element, 20 % for diagonal elements and 0.02 for tipper. The mesh size that was used in the 3D NLCG modelling algorithm was 56 x 44 x 79.

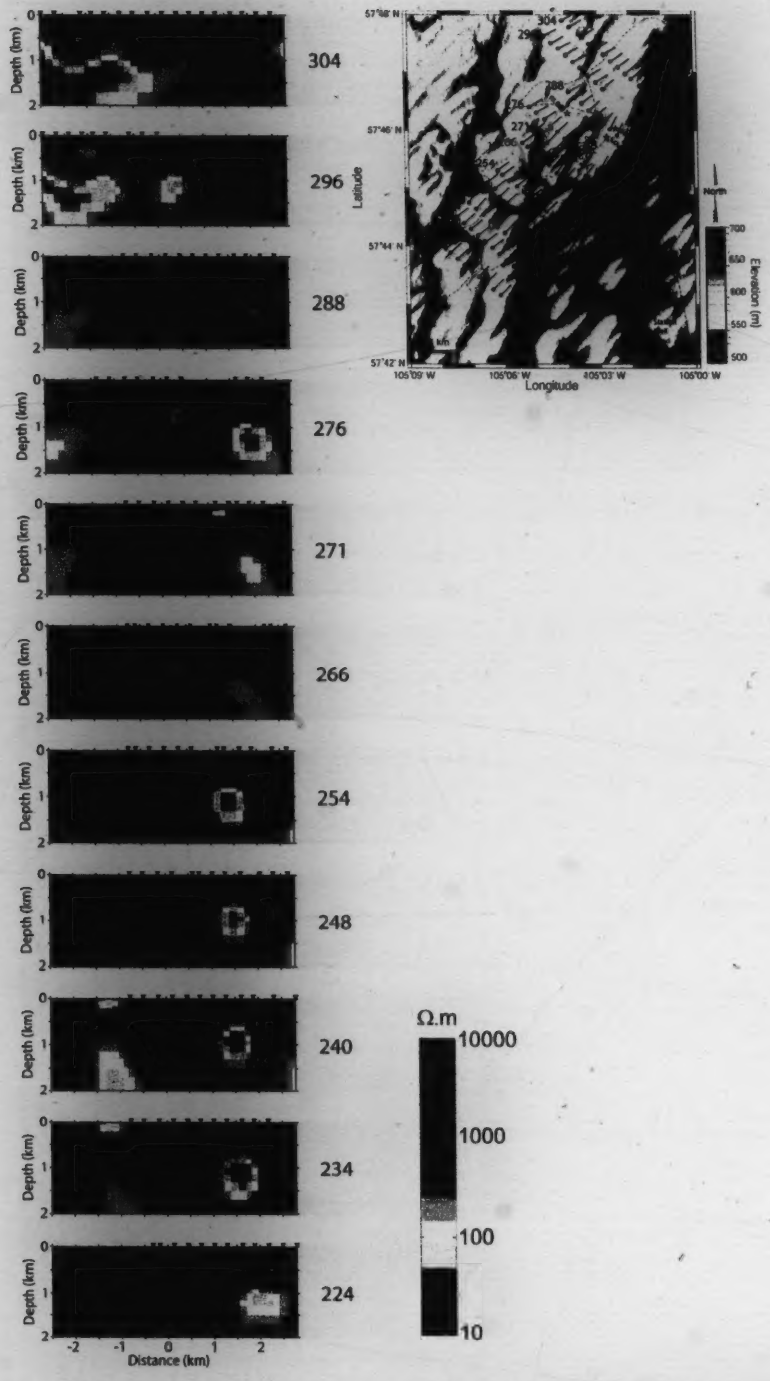

Figure 6-8. Vertical slices of the 3D TE-TM inversion using the REBOCC algorithm. The starting model was a 1000 Ω.m halfspace and the horizontal to vertical smoothing was set to unity. The error floor of the impedance was taken as 5 %. The initial and the final r.m.s. misfit values were 5.56 and 1.38 respectively.

Figure 6-9 shows a comparison of the resistivity models obtained by different inversion algorithms. In general the models are quite similar and all image the same first order resistivity features. However, there is more similarity between the models obtained by the 2D and 3D NLCG inversions than between models derived from the NLCG and REBOCC inversions. This is probably due to the fact that NLCG and REBOCC algorithms used slightly different datasets. Overall, similarities between the models suggest that both 3D inversions are reliable.

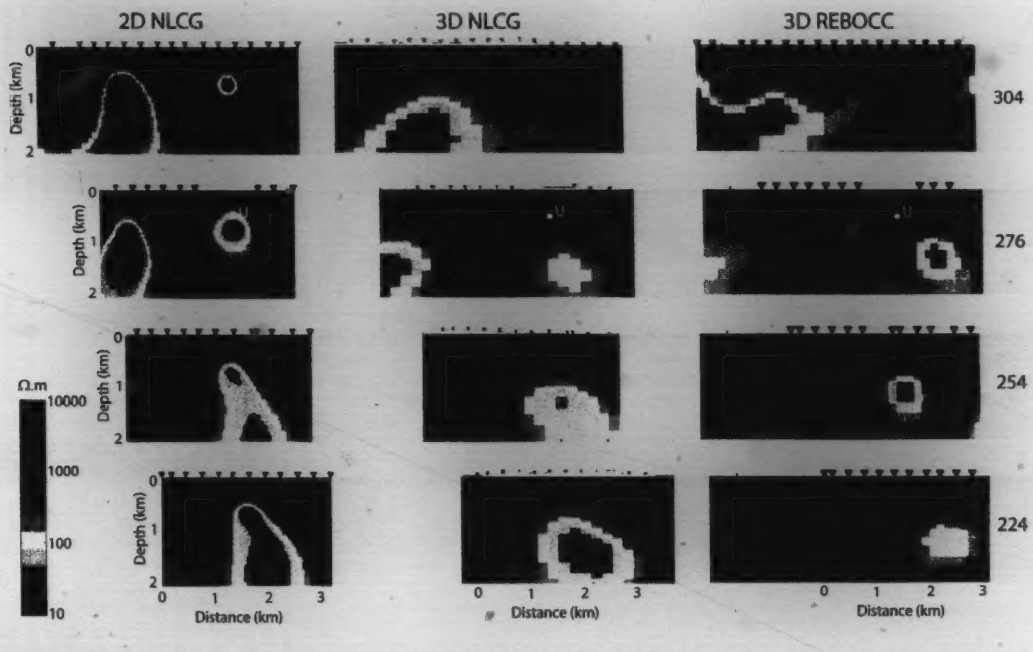

Figure 6-9. Comparison of the REBOCC and NLCG6 inversions for profiles 224, 254, 276 and 304. Note that NLCG algorithms included the vertical magnetic field data into the 2D and 3D inversions as well as the TE and TM mode data. REBOCC algorithm just used the TE mode and TM mode data for the 3D joint inversion. White squares on profile 276 show locations of the uranium pods of the McArthur River P2 North deposit.

Figure 6-10 illustrates the horizontal slices of the REBOCC inversion model. At shallow depths the model is mostly resistive and there are no continuous structures that might be interpreted as graphitic basement faults. Below the depth of the unconformity (550 m), a conductive structure can be identified that is probably the P2 fault. It is very obvious in the 800 and 1000 m depth slices, especially on the southern profiles. Another conductor is also obvious in the northwest corner of the survey area. This is consistent with the 2D

inversion results and this conductor was observed on profiles 296 and 304. The P2 conductor begins to disappear at a depth of 2000 m. However, the NW conductor is still strong. All these results demonstrate similarities with 2D inversion results. This correspondence could be confirmed with comparison of the 2D and the 3D results shown in Figure 6-11 and 6-12. Figure 6-11 illustrates the comparison of 2D TE-TM and TE-TM-Tzy inversions with the 3D TE-TM inversion of REBOCC algorithm.

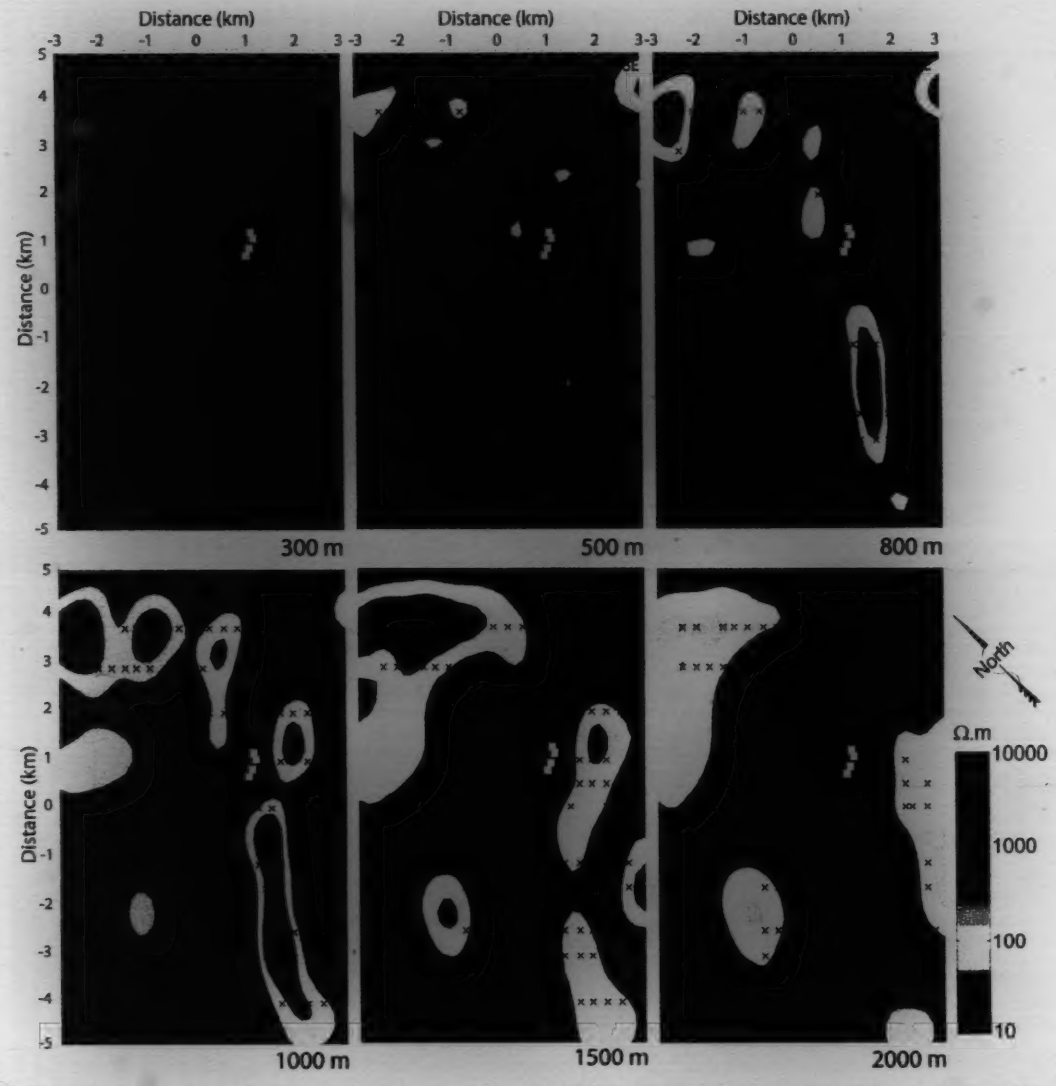

Figure 6-10. Horizontal slices of resistivity contour maps from different depths obtained from 3D inversion results of REBOCC algorithm. White squares show locations of the uranium pods. Cross signs (x) show the locations of the AMT stations of McArthur River.

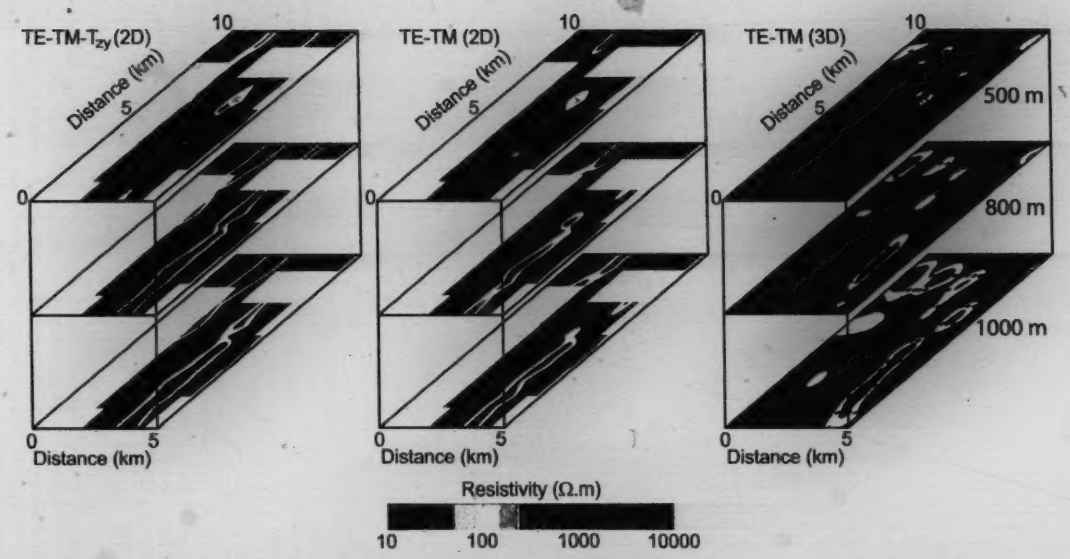

Figure 6-11. Comparison of two dimensional and three dimensional horizontal depth slices at different depths showing the similarities in the McArthur River area (Figure is taken from Tuncer et al., 2006a). White diamonds indicate locations of the uranium pods. Two dimensional inversions used the NLCG algorithm whereas three dimensional inversion used REBOCC algorithm.

Figure 6-12 includes the three dimensional NLCG algorithm and illustrates the comparison of two dimensional and three dimensional TE-TM-Tzy joint inversion with three dimensional TE-TM joint inversion. They all suggest the continuity of the P2 conductor of the McArthur River area at deeper levels and the presence of a second conductor in the northwest part. Thus, these results do not show much difference between the two dimensional and the three dimensional results. However, the conductive zone in the northeast corner of the three dimensional results might indicate another conductor. This zone is also consistent with the high r.m.s. misfit anomaly of the tensor decomposition results (Figure 5-3).

6.3. Comparison of the 2D and 3D Inversions with drill-hole data

There is a good qualitative agreement between the two dimensional and three dimensional inversion models. These inversion models can be further validated by comparison with the well log data that were collected during exploration of the McArthur River site.

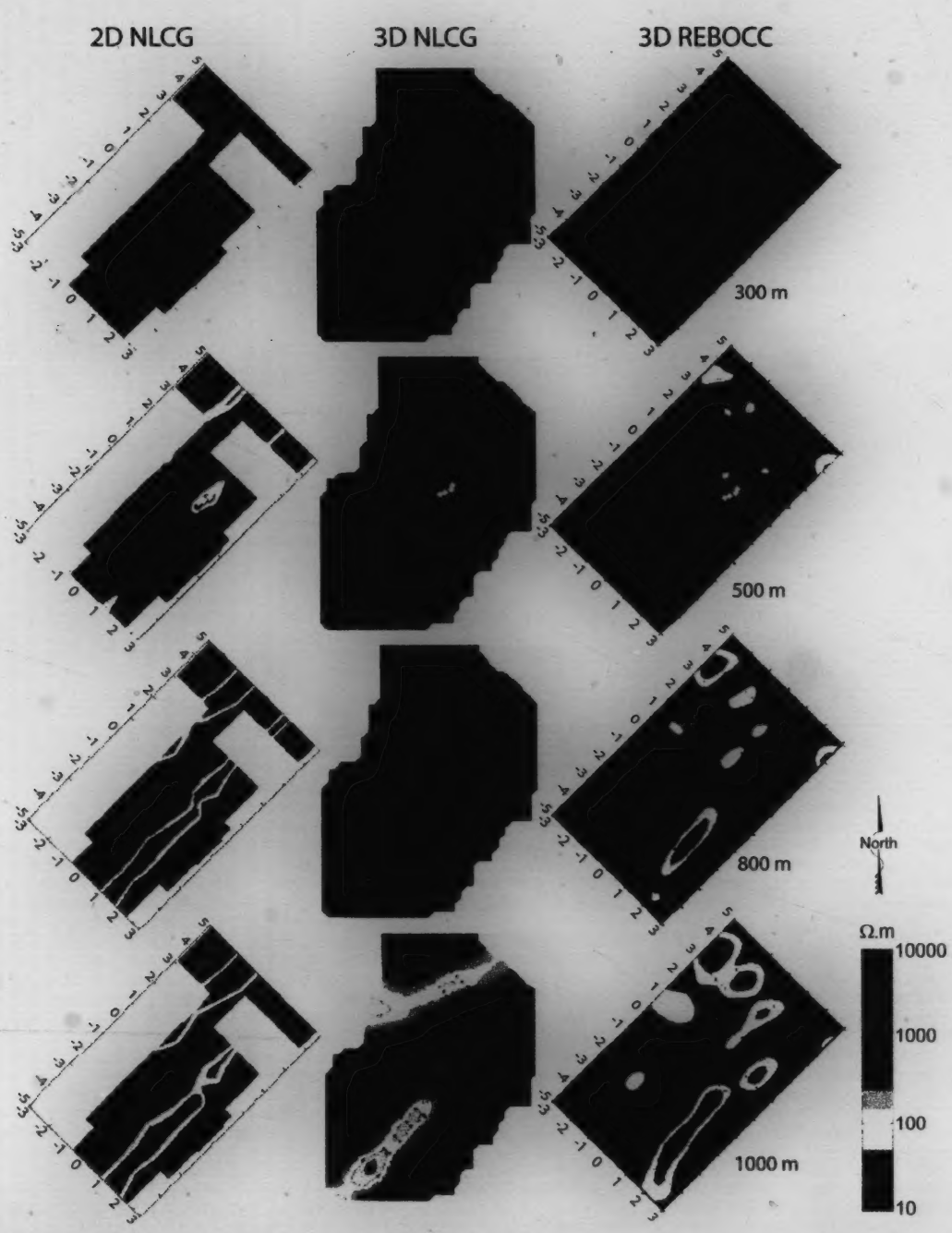

Figure 6-12. Comparison of the horizontal slices of the inversion models derived with NLCG and REBOCC algorithms. Models are shown at depths of 300, 500, 500 and 1000 m. White diamonds show locations of the uranium pods.

Figure 6-13 shows a comparison of resistivity logs and the 2D and 3D inversion models. The agreement between well logs and the 2D and 3D

resistivity models is acceptable in the shallow wells (MC197, MC218, and RL088). However, at depths below 300 m, there are significant differences between the 2D and 3D models that may be a consequence of how deeper structure is smoothed into shallower structure by the inversion algorithms. MC265 and MC266 extend deeper and terminate in a zone of lower resistivity (100 Ω.m) that is well resolved in the 2D inversion model. The 3D model agrees with the well log and 2D inversion at MC266, but agreement is poorer at MC265, perhaps because the location of this well is at the edge of the 3D survey grid. Overall, acceptable agreement is observed between well logs and 2D inversion models. However, the basement conductor is not sampled by the borehole data, and this feature dominates the spatial smoothness of the whole resistivity model. As a consequence, the different regularization used in the 2D and 3D inversion is likely the result of the differences between the 2D and 3D models.

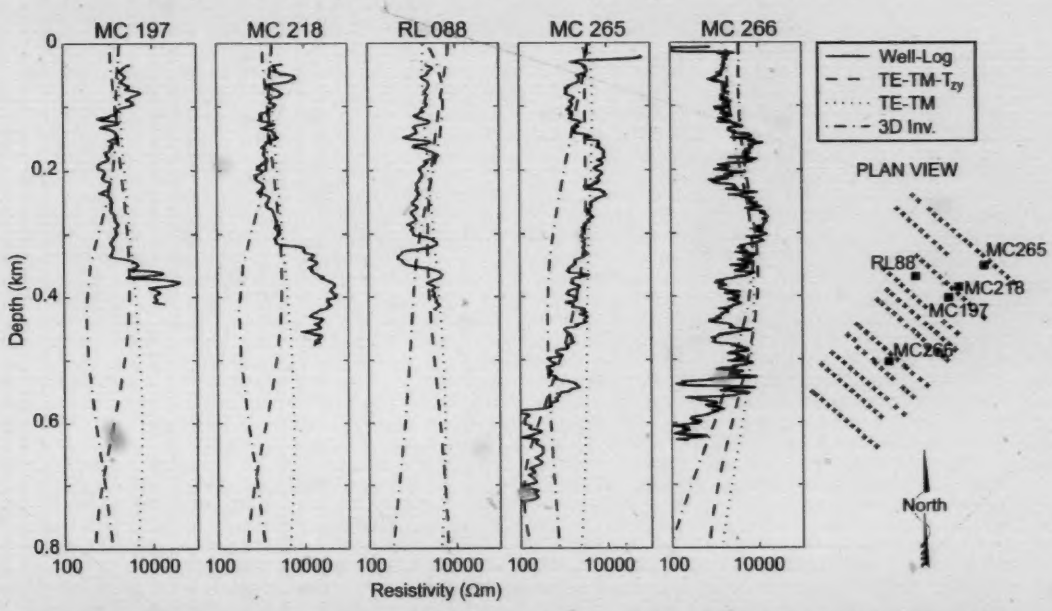

Figure 6-13. Comparison of borehole-log resistivity data (from Mwenifumbo et al., 2004) and the of 2D and 3D joint inversion models (Figure is modified from Tuncer et al., 2006a). A 7-point moving average filter was applied to the resistivity log data to allow a more objective comparison of the two measures of subsurface resistivity.

Another comparison between the inversion models and the resistivity log data is shown in Figure 6-14. Note that the 3D REBOCC inversion did not include the vertical magnetic field data and this makes the comparison less objective

than it could be. Resistivity values in the 2D and 3D models agree well in the centre of the array (line 248), where both the 2D and 3D models are compatible with the well logs. Significant differences are observed between the 2D and 3D models for line 304. These differences may be a consequence of profile 304 being on the edge of the grid of AMT data.

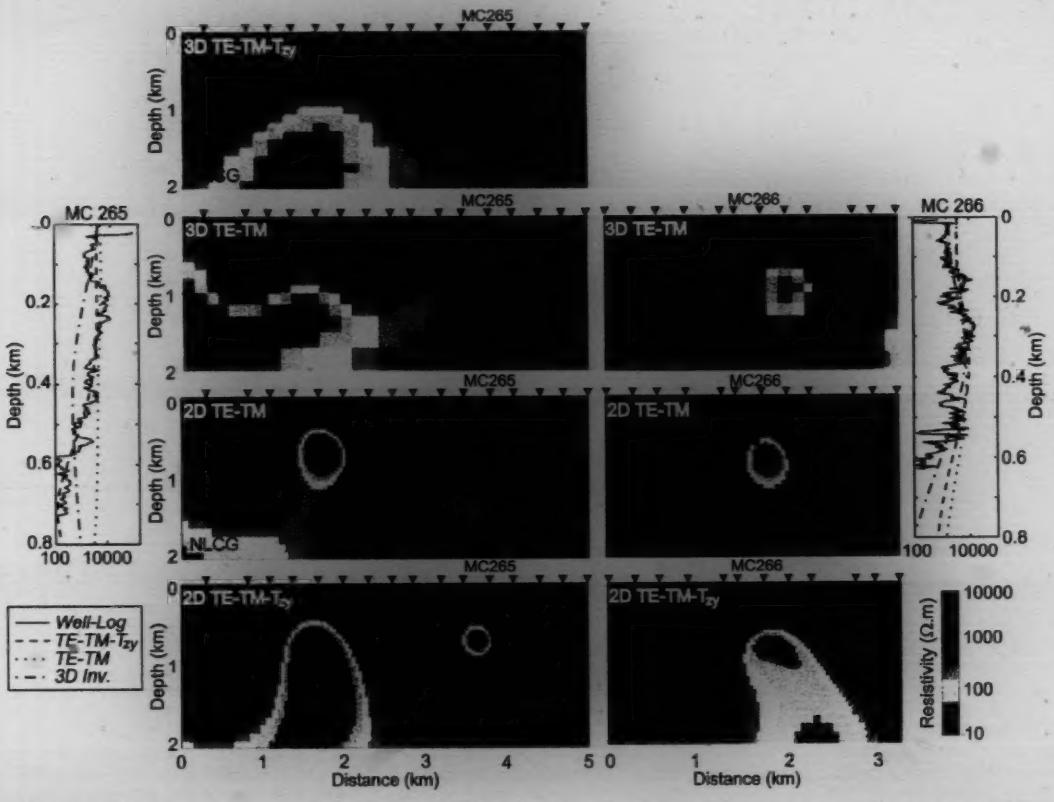

Figure 6-14. Comparison of 2D and 3D inversion results for lines 248 and 304. Comparison with resistivity in adjacent borehole logs is also shown (Figure is modified from Tuncer et al., 2006b).

6.4. Conclusions

A range of 2D inversions were applied to the AMT data with different smoothing parameters. Stable models were obtained that did not depend on a specific choice of regularization parameters. Two southwest-northeast striking conductors were detected at the unconformity depth and appear to dip southeast. These are probably due to graphitic faults in the basement rocks and appear to

dip southeast. The resolution of these models is further examined in the next chapter.

Another feature that might indicate potential uranium mineralization is the alteration zones in the Athabasca sandstone. This zone might be conductive or resistive due to its silica content. A resistive halo imaged above the conductor could be interpreted as the silicified zone, but could also be an artefact of the inversion process. This phenomenon is also examined in the next chapter.

The 2D and 3D AMT inversions generated similar models and justify the use of a 2D inversion in this case. This observation is supported by the results of the tensor decomposition. However, induction arrows do not indicate a perfectly 2D situation and possible explanations for this are also discussed in the next chapter.

7. RESOLUTION AND SENSITIVITY STUDIES

A detailed analysis of the AMT data was presented in the previous chapters and both 2D and 3D inversions were applied to the data. It is vital to evaluate the degree to which the resulting resistivity models are required by the AMT data. This issue is discussed in this chapter through a combination of 2D and 3D forward modelling and inversion.

7.1. Two Dimensional Synthetic Inversions

The sensitivity of the resistivity models to the measured AMT data can be investigated using 2D synthetic inversions. This procedure can reveal whether features in the resistivity models are required by the AMT data or whether they are artefacts of the inversion process. Generic resistivity models were created that contain the basic resistivity features of the unconformity type uranium ore deposits. Forward modelling was then used to compute the predicted AMT data, and Gaussian noise was added. The synthetic AMT data were then inverted using the same parameters as for the inversion of the field AMT data. Many synthetic models were considered but only representative ones will be shown here. The results are illustrated for line 224 and models were compared with those obtained by inversion of the field AMT data.

In the first models, the effect of varying the smoothing parameters was investigated. Model A in Figure 7-1 represents a uranium deposit with a basement conductor and a modest resistivity contrast across the unconformity. A conductive alteration chimney is also present above the basement conductor. Figure 7-1 shows the results of synthetic inversions using different values of α, the factor that controls the ratio of horizontal and vertical model smoothness. Larger values of α generate horizontal structures, while smaller values of α yield vertical structures. Because the target body in this study is a vertical conductor, a choice of $\alpha<1$ is appropriate. Increasing α gives a higher r.m.s. misfit value because a horizontally smooth model is incompatible with the original resistivity

model. Note that the AMT inversion does not recover the correct width of the basement conductor. The smoothing reflects the diffusive physics of AMT exploration, and small features cannot be recovered correctly. The parameter τ controls the trade-off between fitting the AMT data and producing a spatially smooth resistivity model. Increasing the value of τ results in a spatially smoother model (Figure 7-1). Small values of τ produce a rougher model with a second conductor above the basement conductor. This second conductor is clearly an artefact.

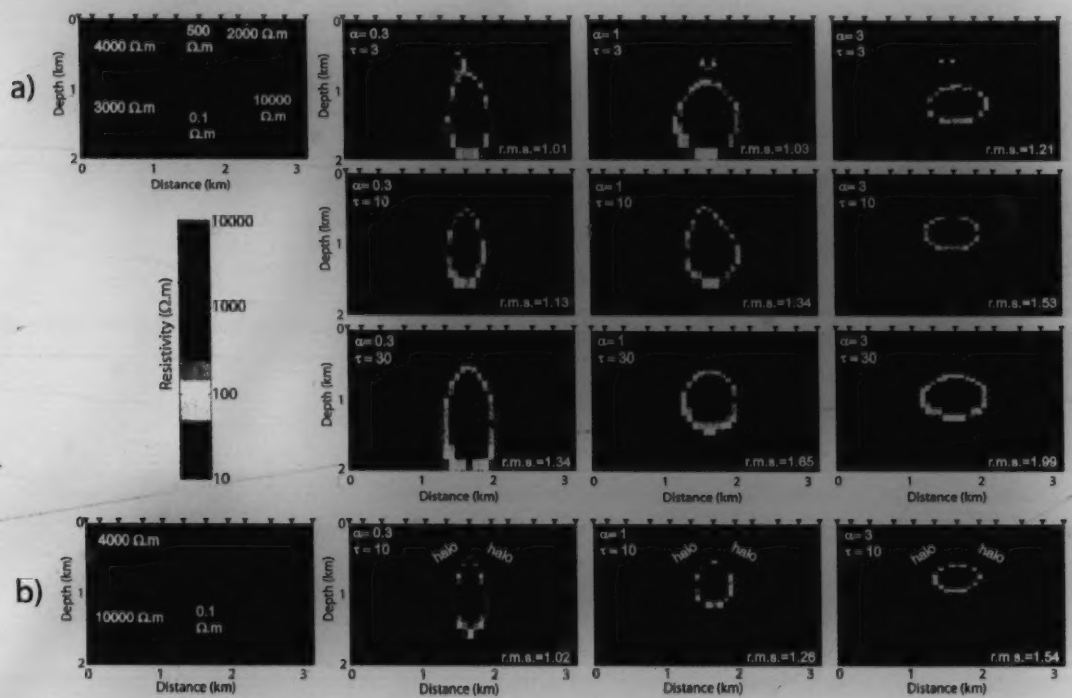

Figure 7-1. Synthetic inversion study showing the effect of different smoothing parameters. (a) This model represents the alteration chimney (500 Ω.m) beneath a 25 m thick, 2000 Ω.m resistive overburden and shows a resistivity contrast across the fault with different smoothing parameters. (b) This model shows a basic two-layer model with a graphitic conductor that has an artificial resistive halo around the conductor.

The synthetic inversion studies suggest that the values $\alpha = 1$ and $\tau = 10$ are the most suitable for the inversion of the measured AMT data. These studies also show that the measured AMT data can image structures up to a depth of 2 km. Synthetic inversions were also used to study whether the AMT data could image the structure of the alteration chimney suggested by McMullan et al.

(1987). The synthetic inversion study shows that a chimney could be resolved by the AMT data. This is clear in model A of Figure 7-1. The absence of such a feature in Figure 6-4 thus suggests a low-resistivity chimney is absent at McArthur River.

Synthetic inversions were also used to determine if a halo of silicification could be imaged with the AMT data. The model in Figure 7-1b includes a simple basement conductor below a 500 m thick layer that represents the Athabasca sandstones. The synthetic inversion produces a high-resistivity halo around the basement conductor. As previously described, this is a consequence of the regularization (smoothing) imposed on the model during inversion. Observing a resistive halo in an inversion model does not imply that one is present in the subsurface. Therefore, the resistive halo in the inversion models could be an artefact of the inversion scheme. However, Craven et al. (2003; 2007) showed that AMT data are sensitive to a resistive zone above the unconformity at the McArthur River area (Figure 6-7).

After investigating the optimal choice of smoothing parameters from the synthetic inversions, the next step was to determine if the EXTECH-IV AMT data could define the geometry of the graphitic faults at the McArthur River mine. For this purpose, a 2D TE-TM-T_{zy} inversion model for profile 224 was chosen as a reference model (Figures 6-1 and 6-4). This model features a conductor dipping to the southeast that apparently increases in thickness with depth. The first model was the dipping conductor that represents the P2 thrust fault at the McArthur River mine (Figure 7-2). The left panel shows the results of an inversion using α=0.3 and a range of τ parameters (3, 10 and 30). The right panel shows the results of synthetic inversions using α=1. This model is quite different to that obtained by inversion of actual EXTECH-IV AMT data. The resulting models do not show any clear dip, except for the first result (α=0.3, τ=3). Therefore it can be concluded that these AMT data are relatively insensitive to the dip of the basement conductors.

The other model included a second basement conductor as suggested by Craven et al. (2007) and illustrated in Figure 7-3. The first inversion shows some similarity to the measured AMT data inversion results but the rest of the inversions are different. In particular, the inversion with values α=1 and τ=10 was very different. Therefore, it can be concluded that this model (Figure 7-3) was not the best model to represent the real geometry of the McArthur River basement

conductor, because the model (Figure 7-3) did not generate a similar response to the measured data inversion response. Furthermore, AMT data suggested that it cannot resolve the two closely spaced basement conductors. However, it showed more similarity than the previous model. The dip is more obvious in this model than the previous one (Figure 7-3).

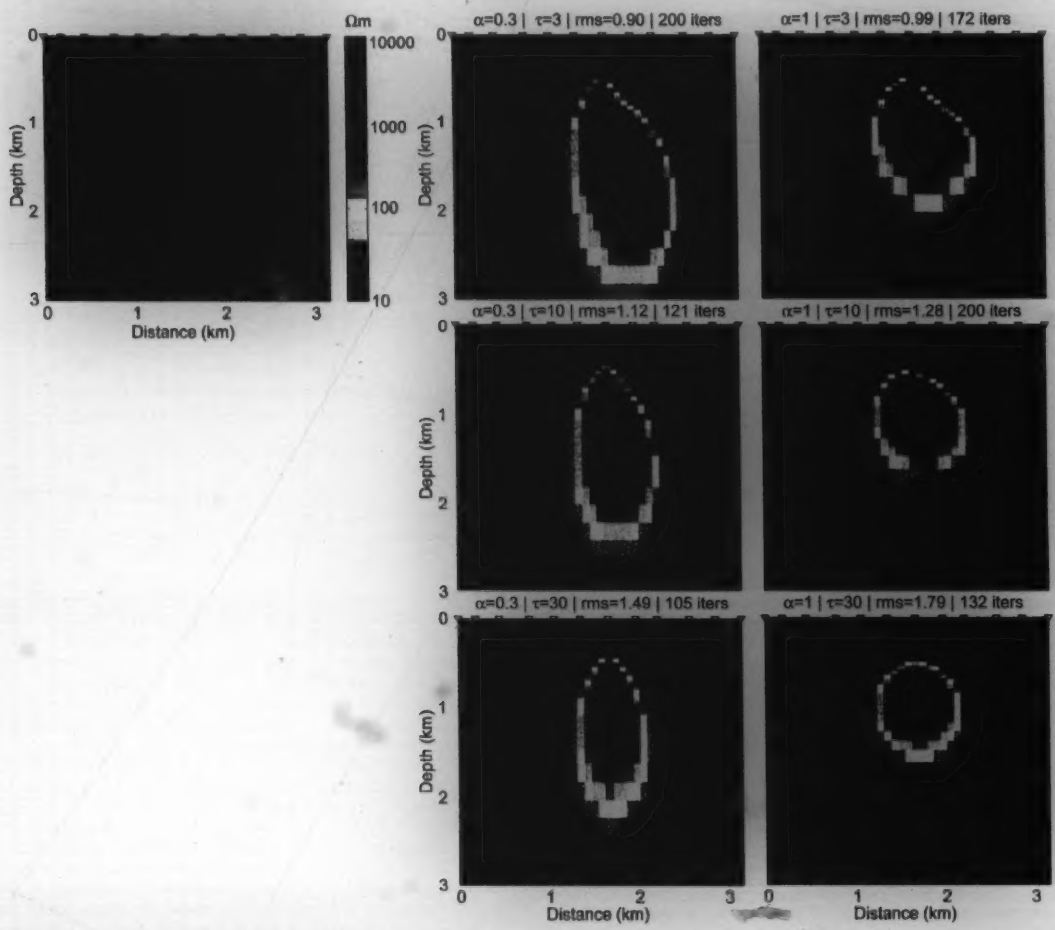
Ωm
10000
1000
100
10
Depth (km)
Distance (km)
α=0.3 | τ=3 | rms=0.90 | 200 iters
α=1 | τ=3 | rms=0.99 | 172 iters
α=0.3 | τ=10 | rms=1.12 | 121 iters
α=1 | τ=10 | rms=1.28 | 200 iters
α=0.3 | τ=30 | rms=1.49 | 105 iters
α=1 | τ=30 | rms=1.79 | 132 iters

Figure 7-2. Synthetic model of dipping basement conductor. The left panel shows the results of an inversion using α=0.3 and a range of τ parameters (3, 10 and 30). The right panel shows the results of synthetic inversions using α=1 and the same τ parameters.

The second model with two conductors showed a greater similarity than the first one with the true model. Therefore, a model with two basement conductors intersecting at depth was investigated, as shown in Figure 7-4. Note that the smoothing parameters were the same as the previous figures. However,

the two separate conductors could not be distinguished in the resistivity model. The dip was observed clearly in this model. However, the desired similarity was not obtained with this model either.

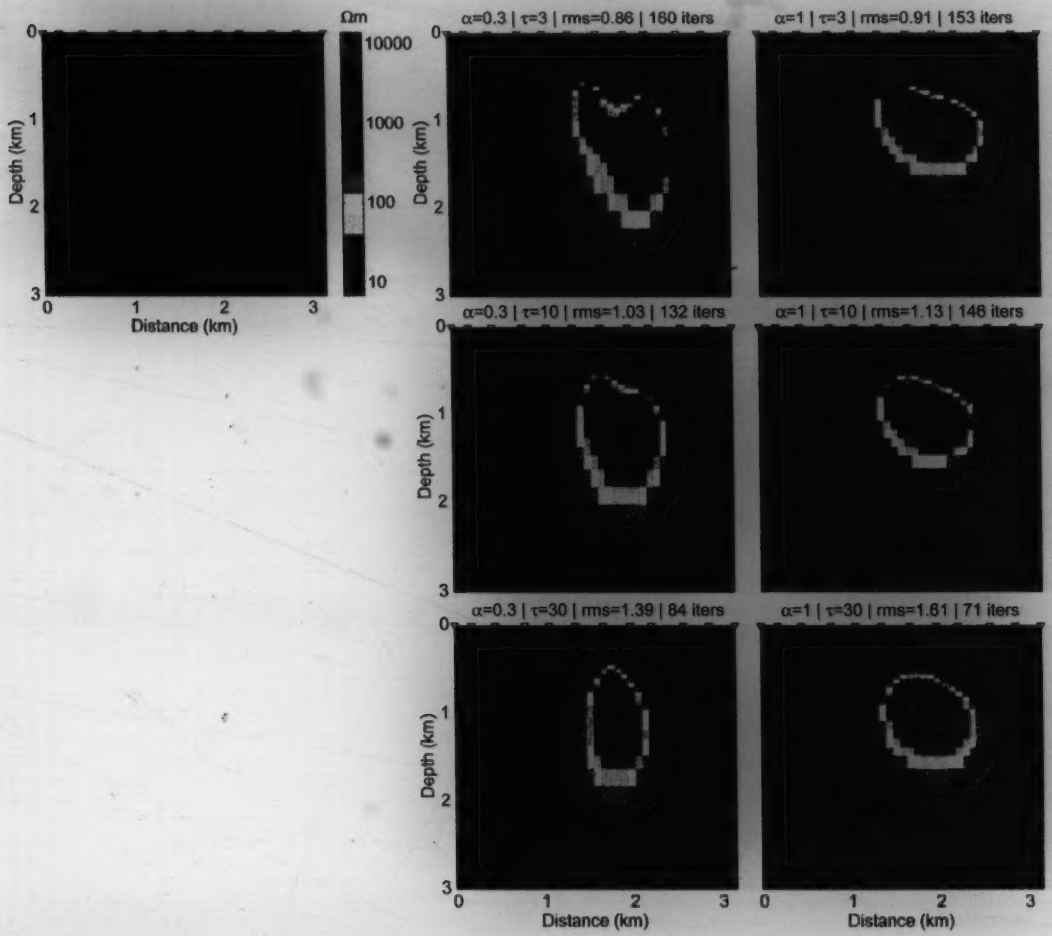
Ωm
10000
1000
100
10
Depth (km)
Distance (km)
α=0.3 | τ=3 | rms=0.86 | 160 iters
α=1 | τ=3 | rms=0.91 | 153 iters
α=0.3 | τ=10 | rms=1.03 | 132 iters
α=1 | τ=10 | rms=1.13 | 146 iters
α=0.3 | τ=30 | rms=1.39 | 84 iters
α=1 | τ=30 | rms=1.61 | 71 iters

Figure 7-3. Synthetic model of two parallel dipping basement conductors. The choice of α and τ, the smoothing parameters, of this synthetic model is same as in Figure 7-2.

The motivation for the final model considered came from other geophysical studies at the McArthur River mine. Seismic and gravity data suggested a stair like geometry for the P2 Fault of McArthur River as shown in Figure 7-5 (Claire O'Dowd, personal communication, 2006, Wood and Thomas, 2007). The inversion model in Figure 7-5 shows the greatest similarity to the true inversions but the agreement is not ideal.

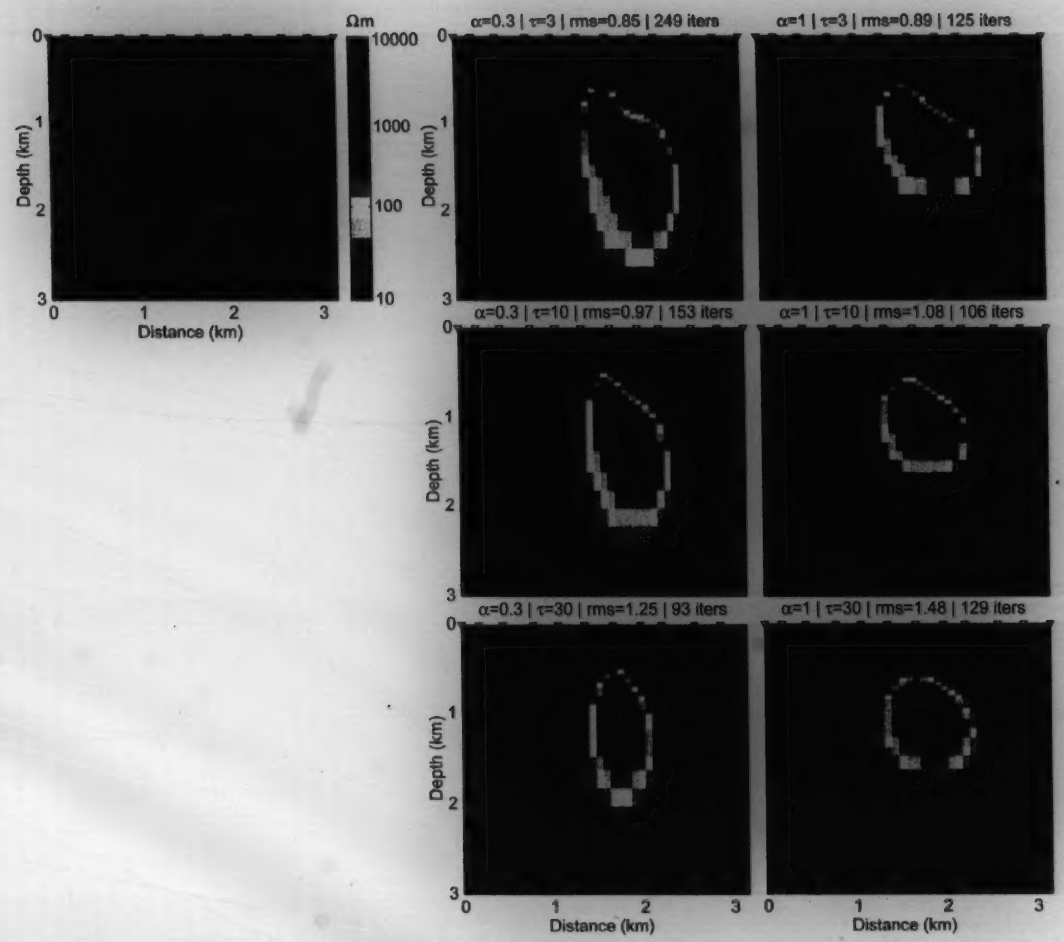
Ωm
10000
1000
100
10
Depth (km)
Distance (km)
α=0.3 | τ=3 | rms=0.85 | 249 iters
α=1 | τ=3 | rms=0.89 | 125 iters
α=0.3 | τ=10 | rms=0.97 | 153 iters
α=1 | τ=10 | rms=1.08 | 106 iters
α=0.3 | τ=30 | rms=1.25 | 93 iters
α=1 | τ=30 | rms=1.48 | 129 iters

Figure 7-4. Synthetic model of two crossing basement conductors. Note that the choice of α and τ parameters in this figure is same as in Figure 7-2.

In summary, none of the synthetic inversion models gave an adequate reproduction of the model obtained by inversion of the measured AMT data. They all differ from the model shown in Figure 6-1. Therefore, it can be concluded that while AMT exploration is good at detecting the top of the conductor, it is not very sensitive to the geometries of the basement conductors. However, a careful modelling study can give further information about the subsurface geometry. Note that many rough synthetic models may give the same inversion model (non-uniqueness problem). Thus, special care and patience are needed to define the subsurface geometry with AMT modelling. However, these synthetic inversions are a very effective way to decide which smoothing parameter is best for certain geological features.

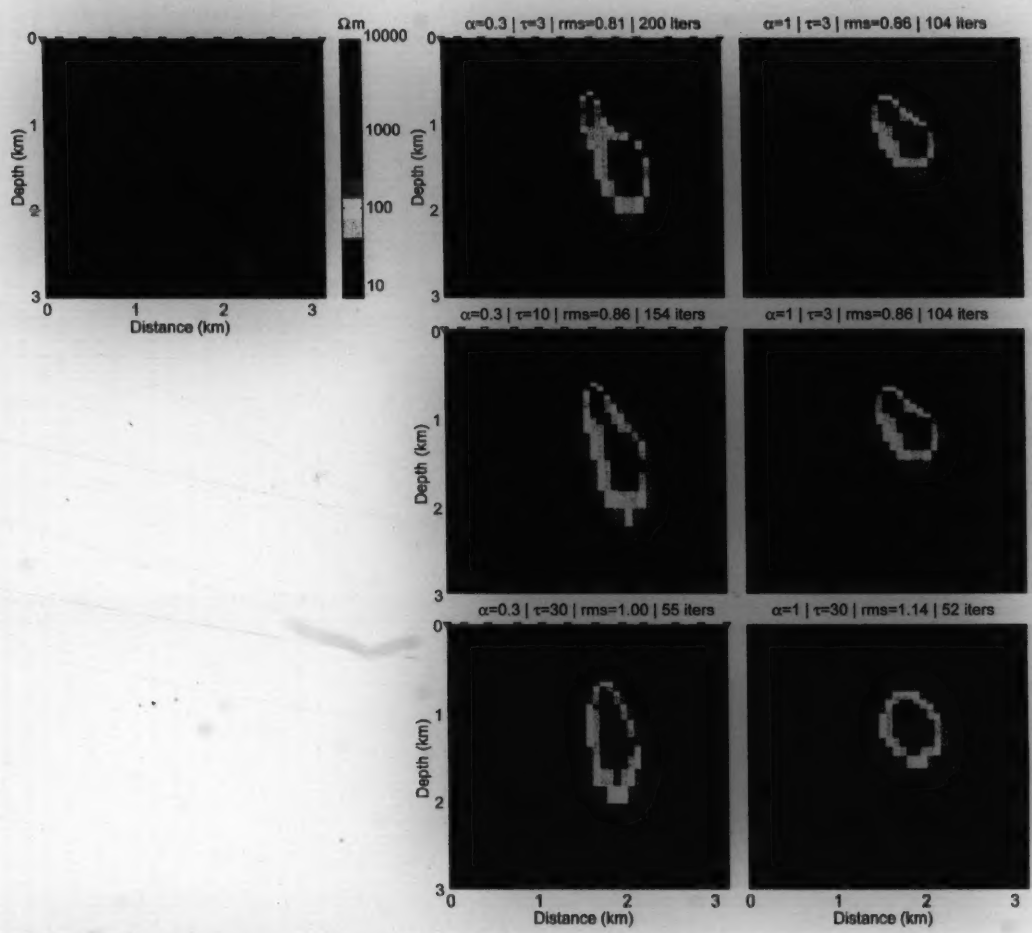
Ωm
10000
1000
100
10
α=0.3 | τ=3 | rms=0.81 | 200 iters
α=1 | τ=3 | rms=0.86 | 104 iters
α=0.3 | τ=10 | rms=0.86 | 154 iters
α=1 | τ=3 | rms=0.86 | 104 iters
α=0.3 | τ=30 | rms=1.00 | 55 iters
α=1 | τ=30 | rms=1.14 | 52 iters
Depth (km)
Distance (km)

Figure 7-5. Synthetic model of stair-like fault geometry. Note that the choice of α and τ parameters in this figure is same as in Figure 7-2.

7.2. Three Dimensional Forward Modelling

Three dimensional (3D) modelling was also used to determine if the 2D inversion results are valid in a 3D environment. The algorithm of Mackie et al. (1994) was used and the parameterization was tested by comparison with 2D modelling. For the comparison, the same 2D resistivity model was created with both 2D and 3D forward algorithms. Figure 7-6 shows the predicted apparent resistivity and phase curves for station 22405n. The resistivity and phase curves in Figure 7-6 are virtually identical which suggests that both algorithms were implemented correctly. The difference between the figures is less than 1 % due to the mesh sizes. Note that number of nodes in the two meshes is same for both algorithms.

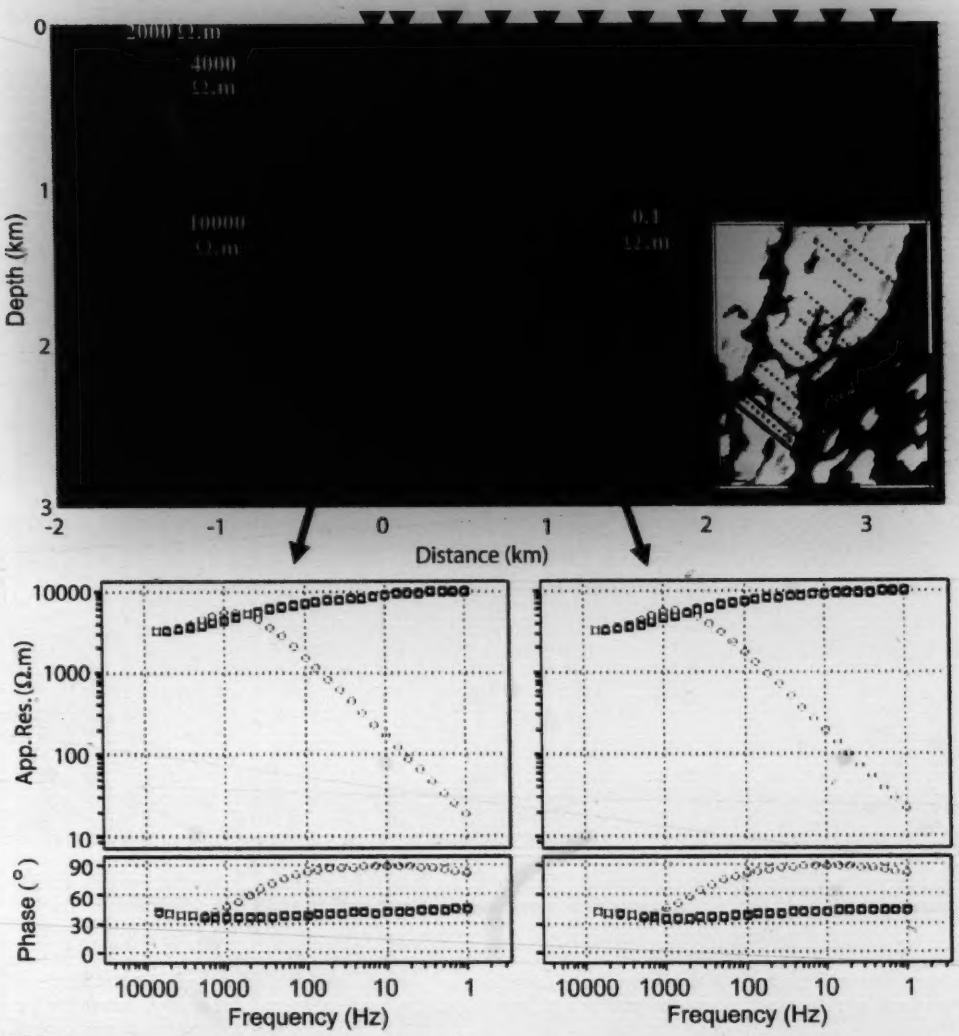

Figure 7-6. Comparison of resistivity and phase curves obtained from the 2D and 3D forward modelling algorithms. Note that both modelling programs used NLCG algorithm. Red circles show TE mode curves, blue squares show TM mode curves.

7.2.1. End effect of basement conductors

Another important question to be addressed with the 3D modelling is the end effect caused by the termination of basement conductors. The model used for this study included (1) an overburden layer (2000 Ω.m) (2) Athabasca sandstones (4000 Ω.m) and (3) underlying 10000 Ω.m metamorphic basement below the unconformity. Graphitic basement conductors (0.1 Ω.m) are present and denoted with grey shading in Figure 7-7.

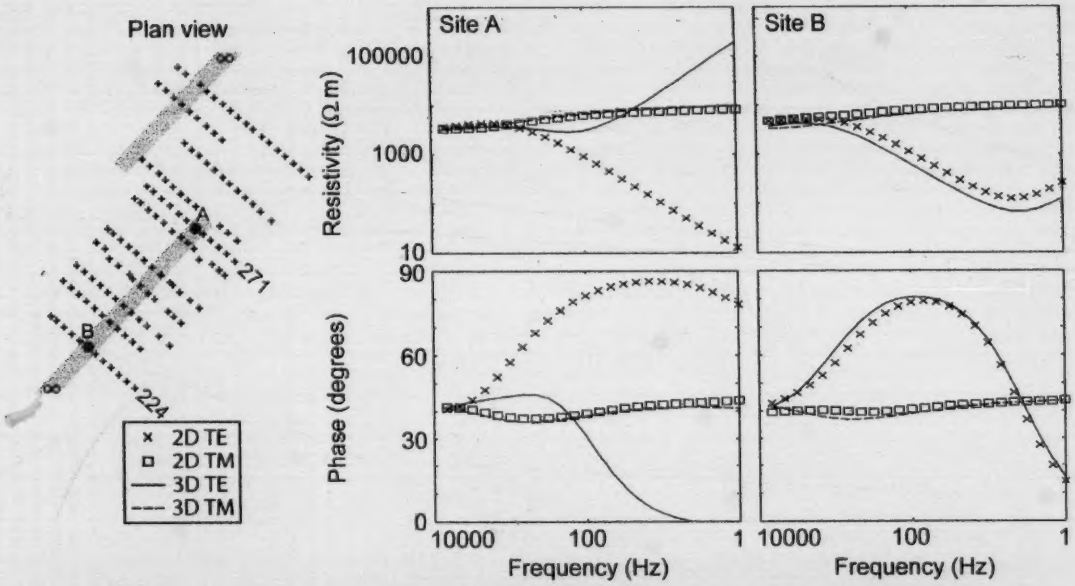

Figure 7-7. End effect in AMT data. Site A shows how the end of the conductor influences the TE mode response. The response at Site B shows that the end effect gets weaker as distance from the end of the conductor increases.

Figure 7-7 shows the apparent resistivity and phase curves at selected locations that were computed using a 3D forward calculation. The end effect is very strong in the TE mode at site A on line 271 and significantly weaker at site B on line 224. This is because the electric charges develop at the end of the conductor in the 3D model, the TE apparent resistivity is increased at low frequency, even exceeding the TM mode apparent resistivity. Simpson and Bahr (2005) indicated that 3D responses can be close to 2D responses where the galvanic effects are insignificant compared to inductive effects and inductive fields from the ends of the conductor are attenuated. They also show that the TE mode is the most influenced by these effects. Therefore, the TE mode data must be used with caution if the subsurface structure is significantly 3D (Wannamaker et al., 1984; Siripunvaraporn et al., 2005b). However, the TE mode data is very important in this type of survey because the basement conductor is essentially invisible to the TM mode. Moreover, none of the measured AMT data show the effect described above, and the TE mode apparent resistivity is always less than the TM mode at all stations (Figure 5-7). This indicates that major 3D effects are likely not present and the McArthur River AMT data and it can be considered 2D. However, if a basement conductor terminates close to the profile, then a 2D inversion may not be valid. This was shown in Figure 7-7 where the difference

between 2D and 3D forward responses was significant. However, it is believed that the basement conductors in the McArthur River area do not terminate in this fashion. This is consistent with the similarity of the 2D and 3D inversion results described in Chapter 6.

7.2.2. 2D and 3D resistivity models and induction vectors

The other problem that was encountered in the interpretation of the McArthur River AMT data set was the complexity of the induction vectors. As described in chapter 5, induction vectors plotted with the Parkinson convention, point at conductors. Thus if a conductor is perpendicular to the profile, the induction vectors should be parallel to the profile. However, this simple geometry was not observed in the measured AMT data (Figure 5-6). Thus, it was thought that these data might be significantly affected by the 3D structures. This effect was investigated with 3D forward modelling to see what type of subsurface geometry might cause this effect.

For this investigation, a number of 2D and 3D model responses were computed with the 3D forward algorithm of Mackie et al. (1994) and representative responses will be shown in this study. Figure 7-8 shows the variety of 2D models because it was important to understand the 2D behaviour of the induction vectors before examining 3D effects. All models have two parallel basement conductors. However, at the top two models, the basement consists of two different domains which may represent the Wollaston and Mudjatik domains. The key difference between these two models was the termination depth of the conductors. In the first model the conductors terminate at a depth of 3 km while the conductors in the second model extend to infinite depth. This difference does not cause any difference in the computed induction vectors. Also excluding the Mudjatik domain from the model (third model) does not cause any change either. Moreover, all the induction vectors are parallel to the profiles and do not demonstrate any deviation. Therefore, it is verified that 2D models show parallel induction vectors which point towards the conductor. This result was expected in a 2D model and confirms that the 3D AMT modelling has been correctly implemented.

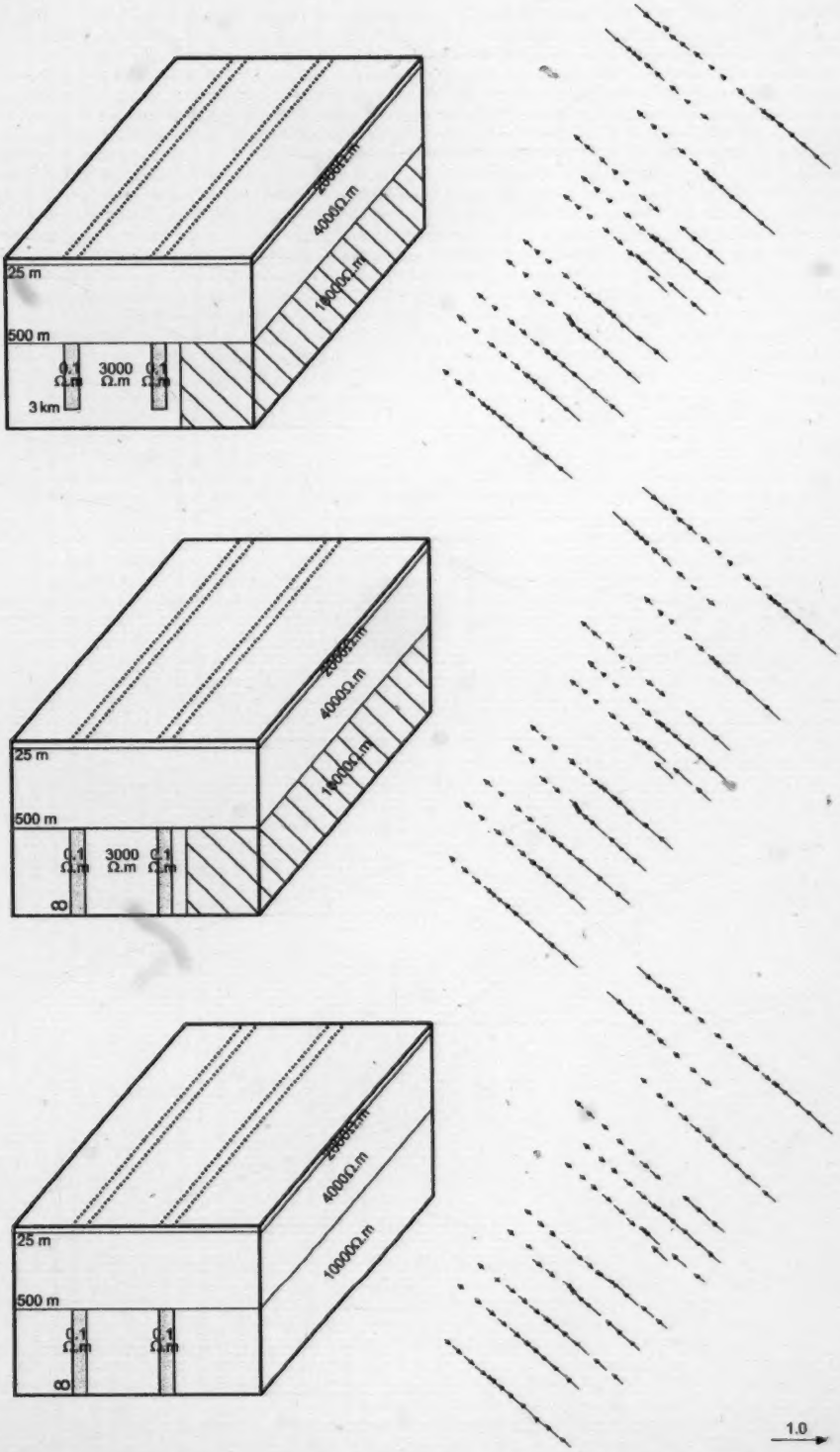

Figure 7-8. 2D models computed by 3D forward algorithm to test the 2D behaviours of the induction vectors.

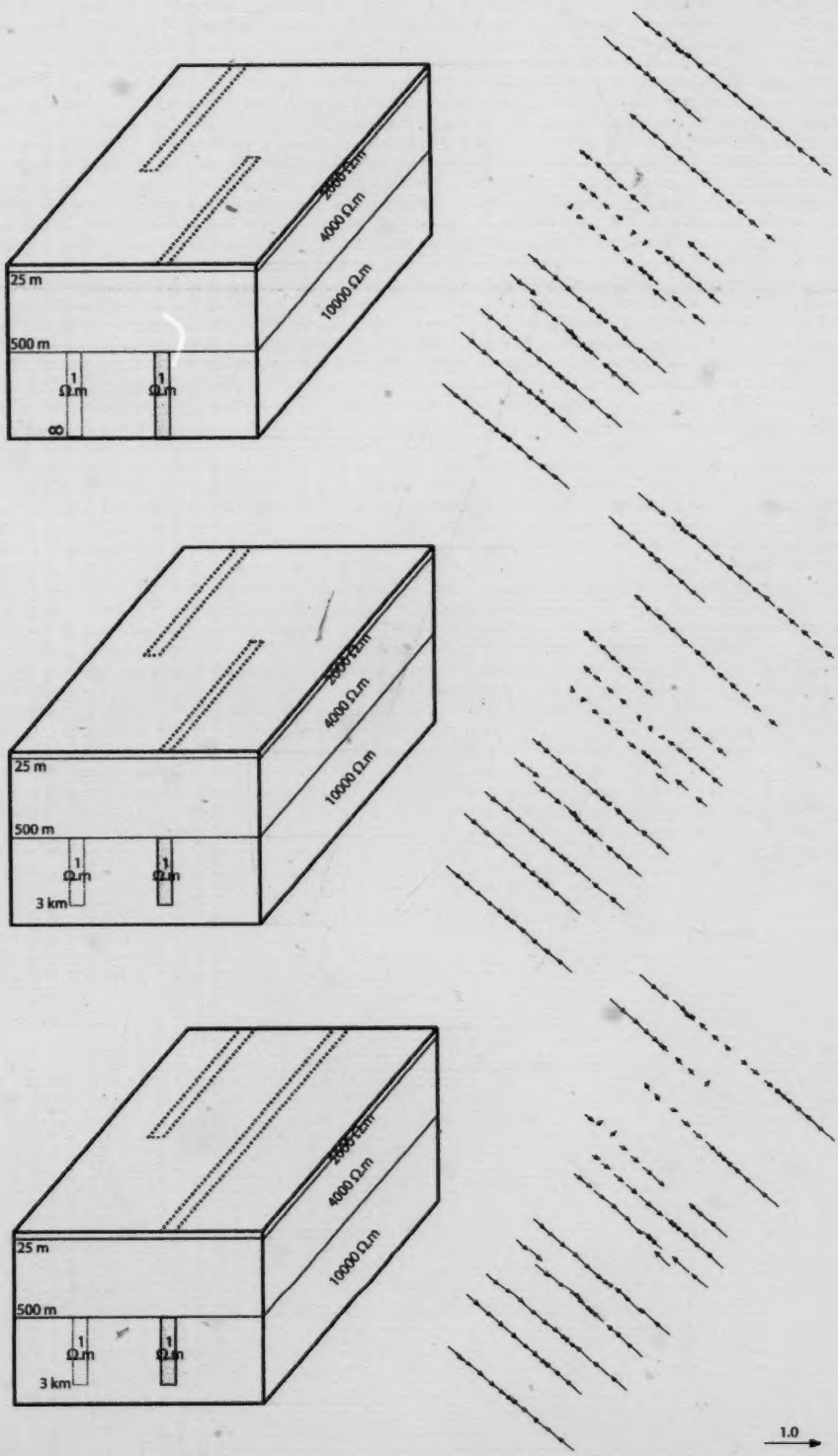

Figure 7-9. 3D models used to model the measured induction vectors.

It is possible that effects of the ends of basement structures might cause the observed deviations of the induction vectors. This was tested with the three dimensional models shown in Figure 7-9. In the top two models, both conductors terminate at the center of the AMT survey area. In the first model the conductors extend to infinite depth while in the second model they terminate at a depth of 3 km. Only small changes in the induction vectors were observed close to the end of the conductors. However the pattern was not as strong as that observed in the measured AMT data. Measured data induction vectors were more distorted by complex structures compared to these three dimensional models. Thus, the third model included both two dimensional and three dimensional conductors. In the third model, the eastern conductor was continuous (2D) and the western one terminated in the middle of the model. The effect was stronger compared to the other two but it was not strong enough to reproduce the observed pattern. None of these three 3D models can display the observed deviation, which suggests a more complex geometry for the McArthur River area than included in the synthetic models.

The study above showed that two parallel basement conductors could not create the observed induction vector patterns. Therefore, an alternative hypothesis was to consider a series of intersecting conductors (Figure 7-10). In the first model, the location of the crossing conductor was in the middle of the survey area. This generated the observed induction vector pattern on the southern profiles (224 – 254). However, on the northern profiles, the induction vectors point south, which was not observed in the field data (Figure 5-6). This indicated that there may not be an across-strike conductor beneath the audio-magnetotelluric survey area, but there could be one to the north of the survey area. This is because there is no induction vector pointing south in the measured McArthur River audio-magnetotelluric data. The second model in Figure 7-10 was generated to test this hypothesis. This model gave the best agreement with the measured induction vectors. Thus, it can be postulated that there might be one basement conductor at the northern side of the McArthur River mine site striking East or Northeast. McGill et al. (1993) and Ruzicka (1996) suggested Northeastern and Eastern striking faults in the area which supports this hypothesis.

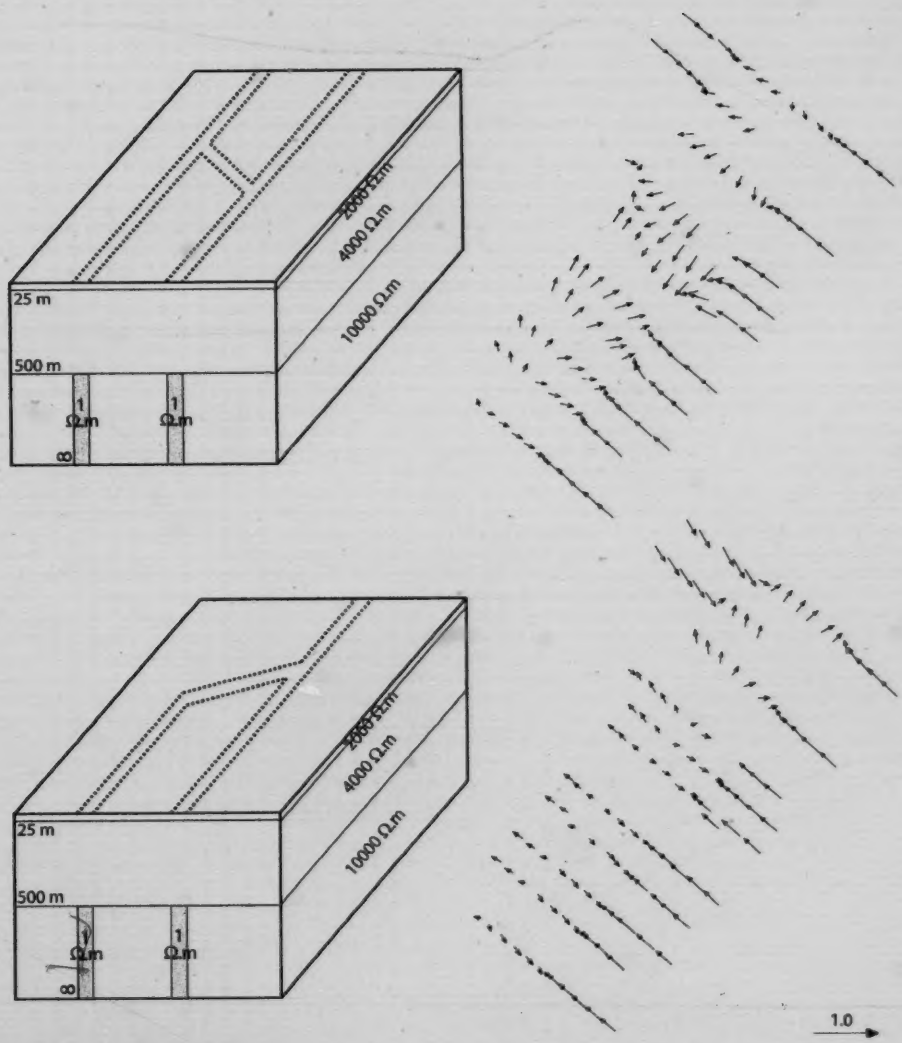

Figure 7-10. 3D models that includes crossing conductors to model the measured induction vectors.

7.2.3. Tensor decomposition of the 3D models

Tensor decomposition is another effective way to determine if a 2D interpretation of an AMT data set is valid. Figure 7-11 shows the results of tensor decomposition for the synthetically generated AMT data from the 3D model shown previously in Figure 7-9. A strike direction parallel to the basement conductors was determined for stations far from the end of the conductors, although a more complex pattern was observed close to the ends. Note that the degree of scatter in the synthetic strike directions is quite similar to the observed data (Figure 7-11).

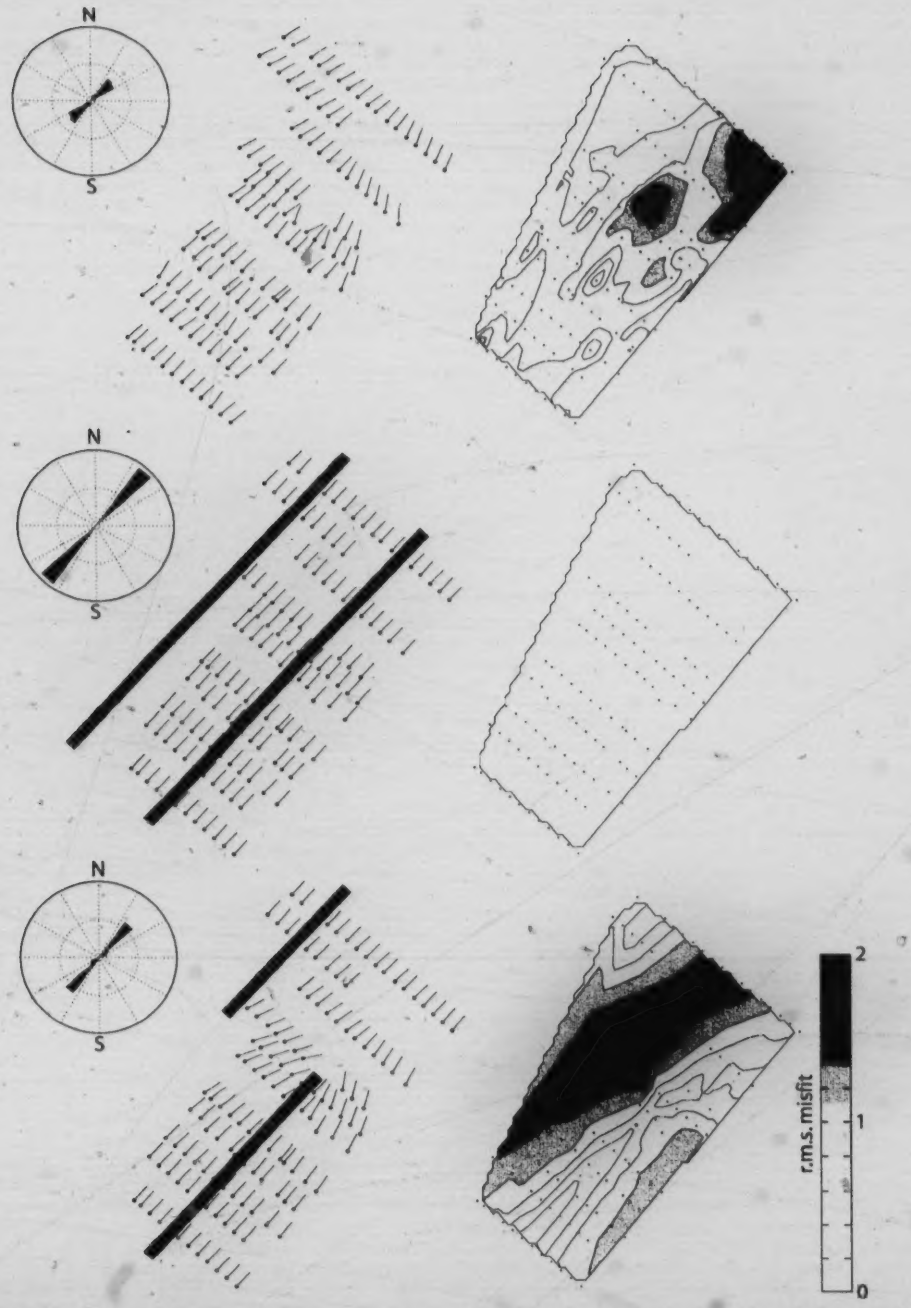

Figure 7-11. Results of tensor decomposition for measured data and synthetic 3D model over a frequency range 1 – 1000 Hz. (a) Shows best fitting strike direction in map format and the misfit obtained by the tensor decomposition. Low misfit values indicate the 2D assumption is well satisfied. (b) Same quantities for synthetic data generated for a 2D resistivity model. (c) Same quantities for synthetic data generated for a 3D resistivity model. Red rectangular bars shows the locations of conductors in the synthetic models.

Figure 7-11 also shows a map of r.m.s. misfit values obtained from the tensor decomposition. Note that misfit values for the 3D synthetic model were significantly higher than the misfit values obtained from the field data. This indicates two dimensionality in the survey area. The r.m.s. misfit maps thus represent a more reliable test than the strike diagrams to determine if the field AMT data can be considered 2D.

7.3. Discussion

2D synthetic inversion and the 3D forward modelling were an effective way to test the resolution and stability of the inversion models. Many hypotheses were tested with these techniques and useful information was obtained. The first investigation with 2D synthetic inversions was to test how deep the AMT data set can image the conductor. It was found that it was possible to reliably image to a depth of 2 km and with increased ambiguity to 3 km depth. It is also possible to image structures below 3 km using lower frequencies. However, these lower frequencies cannot generally be recorded with AMT systems and would require broadband MT systems. In addition, AMT data can delineate the desilicified alteration zones if they are present through their low resistivity. However, the synthetic study showed that AMT data are not very sensitive to silicified (resistive) alteration zones since they can be confused with artefacts in the model. Synthetic inversions suggested that the resistive halo which was thought as the silicification above the conductor might be the artefact of the inversion scheme. This was because the models that did not include silicification zones showed the same resistive halo through smoothing as those that contained a halo.

3D forward modelling studies also indicated that the McArthur River AMT data set does not exhibit major 3D induction or galvanic effects. The impedances and induction vectors were mostly 2D on the profiles but there could be some 3D effects to the north of the survey area. A range of 2D and 3D resistivity models with parallel conductors showed parallel induction vectors aligned in the east west direction in contrast to the well defined geoelectric strike directions results. However, further studies showed that the crossing conductors outside the survey area might be the reason for the observed deviation of the measured data induction vector's behaviour.

Finally, the r.m.s. maps of the decomposition of the AMT data was used to understand the dimensionality in the area. It was shown that even the simple 3D models with parallel conductors showed higher r.m.s. misfit values than the measured AMT data. This indicates that the subsurface structures can be considered relatively 2D in the study area.

8. CONCLUSIONS

This thesis has described a rigorous evaluation of AMT as a tool for deep uranium exploration in environments such as the Athabasca Basin. The resistivity image in Figure 8-1 shows the main sub-surface features that can be imaged with AMT exploration. The P2 fault has a very low resistivity owing to the presence of graphite, dips southeast and terminates upward at the depth of the unconformity. Synthetic studies showed that basement conductors could be detected by AMT in locations where the unconformity is at a depth of 2-3 km. This is a significant advantage over the maximum exploration depth of ~ 900 m that can be achieved with existing EM methods such as MEGATEM, VTEM, UTEM and DEEPEM.

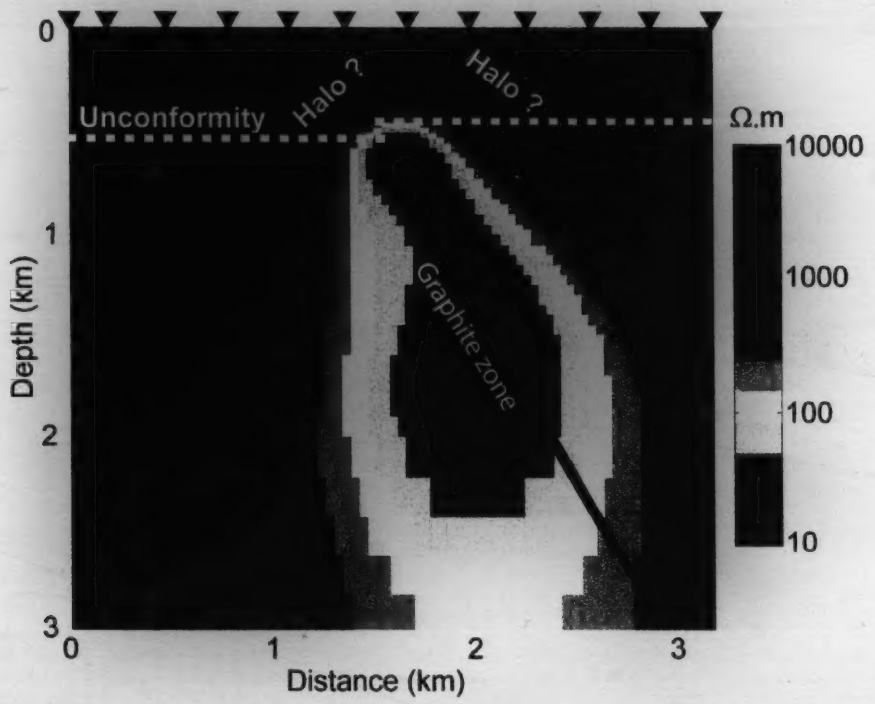

Figure 8-1. Resistivity model derived from the 2D inversion of the TE-TM-T_{zy} data on profile 224 (Figure is modified from Tuncer et al., 2006a).

The resistivity model shows a resistive halo above the uranium deposit. This feature could have been the result of silicification caused by hydrothermal flow during mineralization. However resolution tests (Chapter 7) showed that this feature could be an artefact of the smoothing scheme used by the inversion algorithm. However, a 1D analysis of the data by Craven et al., (2007) showed that AMT is inherently sensitive to such features. However, in 2D the huge resistivity contrast between the graphite in the faults and rocks above and below the unconformity masks this subtle feature. The uranium ore bodies were not imaged directly because of their small size. Although the uranium ore bodies have lower resistivity values than the surrounding rocks (i.e. sandstones and basement rocks), the presence of graphite overshadows this contrast since the conductance of the graphitic fault is much larger. Typical resistivities of rocks encountered in this area are listed in Figure 1-3.

In the type of subsurface geometry encountered at the McArthur River mine, the 2D inversion appears to recover subsurface resistivity reliably, and a full 3D inversion may not always be needed. Tensor decomposition and resistivity models derived from 3D AMT inversions also support this hypothesis. The 3D inversion results generally showed good agreement with the 2D inversion results. The only difference was the presence of a conductive zone at the northeast part of the study area below the unconformity.

Vertical magnetic fields were recorded in this AMT survey and are displayed as induction vectors. In most parts of the survey area, the induction vectors indicate a 2D subsurface resistivity structure and these data were very useful in understanding the dimensionality of the subsurface. The vertical magnetic fields were also useful in constraining the 2D and 3D AMT inversions. However, this study has shown that vertical magnetic field data should be used with caution in a 2D inversion when there are indications that the subsurface structure is 3D. In this case, 3D inversions and modelling are necessary to validate the 2D inversions. Vertical magnetic fields should be routinely recorded in AMT surveys.

In summary, AMT exploration can image the graphitic conductors with high resolution to depths of 2–3 km depth using frequencies of 10000-10 Hz. AMT exploration can also image the zones of alteration that may indicate the presence of uranium mineralization, and which are important exploration targets. The geometry of the subsurface structure can be also modelled with the aid of

other geophysical methods and borehole data and permit improved constraints on subsurface structure. For example, (1) information about unconformity depth and fault geometry can be derived from seismic data, (2) boundaries of the different geological domains can be obtained from magnetic data and (3) the geometry and type of alteration zones can be derived from well log data. Each of these pieces of information can enhance the information that can be derived from AMT exploration.

There could be value in additional AMT research at the McArthur River mine. Additional AMT profiles could be used to extend spatial coverage and determine the pattern of regional basement conductors. This would enhance resolution in the vicinity of the mine. AMT profiles with closer station spacing would also be useful in the vicinity of the mine and might delineate more subtle features above the unconformity. Finally, studies of other uranium prospects would be very useful to determine if the features observed at McArthur River are typical of most unconformity uranium deposits. This would allow the role of AMT in future exploration to be further evaluated.

REFERENCES

Alexandre P., K. Kyser, D. Thomas, P. Polito and J. Marlat, 2007. Geochronology of unconformity-related uranium deposits in the Athabasca Basin, Saskatchewan, Canada and their integration in the evolution of the basin. *Miner Deposita,* DOI 10.1007/s00126-007-0153-3.

Andrade, N., 2002. Geology of the Cigar Lake uranium deposit; in Andrade, N., Breton, G., Jefferson, C.W., Thomas, D.J. Tourigny, G., Wilson, W., and Yeo, G.M., eds., The Eastern Athabasca Basin and its uranium deposits, Field Trip A-1 Guidebook: Geological Association of Canada and Mineralogical Association of Canada, Saskatoon, May 24-26, 2002, p. 53-72.

Annesley, I. R. and C. Madore, 1993. Laboratory measurements of magnetic susceptibility and density from lithological units of the Wollaston Domain, Saskatchewan; Saskatchewan Research Council, Publication R-1230-11-C-93, 21p.

Berdichevsky M. N., V. I. Dmitriev and E. E. Pozdnjakova, 1998. On two-dimensional interpretation of magnetotelluric soundings. *Geophysical Journal International*, **133,** 585 – 606.

Bernier, S., 2004. Stratigraphy of the Late Paleoproterozoic Manitou Falls Formation, in the vicinity of the McArthur River Uranium Deposit, Athabasca Basin, Saskatchewan, Canada; unpublished M.Sc. thesis: Laurentian University, 184 p.

Bruneton, P., 1993. Geological environment of the Cigar Lake uranium deposit, *Canadian Journal of Earth Sciences*, **30**, p. 653-673.

Cagniard, L., 1953. Basic theory of the magneto-telluric method of geophysical prospecting. *Geophysics,* **18**, 605 – 635.

Campbell, J. E., Shieves, R. B. K. and Klassen R. A., 2002. Integrated field investigations of airborne radiometric spectral domains, NEA-IAEA test area, eastern Athabasca Basin: A preliminary report, *Summary of Investigations 2002,* **v2**, *Saskatchewan Geological Survey, Saskatchewan Industry Resources, Miscellaneous Report 2002-4.2*, Paper D-2.

Card, C. D., D. Pana, R. A. Stern and N. Rayner, 2007. New insights into the geological history of the basement rocks to the southern Athabasca Basin, Saskatchewan and Alberta, in Jefferson, C.W., and Delaney, G., eds., EXTECH IV: Geology and Uranium EXploration TECHnology of the

Proterozoic Athabasca Basin, Saskatchewan and Alberta: Geological Survey of Canada, Bulletin **588** (also Saskatchewan Geological Society, Special Publication 18; Geological Association of Canada, Mineral Deposits Division, Special Publication 4).

Clarke, J., T. D. Gamble, W. M. Goubau, R. H. Koch, R. F. Miracky, 1983. Remote-reference magnetotellurics: Equipment and procedures, *Geophysical Prospecting*, **31**, (1), 149 – 170.

Constable S. C., R. L. Parker and C. G. Constable, 1987. Occam's inversion: a practical algorithm for generating smooth models from electromagnetic sounding data. *Geophysics,* **52**, 289 – 300.

Craven, J. A., G. McNeice, G. Wood, B. Powell, R. Koch, I. R. Annesley, and C. J. Mwenifumbo, 2002. EXTEXCH IV Sub-project 9T; A 3D Audio-Magnetotelluric survey at the McArthur River mining camp in summary of investigations 2002, *Saskatchewan Geological Survey Sask. Energy Mines, Misc. Rep.*

Craven, J. A., G. McNeice, B. Powell, R. Koch, I. R. Annesley, G. Wood, C. J. Mwenifumbo, M. Unsworth and W. Xiao, 2007. Audio-magnetotelluric studies at the McArthur River mining camp and Shea Creek area, northern Saskatchewan, in Jefferson, C.W., and Delaney, G., eds., EXTECH IV: Geology and Uranium EXploration TECHnology of the Proterozoic Athabasca Basin, Saskatchewan and Alberta: Geological Survey of Canada, Bulletin **588** (also Saskatchewan Geological Society, Special Publication 17; Geological Association of Canada, Mineral Deposits Division, Special Publication 4).

Craven, J. A., C. G. Farquharson, R. L. Mackie, W. Siripunvaraporn, V. Tuncer and M. J. Unsworth, 2006. A comparison of two- and three-dimensional modelling of audiomagnetotelluric data collected at the world's richest uranium mine, Saskatchewan, Canada, 18th International Workshop on Electromagnetic Induction in the Earth, El Vendrell, Spain.

Creaser, R. A. and L. Stasiuk, 2005. Depositional age of the Douglas Formation, northern Saskatchewan, determined by Re-Os geochronology; in Jefferson, C.W., and Delaney, G., eds., EXTECH IV: Geology and Uranium EXploration TECHnology of the Proterozoic Athabasca Basin, Saskatchewan and Alberta: Geological Survey of Canada, Bulletin **588** (also Saskatchewan Geological Society, Special Publication 17; Geological Association of Canada, Mineral Deposits Division, Special Publication 4), in prep.

Cristall, J., and D. Brisbin, 2006. Geological sources of VTEM responses along the Collins Bay Fault, Athabasca Basin: Proceedings of the Giant Uranium Deposits Short Course, PDAC.

Crone, J. D., 1991. PEM case histories, Cigar and Winston Lakes, Canada, in M. N. Nabighian ed., Electromagnetic methods in Applied Geophysics, **2**,

Application, Parts A and B, Society of Exploration Geophysicists, 490 – 494.

Cumming, G. L., and D. Krstic, 1992. The age of unconformity-related uranium mineralization in the Athabasca Basin, northern Saskatchewan, *Canadian Journal of Earth Sciences,* **29**, 1623-1639.

deGroot-Hedlin C. and S. Constable, 1990. Occam's inversion to generate smooth, two-dimensional models from magnetotelluric data. *Geophysics,* **55**, 1613 – 1624.

Earle, S. and V. Sopuck, 1989. Regional lithogeochemistry of the eastern part of the Athabasca Basin uranium province, Saskatchewan; in . Muller-Kahle , E., ed.,Uranium resources and geology of North America: International Atomic Energy Agency, TECDOC-**500**, p. 263 – 269.

Egbert, G. D., 1989. Multivariate analysis of geomagnetic array data: 2. Random source models, *Journal of Geophysical Research,* **94**, 14249 – 14265.

Egbert, G. D., 1997. Robust multiple-station magnetotelluric data processing: Geophysical Journal International, **130**, 475–496.

Egbert, G. D., 2002. Processing and interpretation of electromagnetic induction array data, *Surveys in Geophysics,* **23**, 207 – 249.

Egbert, G. D., and J. R. Booker, 1986. Robust estimation of geomagnetic transfer functions, *Geophys. J. R. Astron. Soc.,* **87**, 173–194.

Egbert, G. D. and J. R. Booker, 1989. Multivariate analysis of geomagnetic array data: 1. The response space, *Journal of Geophysical Research,* **94**, 14227 – 14247.

Egbert, G. D. and J. R. Booker, 1993. Imaging crustal structure in southwestern Waschington with small magnetometer arrays, *Journal of Geophysical Research,* **98**, 15967 – 15985.

Fayek, M., T. M. Harrison, R. C. Ewing, M. Grove and C. D. Coath, 2002a. O and Pb isotope analyses of uranium minerals by ion microprobe and U-Pb ages from the Cigar Lake deposit, *Chemical Geology*, **185**, p. 205- 225.

Gamble, T. D., W. M. Goubau and J. Clarke, 1979. Magnetotellurics with a remote magnetic reference, *Geophysics,* **44**, 53 – 68.

Goubau, W. M., T. D. Gamble and J. Clarke, 1978. Magnetotelluric data analysis: removal of bias, *Geophysics,* **43**, 1157 – 1166.

Groom R. W. and R. C. Bailey, 1989. Decomposition of magnetotelluric impedance tensors in the presence of local three-dimensional galvanic distortion. *Journal of Geophysical Research,* **94**, 1913 – 1925.

Györfi, I., Z. Hajnal, S. Bernier, E. Takacs, B. Reilkoff, D. White, B. Powell and R. Koch, 2002. Initial seismic images along line 14 of the McArthur River high-resolution survey; *in Summary of Investigations, 2002, Volume*

2; Saskatchewan Geological Survey, Saskatchewan Industry and Resources, Miscellaneous Report 2002 – 4.2 (CD-ROM).

Györfi, I., Z. Hajnal, D. J. White and B. Roberts, 2004. High-resolution 2D and 3D seismic imaging of structurally complex hardrock environments hosting high-grade uranium ore, Athabasca Basin, Canada, SEG/Denver 74th Annual Meeting.

Györfi, I., Z. Hajnal, D. J. White, E. Takacs, B. Reilkoff, I. R. Annesley, B. Powell and R. Koch, 2007. High-resolution seismic survey from the McArthur River region: contributions to mapping the complex P2 uranium ore zone, Athabasca Basin, Saskatchewan; in Jefferson, C.W., and Delaney, G., eds., EXTECH IV: Geology and Uranium EXploration TECHnology of the Proterozoic Athabasca Basin, Saskatchewan and Alberta: Geological Survey of Canada, Bulletin **588** (also Saskatchewan Geological Society, Special Publication 17; Geological Association of Canada, Mineral Deposits Division, Special Publication 4).

Hajnal, Z., E. Takacs, D. J. White, I. Györfi, B. Powell B. and R. Koch, 2007. Regional seismic signature of the basement and crust beneath the McArthur River mine district, Atabasca Basin, Saskatchewan; in Jefferson, C.W., and Delaney, G., eds., EXTECH IV: Geology and Uranium EXploration TECHnology of the Proterozoic Athabasca Basin, Saskatchewan and Alberta: Geological Survey of Canada, Bulletin **588** (also Saskatchewan Geological Society, Special Publication 17; Geological Association of Canada, Mineral Deposits Division, Special Publication 4).

Hoeve, J. and D. H. Quirt, 1984. Mineralization and host rock alteration in relation to clay mineral diagenesis and evolution of the Middle–Proterozoic Athabasca Basin, northern Saskatchewan, Canada, Saskatchewan Research Council, SRC Technical Report **187**, 187 p.

Hoeve, J., and D. H. Quirt, 1987. Astationary redox front as a critical factor in the formation of high-grade, unconformity-type uranium ores in the Athabasca basin, Saskatchewan, Canada: *Bulletin de Minéralogie*, **110**, 157 – 171.

Irvine, R. and K. Witherly, 2006. Advances in airborne EM acquisition and processing for uranium exploration in the Athabasca Basin, Canada, *SEG/New Orleans 76th Annual Meeting.*

Jacob, J. A., Y. Kato, S. Matsuhita and V. A. Troitskaya, 1964. Classification of geomagnetic pulsation, *Journal of Geophysical Research*, **69**, v1, 180 - 181.

Jefferson, C. W., G. Delaney and R. A. Olson, 2003. EXTECH IV Athabasca uranium multidisciplinary study of northern Saskatchewan and Alberta, Part 1 overview and impact, Geological Survey of Canada Current Research, 2003 - C18.

Jefferson, C. W., D. J. Thomas, S. S. Gandhi, P. Ramaekers, G. Delaney, D. Brisbin, C. Cutts, P. Portella and R. A. Olson, 2007. Unconformity associated uranium deposits, in Jefferson, C.W., and Delaney, G., eds., EXTECH IV: Geology and Uranium EXploration TECHnology of the Proterozoic Athabasca Basin, Saskatchewan and Alberta: Geological Survey of Canada, Bulletin **588** (also Saskatchewan Geological Society, Special Publication 18; Geological Association of Canada, Mineral Deposits Division, Special Publication 4).

Jones, A. G., 1988. Static shift of magnetotelluric data and its removal in a sedimentary basin environment, *Geophysics*, **53**, 967 – 978.

Jones, A. G. and G. McNeice, 2002. Audio-magnetotellurics (AMT) for steeply-dipping mineral targets: importance of multi-component measurements at each site, *SEG/Salt Lake City 72nd Annual Meeting.*

Jones, A. G. and X. Garcia, 2003. Okak Bay AMT data-set case study: Lessons in dimensionality and scale, *Geophysics*, **68**, 70-91.

Kister, P., E. Laverret, M. Cuney, P. Vieillard, and D. Quirt, 2003. 3D distribution of alteration minerals associated with unconformity-type mineralization: Anne Zone, Shea Creek deposit (Saskatchewan, Canada); in Cuney, M., ed., Uranium Geochemistry 2003, International Conference, April 13-16 2003, Proceedings: Unité Mixte de Recherche CNRS 7566 G2R, Université Henri Poincaré, Nancy, France, 197 – 200.

Lakanen, E., 1986. Scalar audio-magnetotellurics applied to base - metal exploration in Finland, *Geophysics*, **51**, (8) 1628 – 1646.

Larsen, J., R. L. Mackie, A. Manzella, A. Fiordelisi and S. Rieven, 1996. Robust smooth magnetotelluric transfer functions, *Geophysical Journal International*, **124**, 801 – 819.

Leppin, M. and D. Goldak, 2005. Mapping deep sandstone alteration and basement conductors utilizing audiomagnetotellurics: exploration for uranium in the Virgin River area, Athabasca Basin, Saskatchewan, Canada, *SEG/Houston 75th Annual Meeting EM 3.7.*

Lezaeta, P. and V. Haak, 2003. Beyond magnetotelluric decomposition: Induction, current channelling and magnetotelluric phases over 90°. *Journal of Geophysical Research,* **108**, EPM 4, 1 – 20.

L'Heureux, E., B. Milkereit and E. Adam, 2005. 3D seismic exploration for mineral deposits in hardrock environments. *CSEG Recorder,* 36 – 39.

Long, D. G .F., 2007. Topographic influences on the sedimentology of the Manitou Falls Formation, eastern Athabasca Basin, Saskatchewan; in Jefferson, C.W., and Delaney, G., eds., EXTECH IV: Geology and Uranium EXploration TECHnology of the Proterozoic Athabasca Basin, Saskatchewan and Alberta: Geological Survey of Canada, Bulletin **588** (also Saskatchewan Geological Society, Special Publication 18;

Geological Association of Canada, Mineral Deposits Division, Special Publication 4).

Mackie, R. L. and T. R. Madden, 1993. Three-dimensional magnetotelluric inversion using conjugate gradients. *Geophysical Journal International,* **115**, 215 – 219.

Mackie, R. L., J. T. Smith and T. R. Madden, 1994. Three-dimensional electromagnetic modelling using finite difference equations: The magnetotelluric example, *Radio Science*, **29**, 923 – 935.

Mackie, R. L., W. Rodi and M. D. Watts, 2001. 3-D magnetotelluric inversion for resource exploration: Extended Abstracts, SEG/San Antonio 75th Annual Meeting.

Matthews, R., R. Koch and M. Leppin, 1997. Advances in integrated exploration for unconformity uranium deposits in western Canada, in *Proceedings of Exploration 97: Fourth Decennial International Conference on Mineral Exploration*, edited by A. G. Gubins, 1997, 993 – 1024.

Maurice, Y. T., W. Dyck, and J. G. Strnad, 1985. Secondary dispersion around the uranium-nickel deposit at Key Lake, northern Saskatchewan; in T.I. Sibbald and W. Petruk, eds., Geology of Uranium Deposits: *Canadian Institute of Mining and Metallurgy*, Special Volume **32**, 38 – 47.

McGill, B., J. Marlatt, R. Matthews, V. Sopuck, L. Homeniuk and J. Hubregtse, 1993. The P2 North uranium deposit Saskatchewan, Canada. *Exploration and Mining Geology*, **2**, (4), 321 – 331.

McMullan, S. R., R. B. Matthews and P. Robertshaw, 1987. Exploration geophysics for Athabasca uranium deposits: Exploration '87 Proceedings, Ontario Geological Survey, Geophysical Methods: Their application to ore exploration, *3,* 547 – 566.

McNiece, G. M. and A. G. Jones, 2001. Multisite, multifrequency tensor decomposition of magnetotelluric data. *Geophysics,* **66**, 158 – 173.

Milkereit, B., E. K. Berrer, A. R. King, A. H. Watts, B. Roberts, E. Adam, D. W. Eaton, J. Wu and M. H. Salisbury, 2000. Development of 3D seismic exploration technology for deep Nickel-Copper deposits – A case history from the Sudbury Basin, Canada. *Geophysics,* **65**, 1890-1899.

Milsom, J., 1989. Field Geophysics, John Wiley & Sons, New York.

Mwenifumbo, C. J., B. E. Elliott, C. W. Jefferson, G. R. Bernius and K. A. Pflug, 2004. Physical rock properties from the Athabasca Group: designing geophysical exploration models for unconformity uranium deposits, *Journal of Applied Geophysics*, **55**, 117-135.

Mwenifumbo, C. J., J. B. Percival, G. Bernius, B. Elliott, C. W. Jefferson, K. Wasyliuk and G. Drever, 2007. Comparison of geophysical, mineralogical and stratigraphic attributes in drill holes MAC 218 and RL 88, McArthur River uranium camp, Athabasca Basin, Saskatchewan; in Jefferson, C.W.,

and Delaney, G., eds., EXTECH IV: Geology and Uranium EXploration TECHnology of the Proterozoic Athabasca Basin, Saskatchewan and Alberta: Geological Survey of Canada, Bulletin **588** (also Saskatchewan Geological Society, Special Publication 17; Geological Association of Canada, Mineral Deposits Division, Special Publication 4), in prep.

O'Dowd C. R., G. Wood, D. Brisbin and B. Powell, 2006. Enhancing uranium exploration through seismic methods and potential field modelling at the McArthur River mine site, Saskatchewan, Canada, SEG/New Orleans 76th Annual Meeting.

Oldenburg, D. W., 1990. Inversion of electromagnetic data; an overview of new techniques, *Surveys in Geophysics*, **11**, 231-270.

Parkinson, W. D., 1959. Directions of rapid geomagnetic variations, *Geophysical Journal of the Royal Astronomical Society*, **2**, 1 – 14.

Parkinson, W. D., 1962. The influence of continents and oceans on geomagnetic variations, *Geophysical Journal of the Royal Astronomical Society*, **6**, 441 – 449.

Queralt P., A. G. Jones and J. Ledo, 2007. Electromagnetic imaging of a complex ore body: 3D forward modeling,sensitivity tests, and down-mine measurements, *Geophysics*, **72**, (2) F85 – F95.

Rainbird, R. H., R. A. Stern, N. Rayner and C. W. Jefferson, 2006. Ar – Ar and U - Pb geochronology of a Late Paleoproterozoic roft basin: support for a genetic link with Hudsonian orogenesis, western Churchill Province, Nunavut, Canada. *The Journal of Geology*, **114**, 1 – 17.

Rainbird, R. H., R. A. Stern, N. Rayner and C. W. Jefferson, 2007. Age, provenance, and regional correlation of the Athabasca Group, Saskatchewan and Alberta, constrained by igneous and detrital zircon geochronology; in Jefferson, C.W., and Delaney, G., eds., EXTECH IV: Geology and Uranium EXploration TECHnology of the Proterozoic Athabasca Basin, Saskatchewan and Alberta: Geological Survey of Canada, Bulletin **588** (also Saskatchewan Geological Society, Special Publication 18; Geological Association of Canada, Mineral Deposits Division, Special Publication 4).

Ramaekers, P., 1981. hudsonian and Helikian basins of the Athabasca Region, northern Saskatchewan, *in Proterozoic Basins of Canada, (ed.) F.H.A. Campbell*, GSC, paper 81 – 10, 219 – 233.

Ramaekers, P., G. M. Yeo, O. Catuneanu, C. W. Jefferson and R. H. Rainbird, 2007. Proterozoic to Mesozoic basin development, uranium deposits and heavy oil accumulations, Athabasca region, western Canada; in Jefferson, C.W., and Delaney, G., eds., EXTECH IV: Geology and Uranium EXploration TECHnology of the Proterozoic Athabasca Basin, Saskatchewan and Alberta: Geological Survey of Canada, Bulletin **588** (also Saskatchewan Geological Society, Special Publication 17;

Geological Association of Canada, Mineral Deposits Division, Special Publication 4), in prep.

Ritz, M., M. Descloitres, B. Robineau and M. Courteaud, 1997. Audio-magnetotelluric prospecting for groundwater in the Baril Coastal area, Piton de la Fournaise Volcano, Reunion Island, *Geophysics*, **62**, (3), 758 – 762.

Rodi, W. and R. L. Mackie, 2001. Nonlinear conjugate gradients algorithm for 2D magnetotelluric inversion, *Geophysics*, **66**, (1), 174 – 187.

Ruzicka, V., 1996. Unconformity associated uranium, Geology of Canada, **8**, 197 – 210.

Salisbury, M. H., B. Milkereit, G. Ascough, R. Adair, L. Matthews, D. R. Schmitt, J. Mwenifumbo,D. W. Eaton, and J. Wu, 2000. Physical properties and seismic imaging of massive sulfides. *Geophysics,* **65**, 1882 – 1889.

Sheriff, R. E., 2002. Encyclopedic Dictionary of Applied Geophysics, fourth edition. Society of Exploration Geophysicists, Tulsa.

Shieves, R. B. K., K. Wasyliuk and G. Zaluski, 2000. Detection of K-enrichment, illite chimneys using ground gamma ray spectrometry, McArthur River area, northern Saskatchewan, *Summary of Investigations 2000,* **v2**, *Saskatchewan Geological Survey, Saskatchewan Industry Resources, Miscellaneous Report 2000-4.2*, 160 -169.

Simpson, F. and K. Bahr, 2005. Practical magnetotellurics. Cambridge University Press, Cambridge, UK.

Siripunvaraporn, W. and G. Egbert, 2000. An efficient data-subspace inversion method for 2-D magnetotelluric data, *Geophysics*, **65**, 791 – 803.

Siripunvaraporn, W., G. Egbert, Y. Lenbury and M. Uyeshima, 2005a. Three-dimensional magnetotelluric inversion: data-space method. *Physics of the Earth and Planetary Interiors.* **150**, 3 – 14.

Siripunvaraporn, W., G. Egbert and M. Uyeshima, 2005b. Interpretation of two-dimensional magnetotelluric profile data with three-dimensional inversion: synthetic examples. *Geophysical Journal International,* **160**, 804 – 814.

Smith, J. T., J. R. Booker, 1988. Magnetotelluric inversion for minimum structure, *Geophysics*, 53, 1565 – 1576.

Smith, J. T., J. R. Booker, 1991. Rapid relaxation inversion of two- and three-dimensional magnetotelluric data, *Journal of Geophysical Research*, **96**, 3905 – 3922.

Swift C. M., 1967. A magnetotelluric investigation of an electrical conductivity anomaly in the south-western United States, Ph.D. thesis MIT.

Telford, W. M., L. P. Geldart and R. E. Sheriff, 1990. Applied Geophysics. Cambridge University Press, Cambridge, UK.

Thomas, M. D. and S. McHardy, 2007. Magnetic insights into basement geology in the area of McArthur River uranium deposit, Athabasca Basin, Saskatchewan, in Jefferson, C.W. and Delaney, G., eds., EXTECH IV: Geology and Uranium EXploration TECHnology of the Proterozoic Athabasca Basin, Saskatchewan and Alberta: Geological Survey of Canada, Bulletin **588** (also Saskatchewan Geological Society, Special Publication 18; Geological Association of Canada, Mineral Deposits Division, Special Publication 4).

Thomas, M. D. and G. Wood, 2007. Geological significance of gravity anomalies in the area of McArthur River uranium deposit, Athabasca Basin, Saskatchewan. in Jefferson, C.W. and Delaney, G., eds., EXTECH IV: Geology and Uranium EXploration TECHnology of the Proterozoic Athabasca Basin, Saskatchewan and Alberta: Geological Survey of Canada, Bulletin **588** (also Saskatchewan Geological Society, Special Publication 18; Geological Association of Canada, Mineral Deposits Division, Special Publication 4).

Tikhonov A. N., 1950. Determination of electrical characteristics of the deep strata of the earth's crust. Doklady Akad. Nauk., S.S.S.R., **73**, 295 – 297.

Tikhonov A. N. and V. Y. Arsenin, 1977. Solutions of ill-posed problems. V. H. Winston and Sons.

Tuncer, V., M. J. Unsworth, W. Siripunvaraporn and J. A. Craven, 2006a. Exploration for unconformity type uranium deposits with audio-magnetotelluric data: A case study from the McArthur River Mine, Saskatchewan (Canada), *Geophysics*, **71** (6), B201 – B209.

Tuncer, V., M. J. Unsworth, W. Siripunvaraporn and J. A. Craven, 2006b. Audio-magnetotelluric exploration for unconformity uranium deposits in the Athabasca Basin, Saskatchewan, Canada, presented at 76th SEG Annual Meeting and Workshop on Geophysical Methods and Techniques Applied to Uranium Exploration, New Orleans, Louisiana, USA

Uchida, T., 1993. Smooth 2-D Inversion for Magnetotelluric Data Based on Statistical Criterion ABIC, *Journal of Geomagnetism and Geoelectricity*, **45**, 841 – 858.

Uchida, T., 1993. Inversion of COPROD2 Magnetotelluric Data by Use of ABIC Minimization Method, *Journal of Geomagnetism and Geoelectricity*, **45**, 1063 – 1071.

Vozoff, K., 1991. The magnetotelluric method, in Misac N. Nabighian ed., Electromagnetic methods in applied geophysics, vol.2: SEG, 641 – 711.

Wannamaker, P. E., G. W. Hohmann and S. H. Ward, 1984. Magnetotelluric responses of three-dimensional bodies in layered earths using integral equations, *Geophysics*, **49**, 1517 – 1533.

Wasyliuk, K., 2002. Petrogenesis of the kaolinite-group minerals in the eastern Athabasca basin of northern Saskatchewan: Applications to uranium mineralization; M. Sc. Thesis, University of Saskatchewan, Saskatoon, Saskatchewan, 140 p.

White, D. J., B. Roberts, C. Mueller, Z. Hajnal, I. Györfi, B. Reilkoff, R. Koch and B. Powell, 2002. Seismic reflection profiling: An effective exploration tool in the Athabasca basin? An interim assessment, *Summary of Investigations 2002,* **v2**, *Saskatchewan Geological Survey, Saskatchewan Industry Resources, Miscellaneous Report 2002-4.2* Paper D-2.

White, D. J., Z. Hajnal, I. Gyorfi, E. Takacs, B. Roberts, C. Mueller, B. Reilkoff, R. Koch, B. Powell, I. Annesley, S. Bernier and C. Jefferson, 2003. Interim results of the EXTECH-IV seismic-reflection program in the Athabasca Basin, northern Saskatchewan, *Geological Survey of Canada Current Research*, C8.

White, D. J., Z. Hajnal, B. Roberts, I. Gyorfi, B. Reilkoff, B. Bellefleur, C. Mueller, S. Woelz, C. J. Mwenifumbo, E. Takacs, D. R. Schmitt, D. Brisbin, C. W. Jefferson, R. Koch, B. Powell and I. Annesley, 2007. Seismic methods for uranium exploration; an overview of EXTECH IV seismic studies at the McArthur River mining camp, Athabasca Basin, Saskatchewan; in Jefferson, C.W., and Delaney, G., eds., EXTECH IV: Geology and Uranium EXploration TECHnology of the Proterozoic Athabasca Basin, Saskatchewan and Alberta: Geological Survey of Canada, Bulletin **588** (also Saskatchewan Geological Society, Special Publication 18; Geological Association of Canada, Mineral Deposits Division, Special Publication 4).

Wiese, H., 1962. Geomagnetische tiefentellurik, *Geophys. Pura. Appl.*, **52**, 83 – 103.

Wood, G. and M. D. Thomas, 2002. Modeling of high-resolution gravity data near the McArthur River uranium deposit, Athabasca Basin, *Summary of Investigations 2002,* **v2**, *Saskatchewan Geological Survey, Saskatchewan Industry Resources, Miscellaneous Report 2002-4.2*, Paper D-16.

World Uranium Mining, 2004. Nuclear Issues Briefing Paper 41; June 2004; published by Uranium Information Centre, Melbourne, Australia at www.uic.com.au.

Xiao, W., and M. J. Unsworth, 2006. Structural imaging in the Rocky Mountain Foothills (Alberta) using magnetotelluric exploration, *AAPG Bulletin*, **90**, 321-333.

Yeo, G., C. W. Jefferson, P. Ramaekers and K. Tong, 2001b. From Palm to Plot - Core logging methodology in Athabasca Basin; in Summary of Investigations 2001, Volume **2**, Saskatchewan Geological Survey, Sask. Energy Mines, Misc. Rep. 2001-4.2, 314 – 319.

Yeo, G., J. B. Percival, C. W. Jefferson, R. Ickert and P. Hunt, 2007a. Environmental significance of oncoids and crypto-microbial laminates from

the Late Paleoproterozoic Athabasca Group, Saskatchewan and Alberta; ; in Jefferson, C.W. and Delaney, G. , eds., EXTECH IV: Geology and Uranium EXploration TECHnology of the Proterozoic Athabasca Basin, Saskatchewan and Alberta: Geological Survey of Canada, Bulletin **588** (also Saskatchewan Geological Society, Special Publication 17; Geological Association of Canada, Mineral Deposits Division, Special Publication 4).

Yeo, G. M., P. Ramaekers, C. W. Jefferson, S. Bernier, O. Catuneanu, B. Collier, B. Kupsch, D. G .F. Long and R. Post, 2007b. Comparison of lower Athabasca Group stratigraphy among deposystems, Saskatchewan and Alberta; in Jefferson, C.W. and Delaney, G., eds., EXTECH IV: Geology and Uranium EXploration TECHnology of the Proterozoic Athabasca Basin, Saskatchewan and Alberta: Geological Survey of Canada, Bulletin **588** (also Saskatchewan Geological Society, Special Publication 17; Geological Association of Canada, Mineral Deposits Division, Special Publication 4).

Appendix A

Pseudosections of the McArthur River profiles and the fit of the 2D inversions

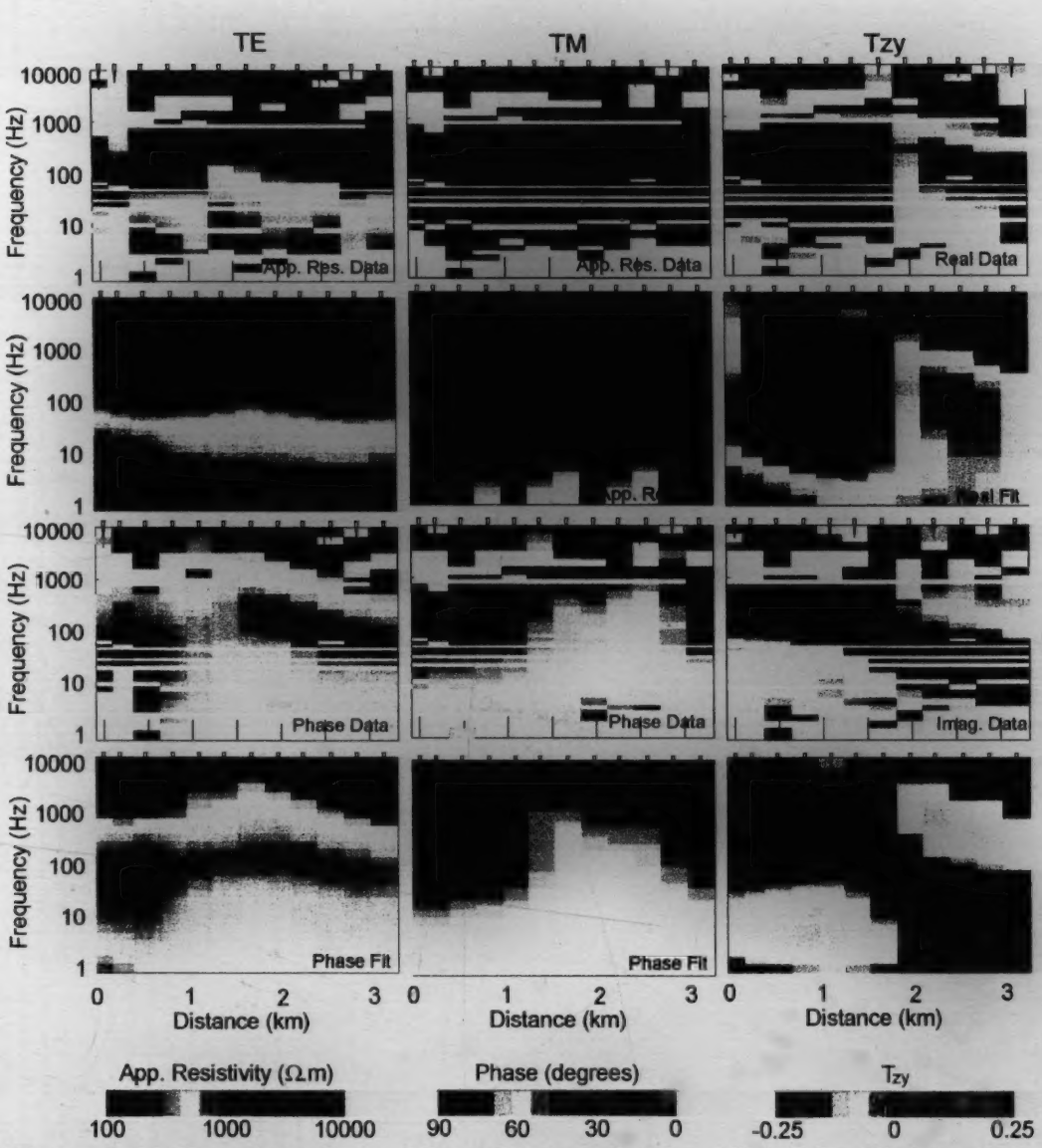

Figure A-1. Pseudosections of the measured data and fits of the 2D inversions for profile 224. Note that $\alpha = 1$ and $\tau = 10$ in the inversion.

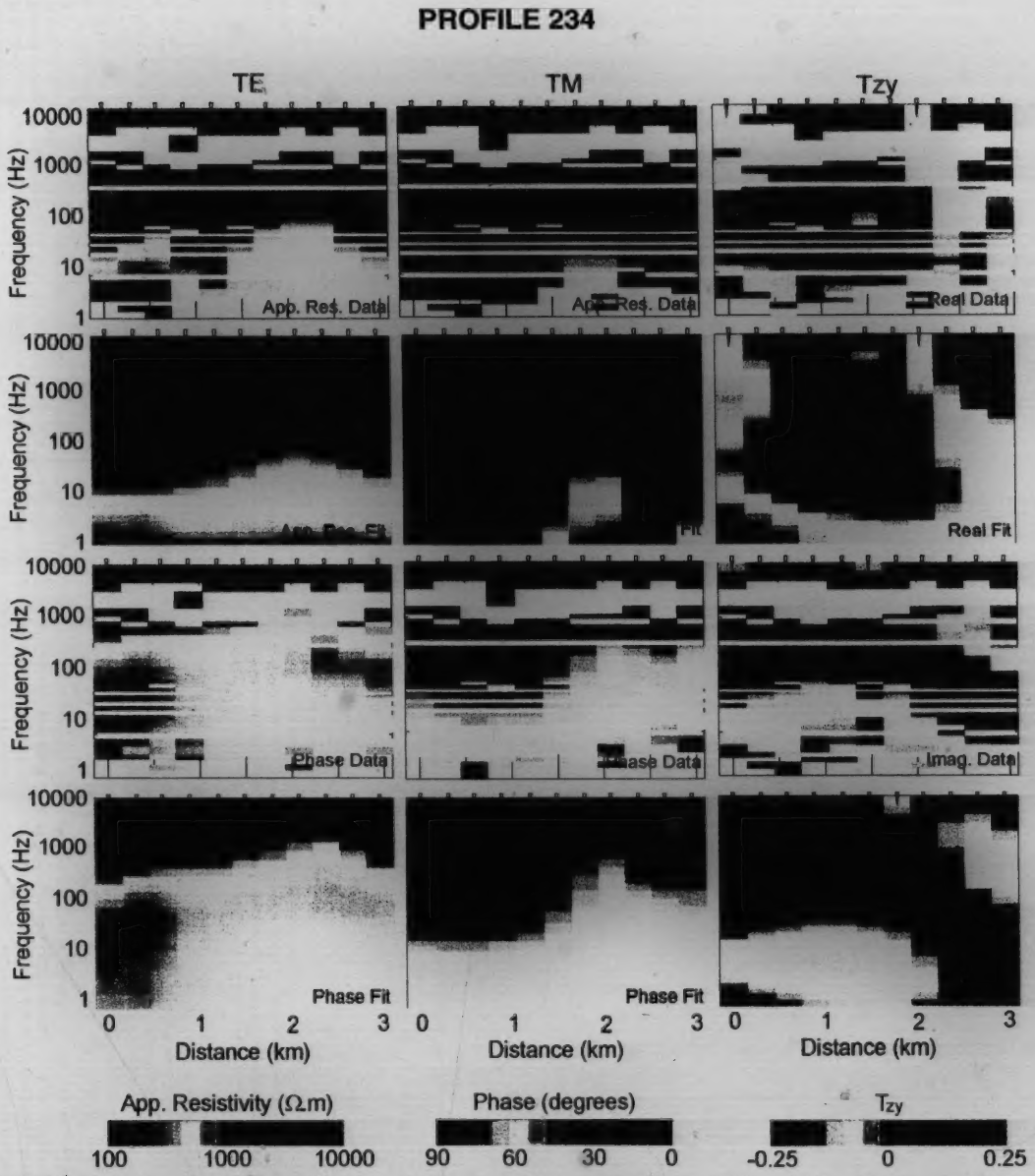

Figure A-2. Pseudosections of the measured data and fits of the 2D inversions for profile 234. Note that $\alpha = 1$ and $\tau = 10$ in the inversion.

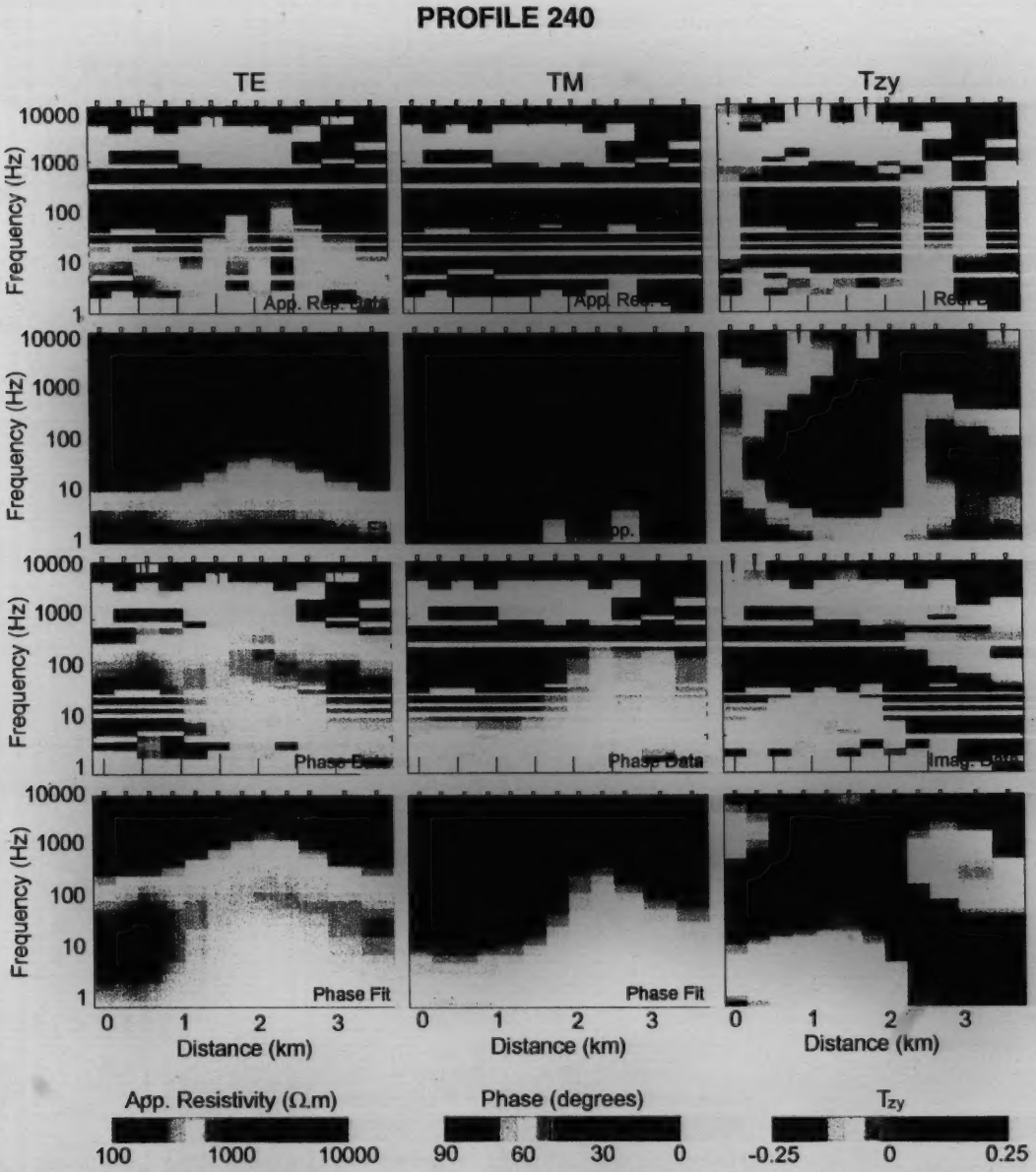

Figure A-3. Pseudosections of the measured data and fits of the 2D inversions for profile 240. Note that $\alpha = 1$ and $\tau = 10$ in the inversion.

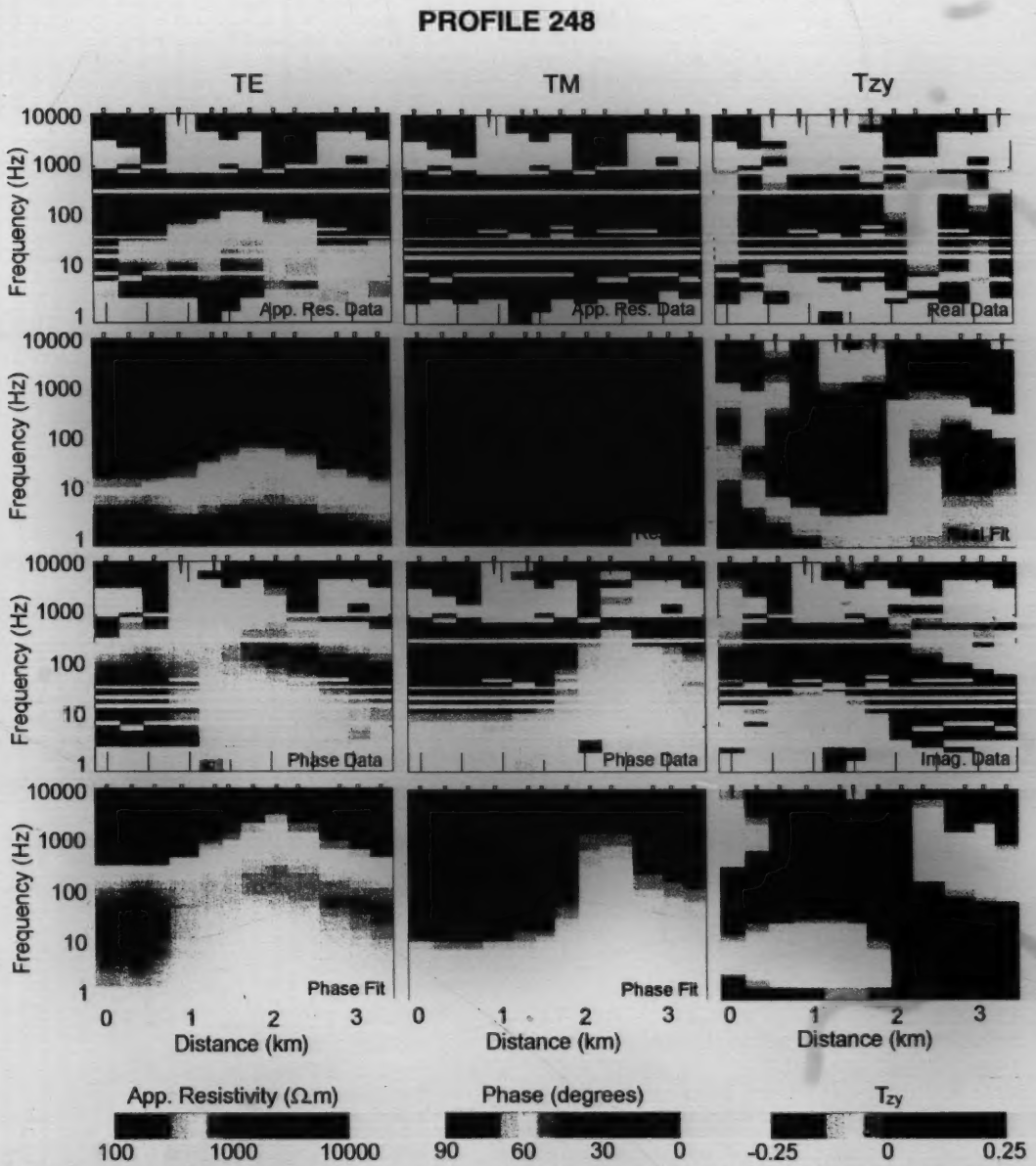

Figure A-4. Pseudosections of the measured data and fits of the 2D inversions for profile 248. Note that $\alpha = 1$ and $\tau = 10$ in the inversion.

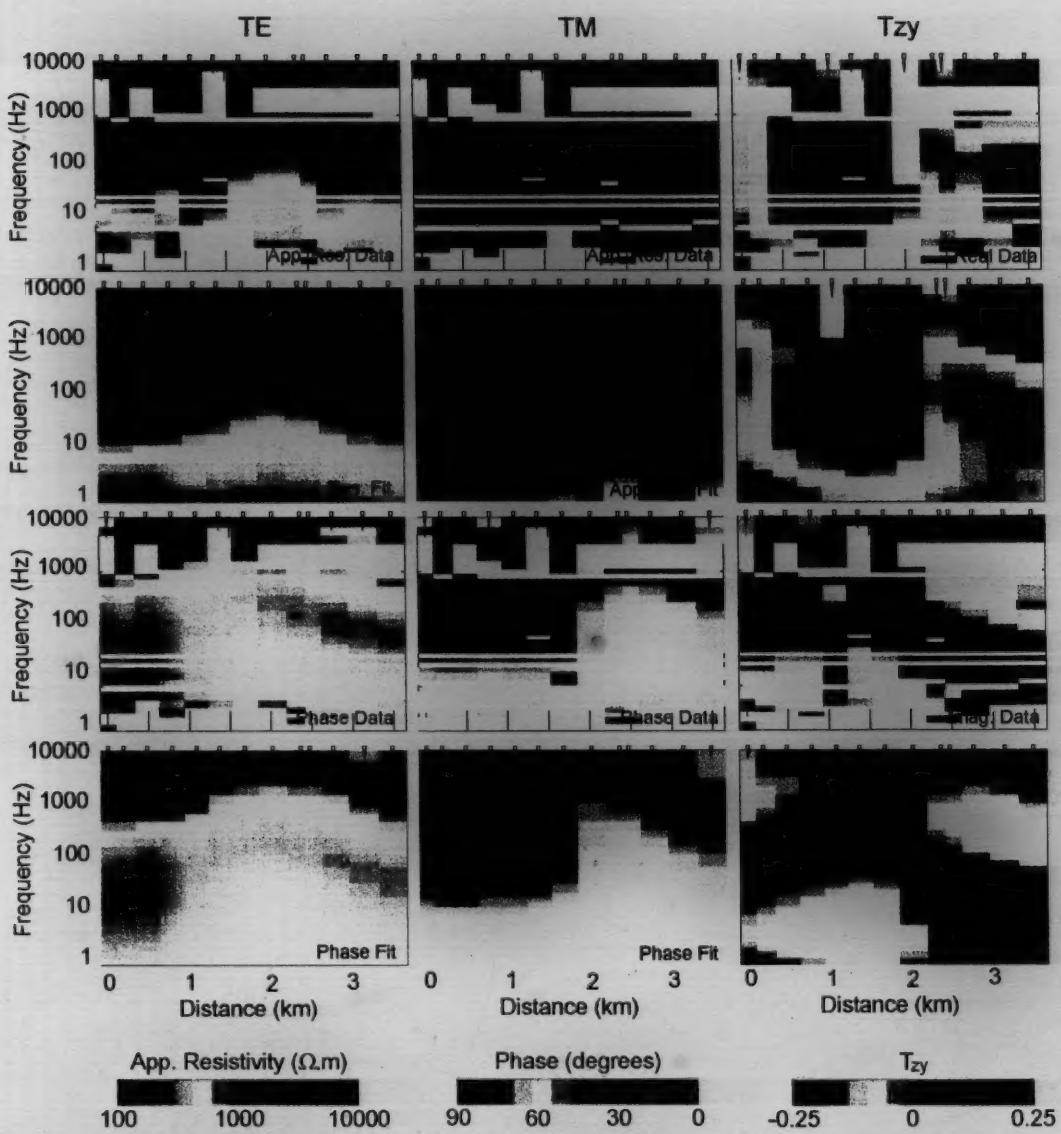

Figure A-5. Pseudosections of the measured data and fits of the 2D inversions for profile 254. Note that $\alpha = 1$ and $\tau = 10$ in the inversion.

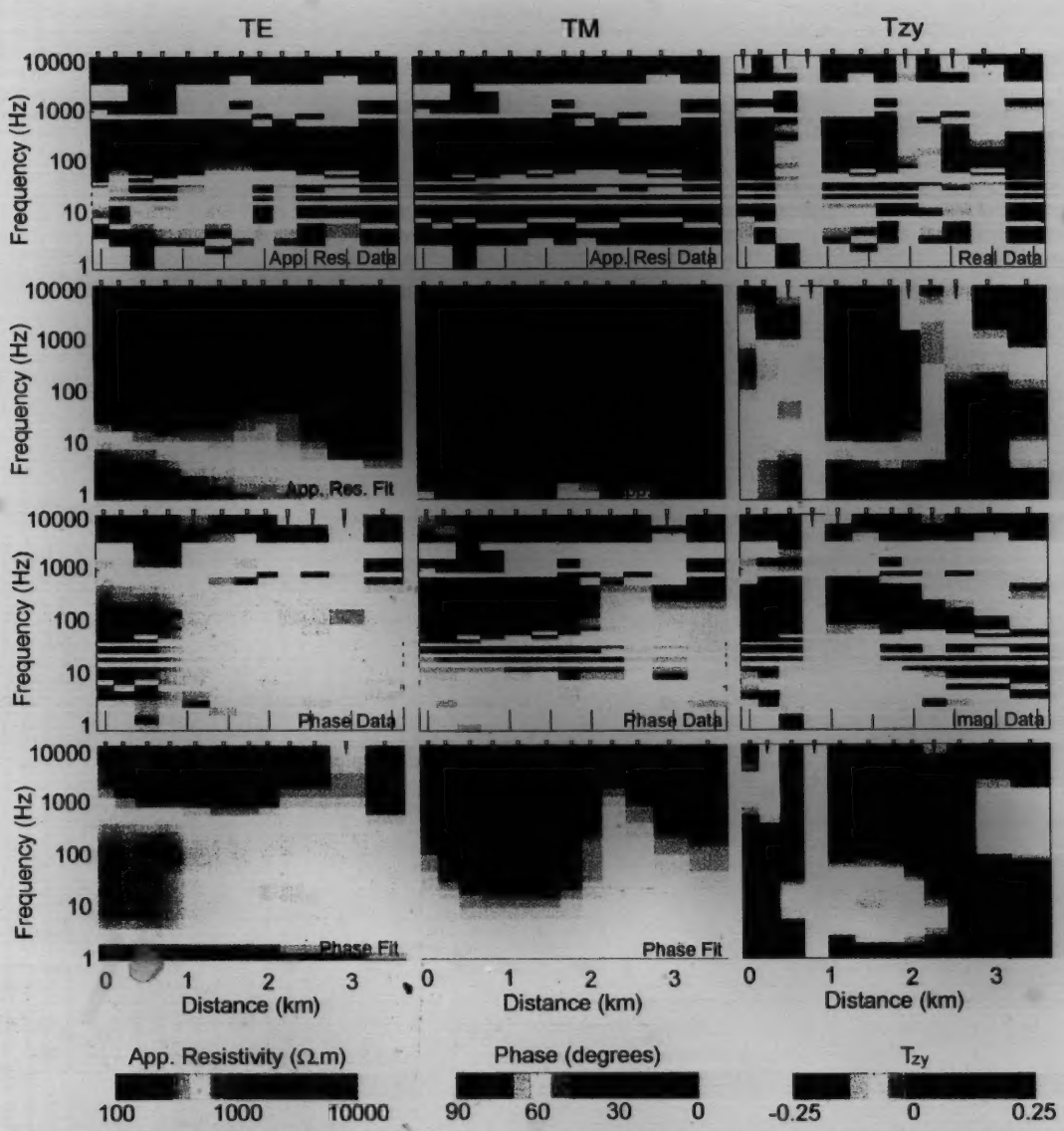

Figure A-6. Pseudosections of the measured data and fits of the 2D inversions for profile 266. Note that $\alpha = 1$ and $\tau = 10$ in the inversion.

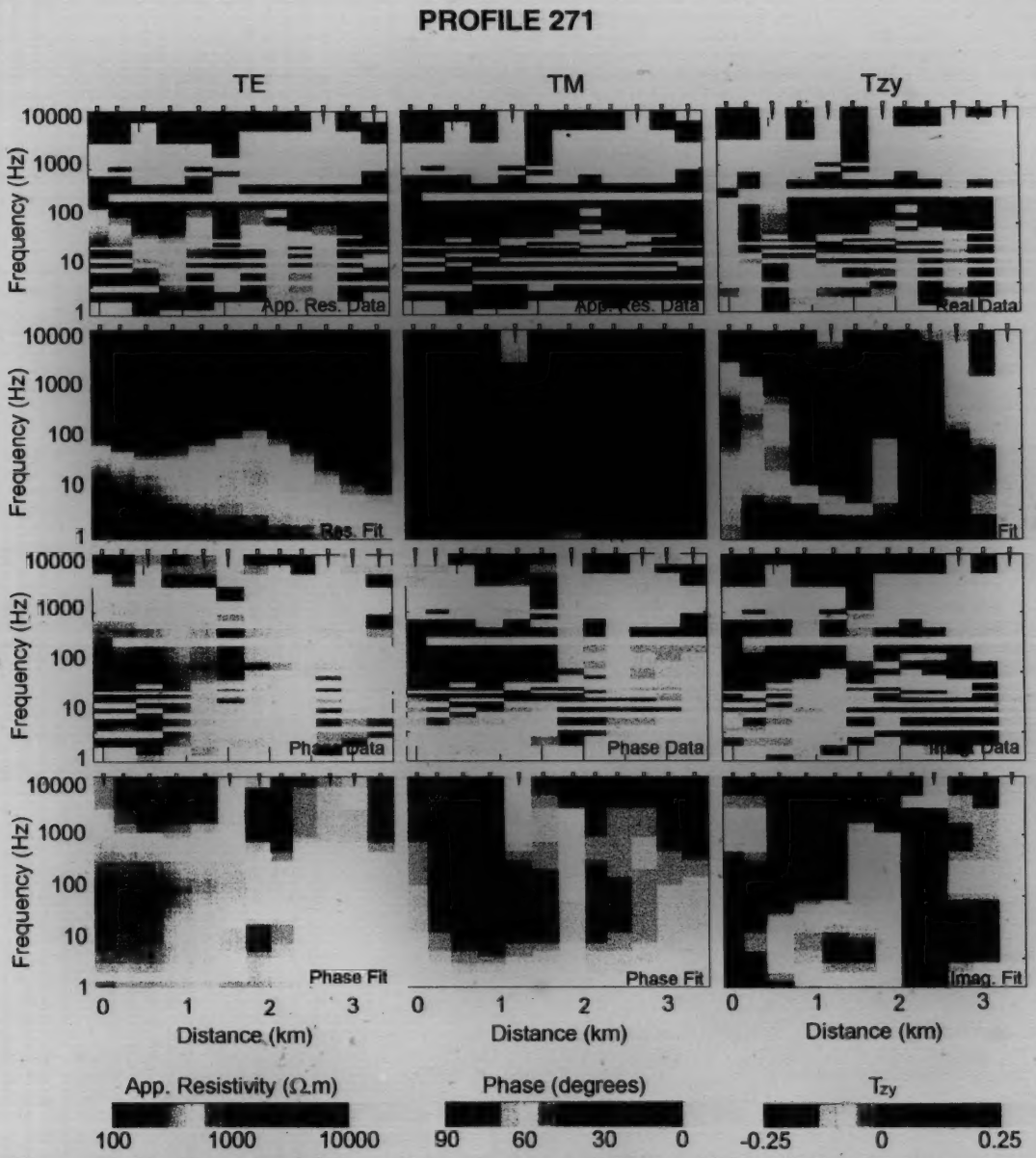

Figure A-7. Pseudosections of the measured data and fits of the 2D inversions for profile 271. Note that $\alpha = 1$ and $\tau = 10$ in the inversion.

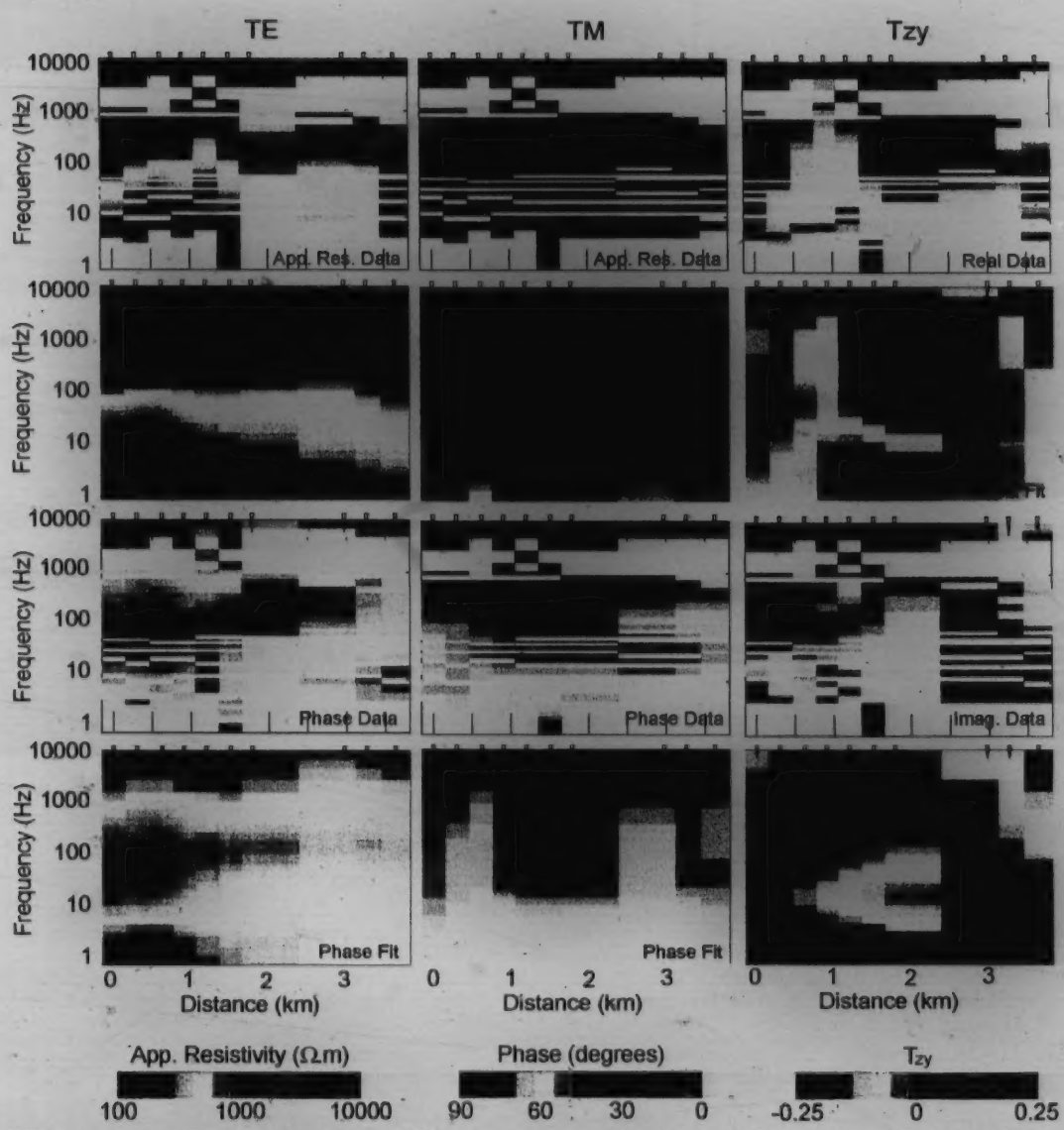

Figure A-8. Pseudosections of the measured data and fits of the 2D inversions for profile 276. Note that $\alpha = 1$ and $\tau = 10$ in the inversion.

PROFILE 288

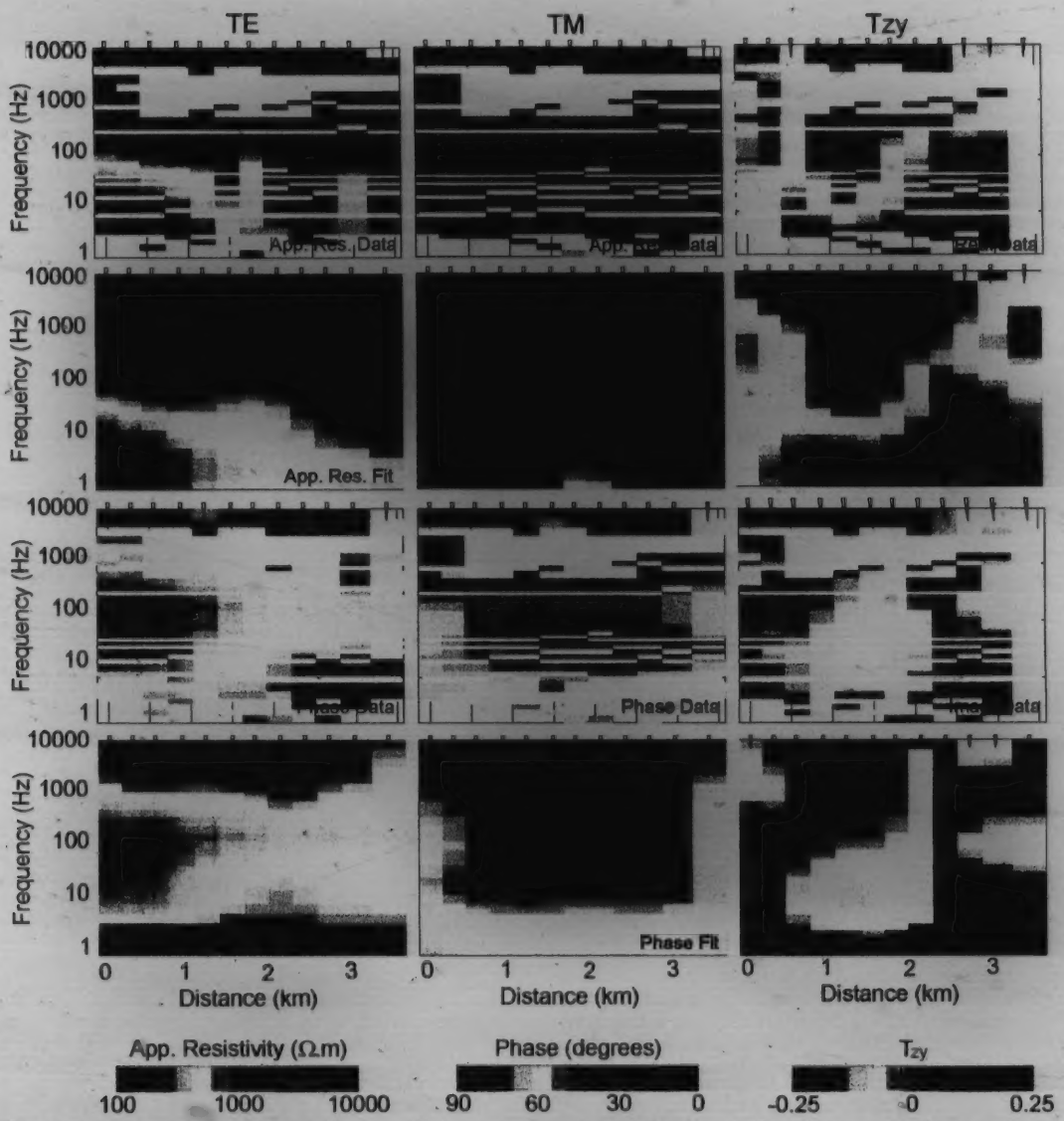

Figure A-9. Pseudosections of the measured data and fits of the 2D inversions for profile 288. Note that $\alpha = 1$ and $\tau = 10$ in the inversion.

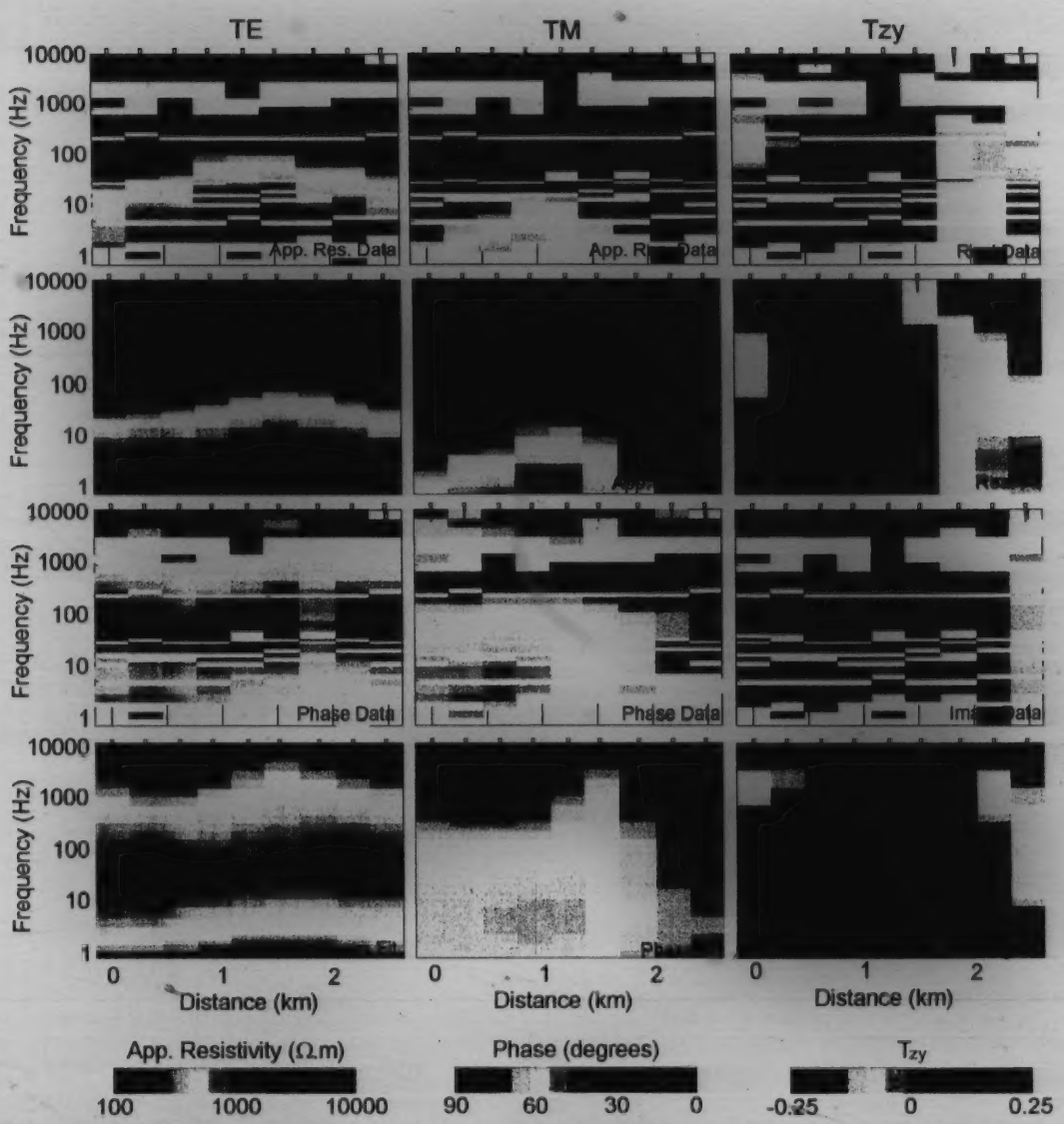

Figure A-10. Pseudosections of the measured data and fits of the 2D inversions for profile 296. Note that $\alpha = 1$ and $\tau = 10$ in the inversion.

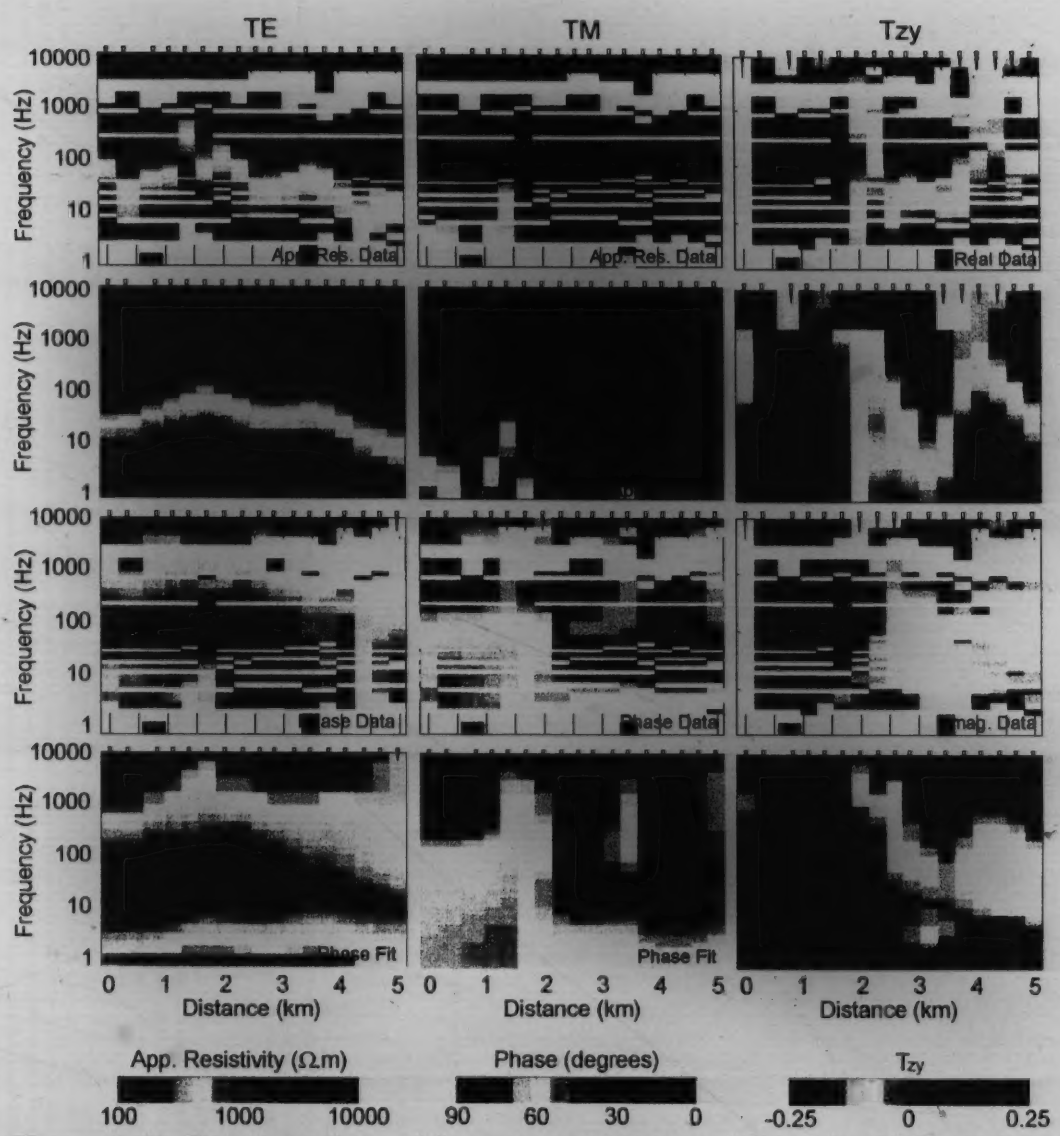

Figure A-11. Pseudosections of the measured data and fits of the 2D inversions for profile 304. Note that $\alpha = 1$ and $\tau = 10$ in the inversion.

Appendix B

Two-Dimensional Inversions of the McArthur River AMT dataset

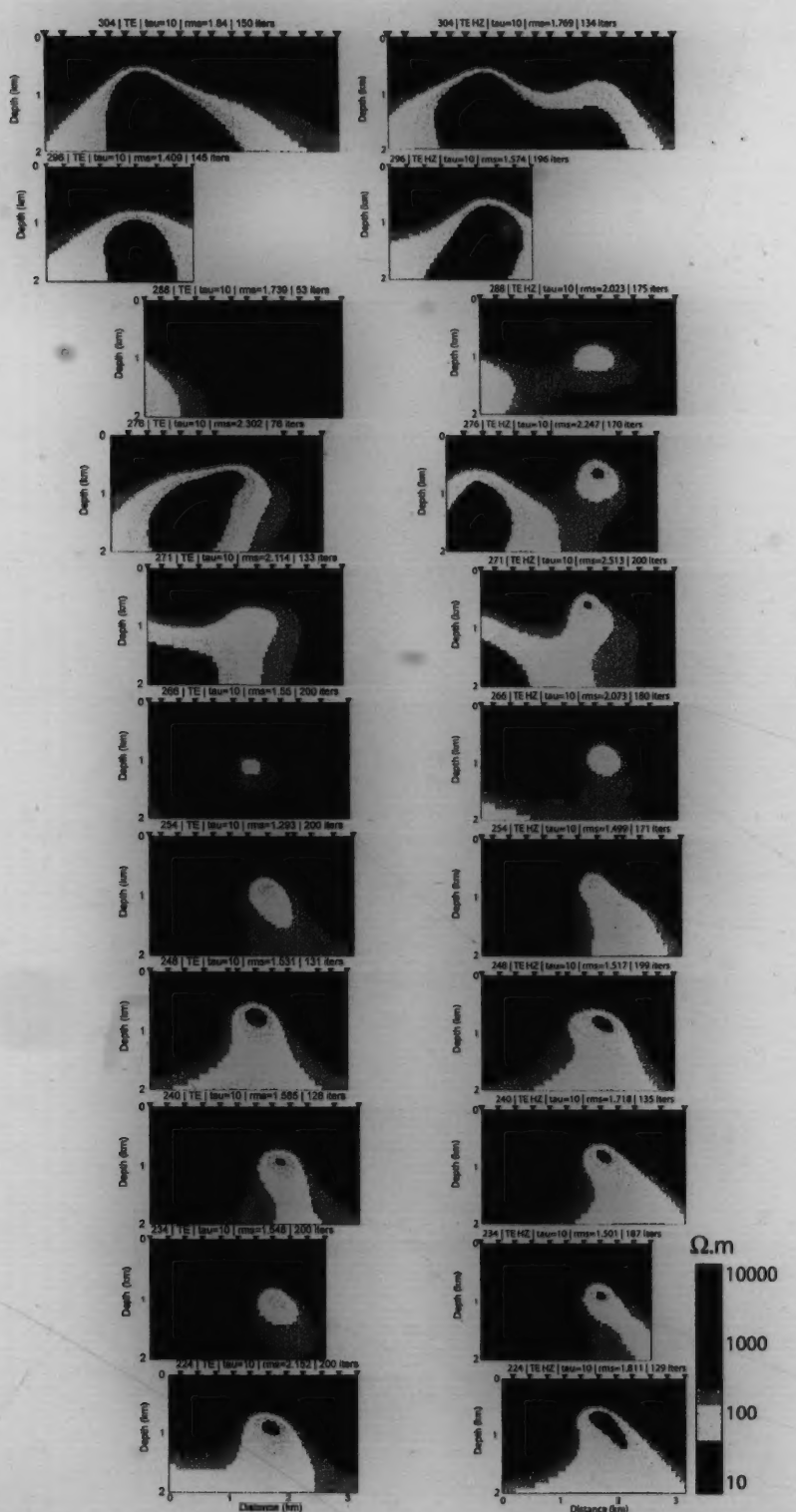

Figure B-1. Resistivity models of TE mode and TE-T_{zy} for all profiles.

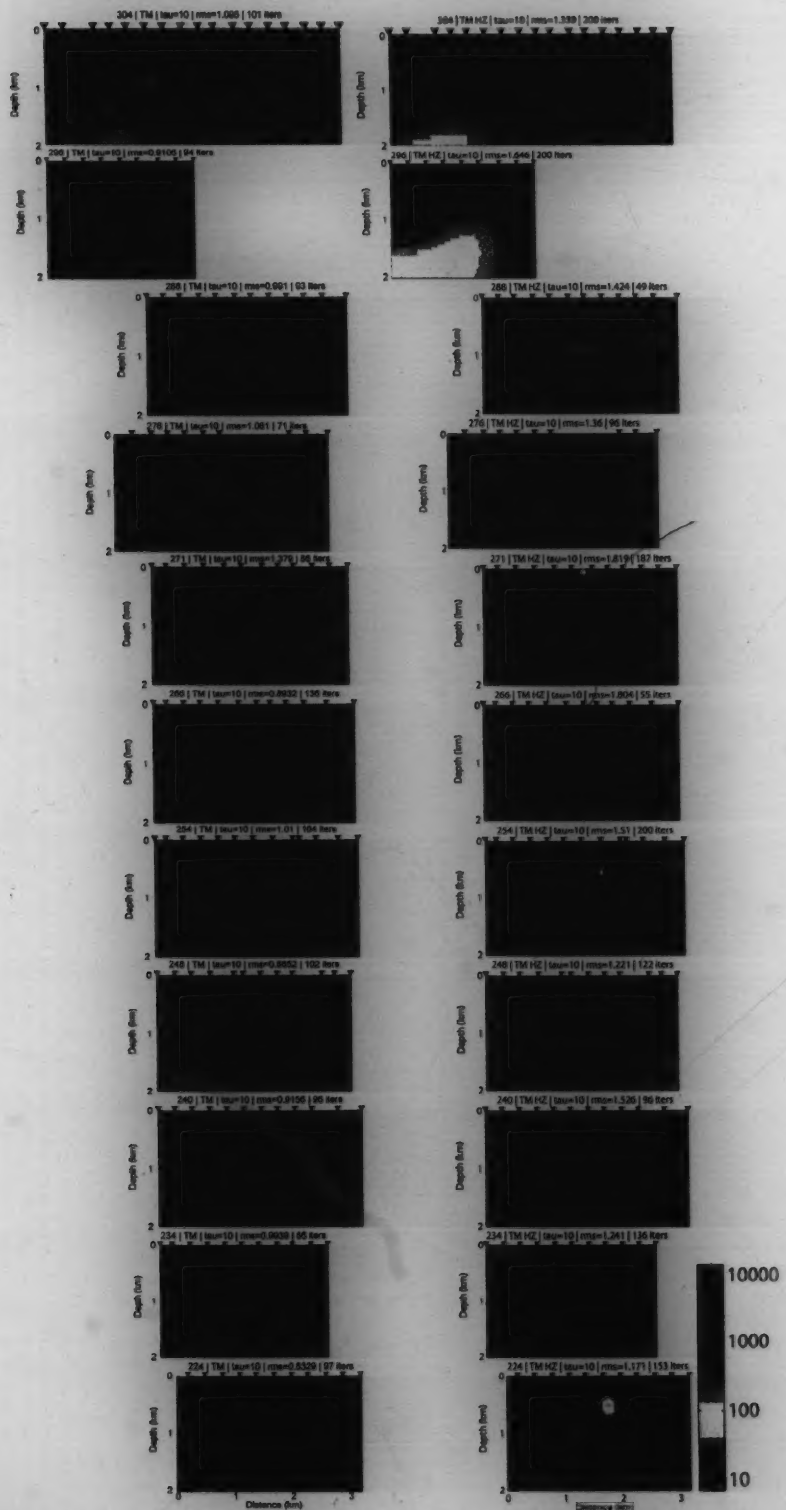

Figure B-2. Resistivity models of TM mode and TM-T_{zy} for all profiles.

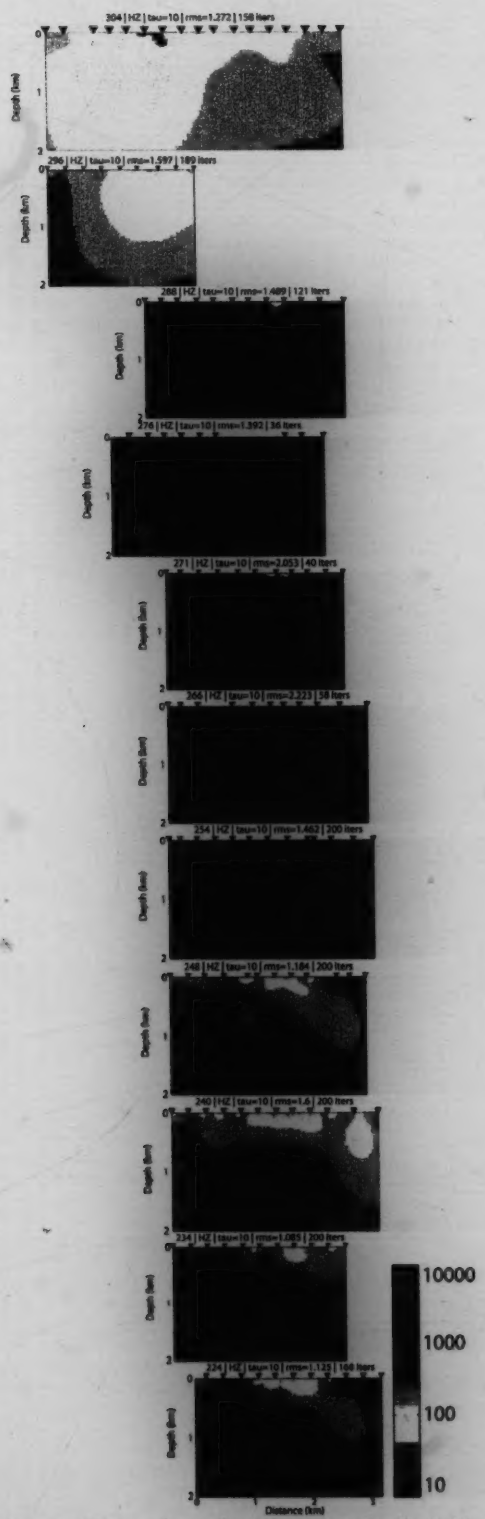

Figure B-3. Resistivity models of vertical magnetic field for all profiles.